ACS APPLIED ENERGY MATERIALS

www.acsaem.org Review

Perovskite Nanowires for Next-Generation Optoelectronic Devices: Lab to Fab

Gundam Sandeep Kumar,[#] Ranadeep Raj Sumukam,[#] Rakesh Kumar Rajaboina, Ramu Naidu Savu, Mudavat Srinivas, and Murali Banavoth*

Cite This: *ACS Appl. Energy Mater.* 2022, 5, 1342−1377 Read Online

ACCESS | Metrics & More | Article Recommendations

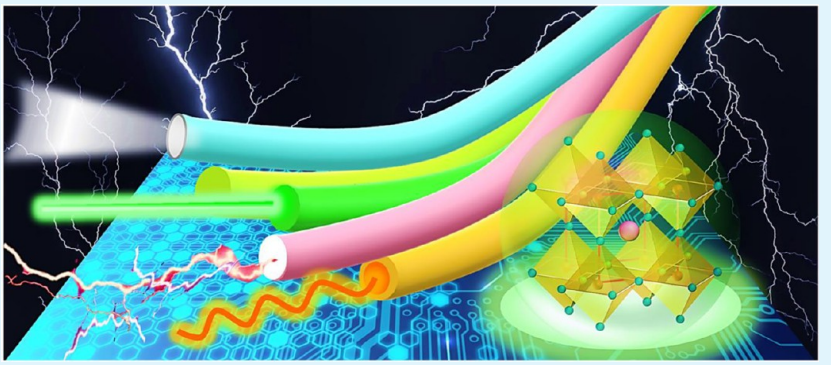

ABSTRACT: The minuscule sizes of one-dimensional (1D) nanostructures have revolutionized photonic circuitry and led to efficient optoelectronic devices with unprecedented speed. With the impressive progress accomplished in consideration of pressing challenges, perovskite materials have been in the spotlight in research. The low-dimensional perovskites (especially nanowires) supersede their bulk counterparts with remarkable optoelectronic properties that make them suitable to be used in a broad range of applications. Nevertheless, for realizing any potential application, mechanistic insights on the crystal growth, especially the ordering/orientation and hence the underlying physics of light−matter interactions in the perovskite nanowires, are needed, and research is yet to plateau. Herein, we emphasize the fundamental understanding of formation mechanisms and anticipated challenges along with the progressive evolutions of several blossoming candidates in exciting optoelectronic applications such as photodetectors, lasers, light-emitting diodes, photovoltaic cells, and field-effect transistors. Importantly, the perspectives offered in this Review can stimulate future research directions and opportunities that could pave the way for ambient-stable next-generation optoelectronic devices.

KEYWORDS: *perovskites, nanowires, optoelectronic devices, photodetectors, lasers, light-emitting diodes, solar cells, field-effect transistors*

Metal halide perovskites have emerged as a class of frontline semiconductors and have attracted tremendous research attention in recent years. Control over the band structure by judicious manipulation of the composition and dimensionality makes them promising materials with striking photophysical properties, such as a large optical absorption coefficient, low defect density, long diffusion length, and suppressed Auger recombination rate.[1−4] The research enthusiasm around this led to the exploration of these alluring semiconductors in various optoelectronic applications, such as photovoltaics (PVs),[5−12] lasers,[13−15] light-emitting diodes (LEDs),[16−19] and photodetectors (PDs).[20−22] Remarkable success has been progressively accomplished, especially in PVs and LEDs, where the corresponding maximum certified photoconversion efficiency (PCE) has reached 25.2%[23] and the external quantum efficiency (EQE) has reached 23.4%,[24] respectively.

Most of the high-performing devices reported so far have been fabricated from polycrystalline perovskite thin films owing to their simple solution-processability by either one-step or two-step processes. Notably, the performances are strongly influenced by the thin films' morphology, crystallinity, uniformity, grain size, surface coverage, and thickness.[25−29] Importantly, polycrystalline thin-film-based devices, though believed to be next-generation candidates, are limited due to critical drawbacks that circumscribe their potential commercial applications.[30−33] For instance, low-temperature solution

Received: October 19, 2021
Accepted: December 27, 2021
Published: January 18, 2022

processes induce mobile ionic defects within the polycrystalline thin film that lead to hysteretic current−voltage (I−V) characteristics under an external bias and act as recombination centers for photogenerated carriers, thereby lowering the overall charge collection efficiency.[30,31] Moreover, polycrystalline thin films comprise comparatively larger numbers of grain boundaries, which act as charge recombination sites for photogenerated carriers and also favorable paths for external moisture.[32] Temperature-related issues such as phase transition and compositional degradation owing to their low thermal/ambient stability deteriorates perovskites' long-term stability.[33] Hence, to accomplish high-performing, stable, and reliable optoelectronic devices from the perovskites, there is a prerequisite for designing perovskites materials with ionic defect-free, grain-boundary-free, and highly crystalline or single-crystalline structures. In an assessment of polycrystalline thin films, single-crystalline 1D nanowires (NWs) are found to have negligible ionic defects and grain boundaries and consequently display enhanced photogenerated carrier transport properties, and devices based on NWs show superior performance, reliability, and stability.[34−36]

Moreover, the confined charge carrier transport in the 1D channel, along with a high specific surface area, makes 1D NWs the most alluring nanostructures. Conventionally, NWs have been synthesized from a variety of semiconductors; however, perovskites have shown phenomenal performance due to unprecedented attributes owing to their high optical absorption coefficient, low density of defect states, carrier lifetime, and diffusion lengths, which qualify them as potential building blocks for technologically important applications.[35] Considerable attention has been focused on the splendid 1D metal−halide perovskites since the first report by Endre Horváth.[37] The enhanced photoelectric performance of 1D nanostructures such as NWs and nanorods (NRs), compared to their polycrystalline counterparts, is due to the charge carriers and photons being transported in one dimension while they are confined to the other two dimensions.[38] Although 1D perovskite NWs are anticipated to be forerunners, they call for more efforts for controlling light absorption, charge separation, charge transport, and recombination to unleash their potential for exhilarating applications.

The enclosing surfaces and defined crystal structure of 1D perovskite NWs ensure various optoelectronics applications, such as PDs, lasers, LEDs, PVs, field-effect transistors (FETs), and waveguides (Figure 1a). For instance, an ultrahigh responsivity of 13 700 A W^{-1} and ultrafast response time of ∼0.3 μs were demonstrated using PDs based on a $MAPbBr_3$ NWs array (MA = methylammonium).[39] Similarly, an ultralow lasing threshold of 220 nJ cm^{-2} and ultrahigh quality factor of 3600 were obtained for $MAPbI_3$ NW-based lasers.[40] A maximum brightness of 12 016 cd m^{-2} and an EQE of 16% were demonstrated using $CsPbBr_3$ NWs-based LEDs.[41] Importantly, a maximum PCE of 18.83% with enhanced stability was shown using perovskite NWs-based PVs.[42] $CsPbBr_3$−MoO_3 core−shell NWs-based FETs exhibited an enhanced performance with highest hole mobility of 23.3 cm^2 $(V{\cdot}s)^{-1}$ and improved device stability owing to the MoO_3 surface passivation.[43] Despite the stability issues that bottleneck their timely commercialization, the facile low-cost synthesis protocols of perovskite NWs give them crucial potential for future integrated photonic devices.

Recent reports on halide perovskite NWs are confined to particular perovskite systems and lack information on their

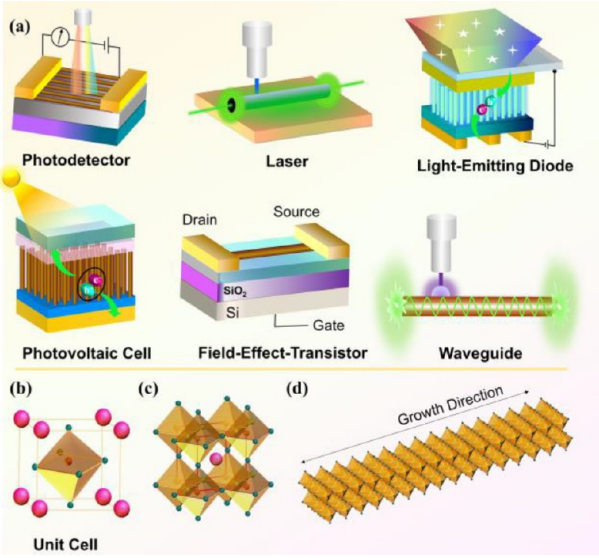

Figure 1. (a) Schematic illustration of the various potential optoelectronic applications of perovskite 1D NWs. Pictorial crystal structure of ABX_3 metal halide perovskites: (b) Structure of unit cell, where A cations are represented by pink spheres, B cations are represented by orange spheres, and X anions are represented by bluish-green spheres. (c) An extended network of ABX_3 perovskites connected by corner-shared octahedrons. (d) Elongated 1D crystal structure of perovskite NWs.

growth mechanisms, which essentially drive the desired aspect ratios needed for fabricating high-quality sensors.[44−48] There is a missing link between all the synthesis methods and state-of-the-art growth mechanisms of perovskite (organic, inorganic, hybrid) NWs and their optoelectronic applications such as PDs, lasers, LEDs, and PVs. Here, in this Review, we provide a glimpse into the evolution of hybrid organic−inorganic and all-inorganic halide perovskite NWs along with their synthesis methodologies and growth mechanisms. We make our best attempts in considering the literature to date and presenting the milestones in the development of perovskite NWs for a broad range of potential optoelectronic applications. Finally, we analyze the critical challenges and suggest future perspectives that can benefit the research community for the development of high-quality perovskite NWs and their integration in various next-generation device applications.

1. SYNTHESIS AND GROWTH MECHANISMS OF PEROVSKITE NANOWIRES

The general formula of a typical halide perovskite is ABX_3, where the A site is a monovalent organic or inorganic cation or their mixture (Cs^+, $MA^+ = CH_3NH_3^+$ or $FA^+ = NH_2CHNH_2^+$), the B site is a bivalent cation (Pb^{2+} or Sn^{2+}), and the X site is a halide (I^-, Br^- or Cl^-). Figure 1b depicts a typical unit cell structure of a perovskite single crystal, where A, B, and X are located at corner, body, and face centers, respectively. Each of the B atoms is connected with six adjacent X atoms via ionic bonding, and A group has 12 nearest X atoms. An extended network of ABX_3 halide perovskites linked by corner-sharing octahedra is shown in Figure 1c.

Most of the commonly used solution-phase methods, such as one-step self-assembly and two-step sequential deposition of precursors employed for the synthesis of metal−halide perovskites, are likely to yield polycrystalline thin films. Hence, various strategies were implemented to generate

https://doi.org/10.1021/acsaem.1c03284
ACS Appl. Energy Mater. 2022, 5, 1342−1377

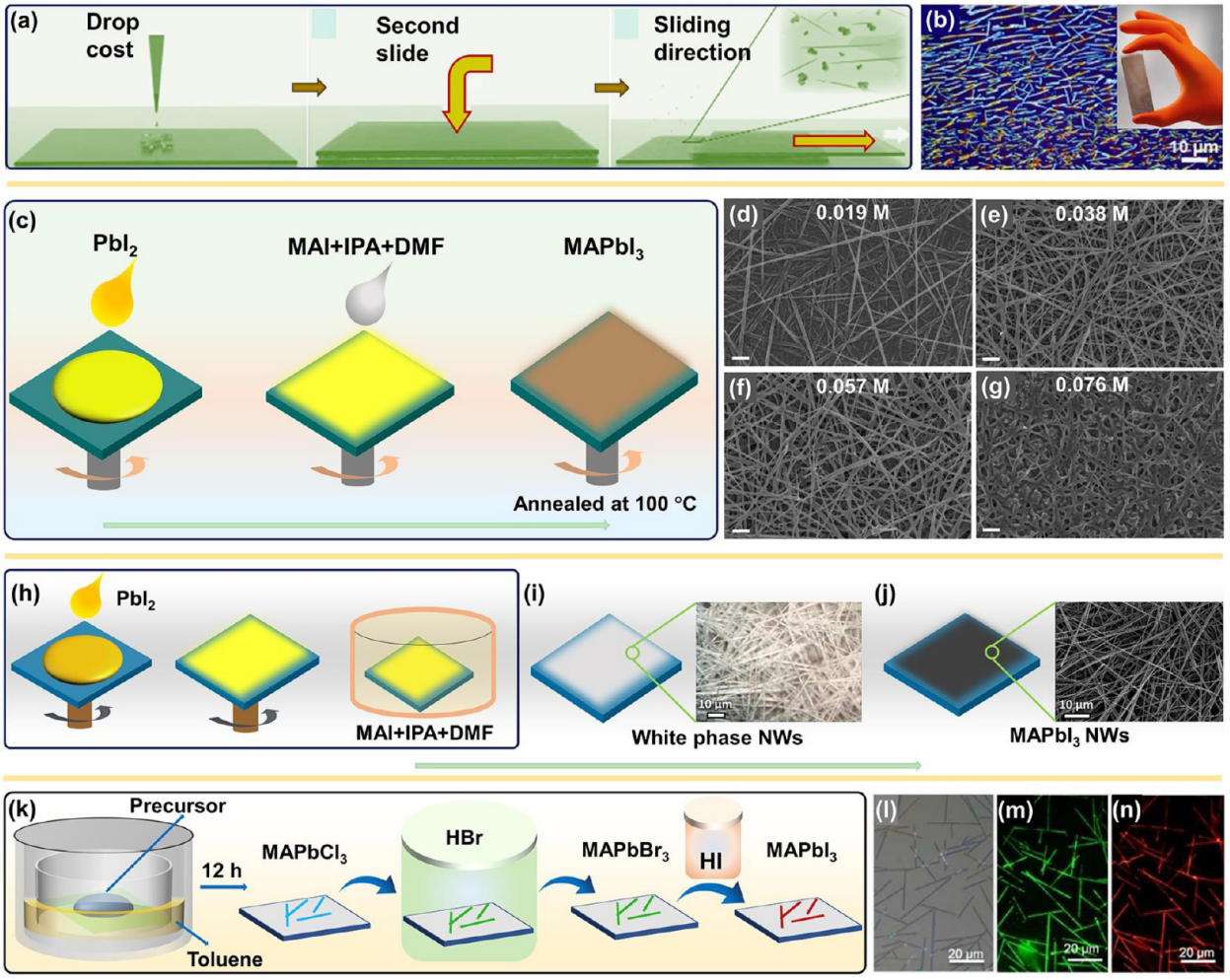

Figure 2. (a) Schematic representation of the step-by-step process of low-temperature slip-coating technique for the growth of $MAPbI_3$ NWs on a glass substrate. (b) Optical microscopy image of NWs grown on SiO_2/Si substrate. The inset shows a digital photographic image of a microscope glass slide containing the NWs. Adapted with permission from ref 37. Copyright 2014 American Chemical Society. (c) Pictorial representation of a two-step spin-coating process for the growth of perovskite NWs. Reprinted with permission from ref 49. Copyright 2015 American Chemical Society. (d–g) SEM images of $MAPbI_3$ NWs grown with 50 μL of DMF/5 mL of IPA solution with different concentrations of MAI: (d) 0.019 M (15 mg MAI), (e) 0.038 M (30 mg), (f) 0.057 M (45 mg), and (g) 0.076 M (60 mg). Adapted with permission from ref 49. Copyright 2015 American Chemical Society. (h) Schematic illustration of the solution-dipping process for the growth of perovskite NWs. (i) Optical microscopic image of the intermediate white-phase NWs. (j) SEM image of fully converted perovskite-phase NWs. Reprinted with permission from ref 55. Copyright 2017 American Chemical Society. (k) Pictorial representation of one-step solution-phase growth of $MAPbCl_3$ NWs and their sequential halide conversion for obtaining $MAPbBr_3$ and $MAPbI_3$ NWs through HBr and HI vapor, respectively. Reprinted with permission from ref 56. Copyright 2017 Royal Society of Chemistry. (l–n) Fluorescence microscopic images of $MAPbCl_3$, $MAPbBr_3$, and $MAPbI_3$ NWs at the same location, respectively. Adapted with permission from ref 56. Copyright 2017 Royal Society of Chemistry.

desired 1D perovskite NWs. First, a dissolution–reprecipitation method, where $MAPbI_3$ NWs were obtained by spin-coating the methylammonium iodide (MAI)/isopropanol (IPA)/dimethylformamide (DMF) solution onto the predeposited PbI_2 layer, was demonstrated by Park et al. for the fabrication of $MAPbI_3$ NWs.[49] Perovskites grew along the low-energy crystal plane ⟨001⟩ to form an anisotropic 1D geometry (Figure 1d). In the following sections, we review solution-phase and vapor-phase synthesis methods for the growth of halide perovskite NWs.

Perovskite NWs are synthesized mainly by employing (i) solution-phase and (ii) vapor-phase methods. Solution-phase synthesis, being a low-temperature method, provides high yield, aspect ratio regulation, and ease of transfer onto target substrates for device fabrication. In contrast, vapor-phase synthesis allows us to control the size and position of NWs that achieve in-plane orientation of high-quality crystals with lower defect density for direct device integration.

1.1. Solution-Phase Synthesis of Perovskite NWs.

Solution-phase methods have been extensively employed for the preparation of perovskites of different morphological nanostructures, such as 1D NWs, 2D nanosheets, 0D quantum dots, and 3D bulk-phase thin films. The solution-phase synthesis methods widely used by many researchers to grow perovskite NWs can be further classified into various categories based on the mechanism/steps used and also on the initiation of NWs growth within the solution, such as slip-coating, spin-coating, solution-dipping, colloidal synthesis, oriented attachment under external conditions, ultrasonic-assisted synthesis, polar solvent/surfactant-assisted synthesis, template-assisted synthesis, nanochannel-assisted synthesis, etc.

https://doi.org/10.1021/acsaem.1c03284
ACS Appl. Energy Mater. 2022, 5, 1342–1377

1.1.1. Slip-Coating Method. Low-temperature slip-coating synthesis is the primary detailed strategy to obtain perovskite NWs in the solution phase.[37] A schematic of the typical growth of NWs is illustrated in Figure 2a. Briefly, a saturated solution of $MAPbI_3$ in dimethylformamide (DMF) is applied dropwise onto a clean microscope glass slide, and another slide is placed on the top. Excess solution is squeezed out to structure a homogeneous liquid film between two glass slides. Finally, the top glass is slid gradually while fixing the bottom one, and the NWs are formed upon solvent evaporation as reflected by an instant color contrast from yellow to brown-red (inset of Figure 2b). An optical microscopic image of the bottom glass slide (Figure 2b) reveals a network of NWs with a maximum length of up to 16 μm and width of around 50−200 nm. Interestingly, variation in the $MAPbI_3$ precursor solution volume-to-surface ratio yielded different sized nanostructures, from NWs to nano/micro whiskers. However, as-grown NWs have random orientation, broad range size distribution, low packing density, and poor interconnectivity, which need to be controlled and optimized for integrated optoelectronic device applications.

1.1.2. Spin-Coating Method. Spin-coating techniques are generally used for the preparation of thin films of various nanomaterials, organic molecules, and polymers. Also, 3D bulk-phase perovskite thin films were prepared by directly spin-coating the precursor solution (MAX + PbX_2). In contrast to the conventional spin-coating process, a two-step spin-coating was developed to grow $MAPbI_3$ NWs with additional solvent engineering.[49] A schematic elucidation of a two-step NWs growth procedure is depicted in Figure 2c. Initially, a PbI_2 thin film was deposited on a target substrate by spin-coating the PbI_2:DMF solution, followed by spin-coating the methylammonium iodide (MAI):isopropanol (IPA):DMF solution onto the predeposited PbI_2 thin film, and subsequent thermal annealing at 100 °C for 45 min resulted in the formation of NWs (Figure 2d) upon evaporation of the solvent. Growth of 1D NWs occurred through the dissolution followed by the recrystallization process. A well-controlled study revealed that NWs growth gets hampered in the absence of DMF during the second step. Interestingly, the density of NWs increased gradually with a variation in MAI concentration from 0.019 to 0.057 M (Figure 2d−f), and a further increment in MAI concentration to 0.076 M resulted in the disappearance of individual NWs (Figure 2g). These results limpidly establish reliance on MAI concentration for fixed DMF and IPA concentrations for the growth of NWs. A similar trend in perovskite NWs growth was documented with additional DMF solvent engineering by various research groups.[50−53] Furthermore, other polar aprotic solvents such as dimethyl sulfoxide (DMSO) and γ-butyrolactone (GBL) were also investigated to study their influence on the growth of NWs; nevertheless, no development of NWs was observed.[49] Here, DMF played a crucial role in the nucleation and subsequent formation/growth of NWs, in which a small amount of PbI_2 particles would be dissolved from the predeposited thin film by the use of DMF solvent during the second step. Locally dissolved PbI_2 residues became the preferential nucleation site for the growth of 1D NWs. NWs designed from this method show high packing density and good interconnectivity. Haplessly, the high contact resistance between the randomly oriented individual NWs increases the device series resistance and limits the overall device performance in PVs and PDs.

1.1.3. Solution-Dipping Method. Solution-dipping is a facile method for the synthesis of perovskite NWs with minimal steps. The first perovskite NWs formed by solution-dipping were reported in 2015, where a lead acetate ($PbAc_2$) thin film coated on a glass substrate was immersed in a highly concentrated MAX solution for the formation of perovskite NWs.[40] Initially, the $PbAc_2$ layer reacted with the MAX solution and resulted in the formation of a thin layer of polycrystalline $MAPbX_3$, which was accommodated as a diffusion barrier and averted the further reaction between MAX and remaining unreacted $PbAc_2$ subsisting underneath the top $MAPbX_3$ layer. The slow dissolution of Pb from underneath the $PbAc_2$ film resulted in an intermediate precursor, PbI_4^{2-}. The top thin layer of $MAPbX_3$ served as seed/nucleation sites, and intermediate PbI_4^{2-} promoted the growth of NWs. The resultant NWs have single-crystalline nature with a rectangular cross-section, well-formed facets, lengths up to 20 μm, and width of a few hundred nm.[40] Following a similar procedure, hybrid $MAPbBr_3/MAPbI_3$ as well as all-inorganic $CsPbBr_3$ single-crystalline perovskite NWs were also documented.[54]

Further, Petrov et al. also demonstrated the solution-dipping method for designing perovskite NWs using PbI_2 in place of the $PbAc_2$ thin film.[55] Briefly, first, a PbI_2 thin film was prepared on FTO substrates by a spin-coating process (Figure 2h), followed by annealing at 100 °C for 30 min. During the second step, the PbI_2 thin film was dipped in a mixed solution of MAI:IPA:DMF (Figure 2h) or FAI:IPA:DMF for 3 min, expeditiously rinsed with IPA thrice, and dried in ambient conditions. Subsequently, the film was annealed at 100 °C for 5 min to get the desired $MAPbI_3/FAPbI_3$ NWs (Figure 2i,j). The effects of MAI concentration and dipping time on the growth of NWs were examined and revealed that the MAI concentration does not alter the shape of the NWs; however, prolonged dipping time of up to 30 min resulted in NWs having a smoother surface. Nevertheless, this method was not fruitful for the growth of $MAPbBr_3$, $FAPbBr_3$, and $MAPbCl_3$ from lead bromide or lead chloride as starting compounds using similar conditions as for iodides. It was suggested that I^- is the only anion that forms a stable intermediate compound with MA^+/FA^+, PbI_2, and DMF or that it is the layered structure of PbI_2 that is essential for the formation of the intermediate by intercalation of MAI/FAI and DMF into the PbI_2 thin film. Here, $MAPbI_3$ and $FAPbI_3$ NWs appear to be pseudomorphs, developed through the topotactical transformation of intermediate phases MAI-PbI_2-DMF (Figure 2i) and FAI-PbI_2-DMF, respectively. However, anion exchange of $MAPbI_3/FAPbI_3$ NWs in IPA solutions of MABr, FABr, and MACl yielded $MA/FAPbX_3$ NWs.[55] This work established that, through judicious regulation of the precursors, their concentrations, and reaction conditions, perovskite NWs with various compositions can be realized.

To directly grow $MAPbCl_3$ NWs on a substrate, a MACl:$PbCl_2$:DMF solution was drop-cast on the glass substrate, which was kept in a Petri dish within a beaker containing toluene.[56] The diffusion of perovskite's antisolvent toluene into perovskite solution, followed by evaporation of DMF, induced the nucleation and subsequent growth of $MAPbCl_3$ NWs; however, this process took over 12 h. Further, $MAPbCl_3$ NWs were transformed into $MAPbBr_3$ NWs in the presence of HBr vapor and then into $MAPbI_3$ NWs in HI vapor through halide anion-exchange reactions. A schematic illustration of the whole process (Figure 2k) and fluorescence

https://doi.org/10.1021/acsaem.1c03284
ACS Appl. Energy Mater. 2022, 5, 1342−1377

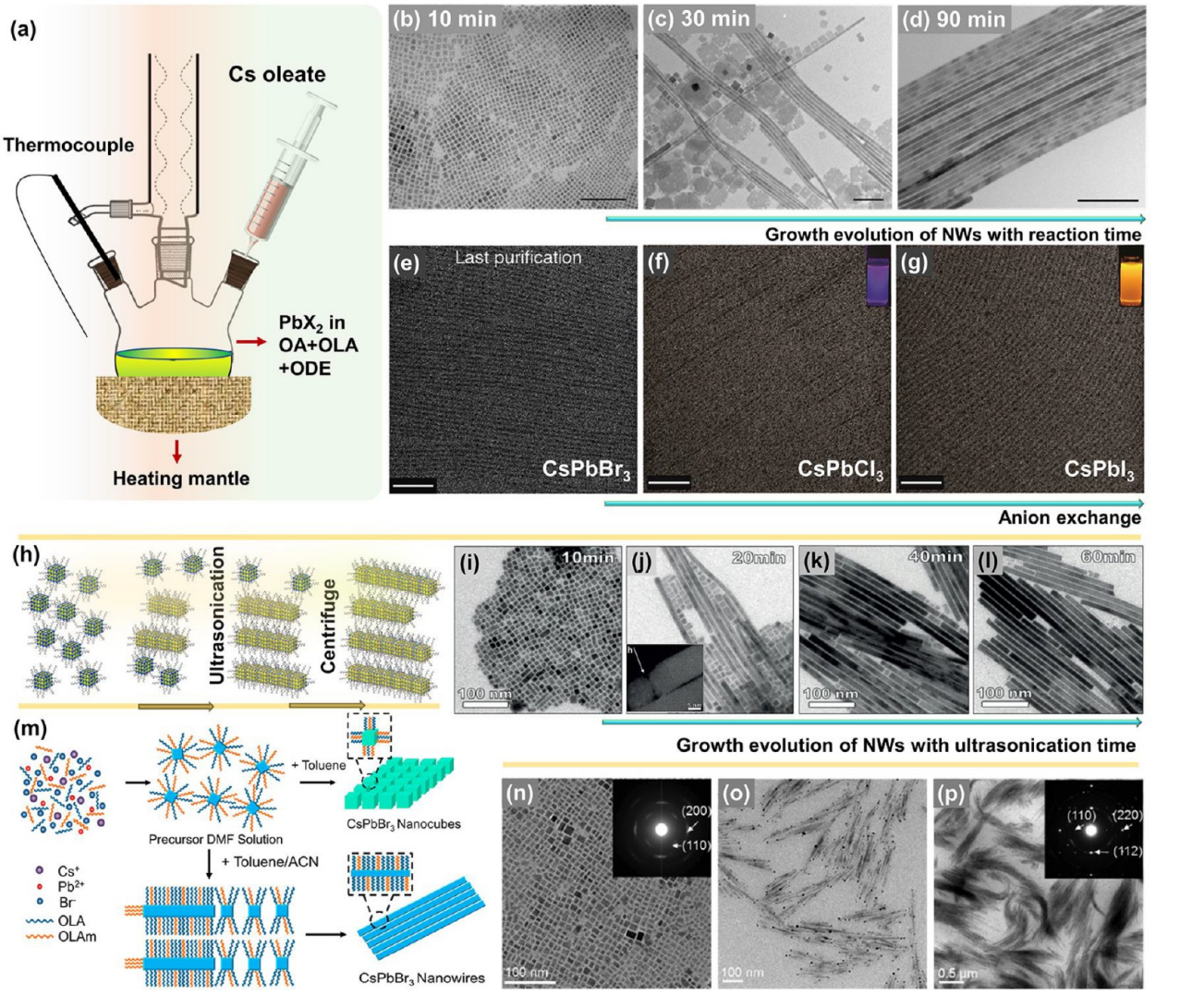

Figure 3. (a) Schematic representation of the synthesis of colloidal NWs through a hot-injection method. (b–d) Shape evolution of perovskite nanostructures from nanocubes into NWs with different reaction times of 10, 30, and 90 min, respectively. Adapted with permission from ref 60. Copyright 2015 American Chemical Society. (e–g) TEM images of ultrathin $CsPbBr_3$ NWs synthesized from a colloidal route after the last purification process and converted into $CsPbCl_3$ and $CsPbI_3$ NWs through Cl^- and I^- halide exchange. The inset shows the colloidal solution of ultrathin $CsPbCl_3$ and $CsPbI_3$ NWs in toluene under UV irradiation of 365 nm. Adapted with permission from ref 61. Copyright 2016 American Chemical Society. (h) Scheme of the initially formed nanocubes from precursor powders transformed into NWs via oriented attachment through an ultrasonication process, followed by centrifugation. Reprinted with permission from ref 65. Copyright 2017 Wiley-VCH. (i–l) Corresponding TEM images of resultant nanostructures at various time intervals formed through an ultrasonication process. Adapted with permission from ref 65. Copyright 2017 Wiley-VCH. (m) Schematic representation of the formation of $CsPbBr_3$ nanocubes in toluene (top panel) and formation of NWs through polar solvent-ACN (bottom panel)-assisted growth method. (n–p) TEM images of $CSPbBr_3$ NWs with mixed solvents containing toluene and ACN at (n) 100:0, (o) 90:10, and (p) 80:20. Insets show the corresponding SAED patterns. Adapted with permission from ref 67. Copyright 2019 American Chemical Society.

microscopic images of $MAPbX_3$ NWs (Figure 2l–n) are depicted. Similar $MAPbI_3$ NWs growth was obtained by using DCM vapor instead of toluene, where as-prepared $MAPbI_3$ NWs showed smoother surfaces than the NWs grown in open-air conditions.[57]

To grow all-inorganic perovskite ($CsPbX_3$) NWs by the solution-dipping method, hydrogen lead iodide ($HPbI_3$) thin films were prepared on FTO substrate by a spin-coating process, followed by dipping in CsI-methanol solution, which resulted in yellow-phase $CsPbI_3$ NWs.[58] Ensuingly, as-formed $CsPbI_3$ NWs were further converted into non-perovskite $CsPbBr_3$ NWs by dipping them in CsBr-methanol solution for halide-exchange reaction, followed by annealing at 150 °C for 10 min, which resulted in the formation of perovskite-phase $CsPbBr_3$ NWs. The resultant NWs have exhibited diameters of 50–100 nm and lengths of up to several μm. It is noteworthy that $HPbI_3$ played a crucial role in the preparation of pristine $CsPbX_3$ NWs, exclusive of any other residual phases, and also exhibited an expeditious growth rate for the formation of NWs compared to the PbI_2-based NWs growth.[58]

Also, all-inorganic $CsPbBr_3$ NWs were prepared from PbI_2 thin film, followed by annealing and submerging the film into a solution of CsBr:methanol.[59] Further, the resultant films were washed twice with IPA and annealed at 50 °C for 5 min for the realization of NWs. Moreover, as-prepared $CsPbBr_3$ NWs were further converted into $CsPbCl_3$ and $CsPbI_3$ NWs through

https://doi.org/10.1021/acsaem.1c03284
ACS Appl. Energy Mater. 2022, 5, 1342–1377

anion-exchange reactions by transferring the individual NWs onto Si/SiO_2 substrates using a nano-manipulator. Besides, multisegmented heterojunctions were engendered with the help of PMMA coating, followed by electron beam lithography (EBL) and sequential dipping of NWs into the conversion solution. Finally, the PMMA mask was washed out with the help of chlorobenzene and hexanes. The resultant individual NWs consisted of $CsPbI_3$-, $CsPbBr_3$-, and $CsPbCl_3$-localized segments, as well as alternative segments of $CsPbBr_3$ and $CsPbCl_3$.[59] These spatially resolved multicolor NWs down to a pixel size of 500 nm were highly congruous for the realization of miniaturized multicolor LED and laser applications.

1.1.4. Colloidal Synthesis Method. To grow all-inorganic single-crystalline $CsPbX_3$ perovskite NWs with diameter down to 10 nm, wityh better control over the size, uniform distribution, high quality, and well-defined morphology, colloidal synthesis of $CsPbX_3$ NWs was reported for the first time in 2015.[60] $CsPbX_3$ NWs were obtained by reacting cesium oleate with lead halide in the presence of oleic acid (OA) and oleylamine (OAm) in octadecene (ODE) at 150−250 °C under air-free conditions (Figure 3a) and thereafter quenching the reaction using an ice−water bath. The reaction product was subjected to centrifugation to disunite the NWs and washed twice with hexane, and finally uniform single-crystalline $CsPbBr_3$ NWs (diameter ∼10 nm) were obtained. Controlled experiments were performed to understand the growth mechanism by changing the growth temperature, growth duration, surfactants, and precursors' concentration in the reaction mixture. Figure 3b−d depicts the shape evolution of as-prepared $CsPbBr_3$ nanostructures and formation/growth of NWs at different reaction times. Also, changing volume of OAm in the reaction solution improved the yield from 10% to 70%, which revealed that the NWs' formation most likely proceeds through a surfactant-directed 1D growth mode. During the reaction, OA was essential for coordinating with Pb^{2+} and decomposing the precursor to form monomers. Here, OAm served as a capping ligand for Pb^{2+} to reduce the reactivity of Pb^{2+} precursor and maintained a higher monomer concentration after the nucleation stage, which was essential for anisotropic growth of 1D NWs.[60]

On augmentation, the same group slightly modified the colloidal synthesis route and purification process to grow, purify, and achieve highly uniform single-crystalline $CsPbBr_3$ NWs with diameters down to 2.2 ± 0.2 nm, which is well below the exciton Bohr radius of $CsPbBr_3$ (7 nm).[61] The reaction product was further purified using different volumes of ethyl acetate (EA) as antisolvent to gradually separate other impurities from the reaction mixture to achieve ultrathin $CsPbBr_3$ NWs. Figure 3e shows the TEM image of $CsPbBr_3$ NWs obtained in the last purification process. Moreover, ultrathin $CsPbBr_3$ NWs were further converted into $CsPbCl_3$ or $CsPbI_3$ NWs through an anion-exchange reaction (Figure 3f,g).[61] Similar growth methods were also reported for the preparation of all-inorganic perovskite NWs such as $Cs_3Sb_2X_9$ and Cs_2SnI_6.[62,63]

1.1.5. Oriented Attachment Growth Method. Oriented attachment, another effective method for the growth of various NWs, was first discovered in 1998.[64] Here, nanoparticles (NPs)/nanocrystals (NCs) with common crystallographic orientations directly combine to form the larger ones that result in the growth of one-directional NWs. Formation of $CsPbX_3$ NWs through the oriented attachment of nanocubes was first observed in a single-step ligand-mediated synthesis route (Figure 3h).[65] $CsPbBr_3$ NWs were formed through prolonged ultrasonication of Cs_2CO_3 and $PbBr_2$ powders dissolved in octadecene in the presence of OAm and OA. To comprehend the growth mechanism and evolution of NWs, ultrasonication was carried out for different periods. As the ultrasonication time progressed further, NWs began to emerge with lengths on the order of 1−3 μm at the expense of nanocubes. Intriguingly, the lateral dimensions of NWs were comparable to those of initially formed nanocubes. Morphological evolution through TEM examination of the intermediate and final products revealed the formation of NWs through the oriented attachment of initially grown $CsPbBr_3$ nanocubes (Figure 3i−l). Moreover, a HAADF-STEM image of a $CsPbBr_3$ NW also corroborated the oriented attachment of a nanocube onto the intermediate NW with a Pb−Br atom layer at their interface (inset of Figure 3j). In augmentation, $CsPbCl_3$ and $CsPbI_3$ NWs were also prepared from as-synthesized $CsPbBr_3$ NWs through halide ion-exchange reactions.[65]

1.1.6. Polar-Solvent-Assisted Growth Method. Polar-solvent-assisted growth of NWs is similar to the oriented attachment of nanocubes, the only difference being the presence of additional polar solvent molecules triggering the development of NWs through induced lattice distortions within the ligand-stabilized cubic $CsPbI_3$ nanocubes.[66] Here, the induced dipole moment on $CsPbI_3$ nanocubes via lattice distortions is intrinsically absent, provided the symmetry is unbroken. The dipole−dipole force drives the nanocubes to self-assemble and recrystallize into a single-crystalline NW having its width the same as that of a nanocube under the oriented attachment mechanism, supplemented by the phase transition from cubic into orthorhombic phase.[66] Pristine, initial $CsPbI_3$ nanocubes were synthesized via a colloidal synthesis route, followed by introducing the polar solvents such as ethanol, methanol, isopropanol, and methyl acetate into the dispersion of $CsPbI_3$ nanocubes in hexane, from which ensued the formation of 1D NWs.[66]

Similarly, to grow the $CsPbBr_3$ NWs via a polar-solvent-assisted growth method, an optimal amount of acetonitrile (ACN) was introduced into the antisolvent toluene at room temperature (RT), which activated the faster growth of NWs by means of supersaturated recrystallization.[67] Fascinatingly, nanocubes were formed in the absence of ACN. Finally, the NWs were formed upon the addition of perovskite precursor solution prepared in DMF to the mixed solution of toluene/ACN drop-by-drop under continuous stirring. The polar solvent acts as a structure-directing agent and additionally restricts the crystal growth along certain facets while facilitating the growth along other facets, thereby leading to the formation of anisotropic 1D NWs.[66,67] A schematic illustration of the polar-solvent-assisted growth mechanism for perovskite NWs is shown in Figure 3m. TEM images also revealed the influence of ACN in toluene for the formation of various nanostructures, where the absence of ACN resulted in perovskite nanocubes (Figure 3n) and the presence of ACN resulted in 1D NWs (Figure 3o,p). Besides, the polar solvent not only promoted the 1D growth but also accelerated the faster halide anion-exchange reaction for the conversion of $CsPbBr_3$ NCs to $CsPbCl_3$ NCs in a short period.[67]

To understand the definitive role of polar solvent in the formation of NWs and its growth mechanism, different solvents were tested. However, no formation of NWs was observed with the addition of methanol (nanodots), ethanol

https://doi.org/10.1021/acsaem.1c03284
ACS Appl. Energy Mater. 2022, 5, 1342−1377

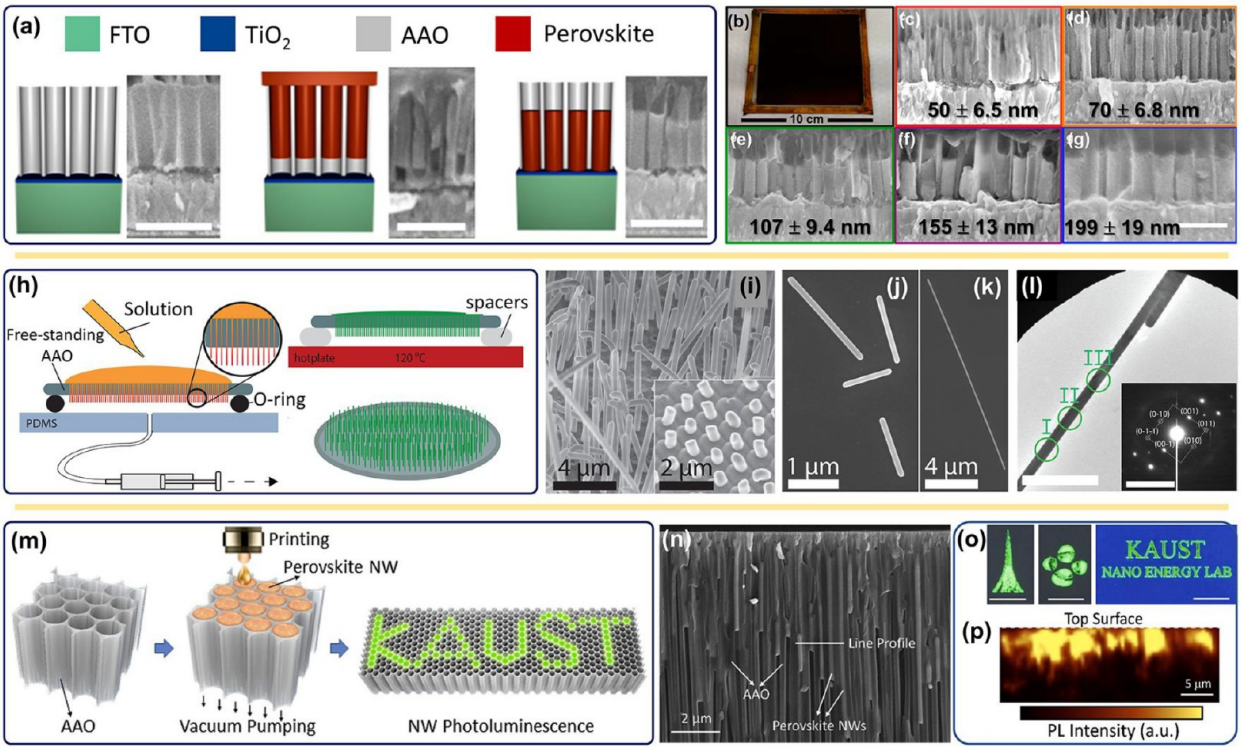

Figure 4. (a) Schematic illustration of the growth of a perovskite NWs array in an anodized aluminum oxide (AAO) template.[68] (b) Digital photograph of a 9 × 9 cm NW array.[68] Cross-sectional SEM images of NWs with diameters of (c) 50.3 ± 6.5 nm, (d) 70.0 ± 6.8 nm, (e) 107 ± 9.4 nm, (f) 155 ± 13 nm, and (g) 199 ± 19 nm. Scale bar is 500 nm.[68] Adapted with permission from ref 68. Copyright 2016 American Chemical Society. (h) Scheme of the growth method of perovskite NWs via an extrusion process. (i) SEM image of vertical NWs. The inset shows shorter NWs achieved when the template is exposed to pressure gradient for shorter times. (j, k) High-magnification SEM images of horizontal NWs with different lengths. (l) Bright-field TEM image of a single NW. The inset shows the SAED pattern at location I. Adapted with permission from ref 69. Copyright 2017 American Chemical Society. (m) Schematic of the printing process for the growth of perovskite NWs within the nanoporous template. (n) Cross-sectional SEM image of perovskite NWs in pores of the AAO template. (o) Optical images of printed perovskite NWs with various patterns under UV irradiation. (p) Cross-sectional PL mapping of perovskite NWs. The scale bars are 5 mm.[70] Adapted with permission from ref 70. Copyright 2020 Elsevier.

(nanoplatelets), benzyl alcohol (large aggregates), and anisole (nanocubes), which indicated a plausible interaction between $CsPbBr_3$ nanocubes and ACN that governed the anisotropic growth of $CsPbBr_3$ NWs.[67] Importantly, the dielectric constant of ACN solvent being higher than those of the other solvents that could easily wash the OAm ligands from certain facets of $CsPbBr_3$ nanocubes was anticipated to promote the anisotropic 1D growth of NWs.[67]

1.1.7. Template-Assisted Growth Method. Generally, the position and orientation of NWs grown in solution phase are resolved by the formation of random nucleation centers, where the NWs desultorily distribute throughout the substrate area with voids, different aspect ratios, and irregular position and orientation. Hence, to control and regulate the position, length, orientation, and directional growth of the NWs, templates were utilized as frames/scaffolds to guide the growth of NWs within the pores of the template. The NWs' diameter can be regulated by ultimately tuning the pore diameter of the template. Template-assisted growth of perovskite NWs in the solution phase was implemented with dripping,[68] extrusion,[69] and inkjet-printing processes.[70]

Ashley et al. demonstrated the template-assisted growth of perovskite NWs by employing an AAO template on a TiO_2-coated FTO conductive substrate.[68] Perovskite precursor solution was added to the template and allowed to penetrate into the pores of the AAO, followed by dripping a solution of DMSO:chlorobenzene on top of the rotating AAO template. This supplemental step abstracted the excess precursor solution from the AAO surface and drew the precursor into AAO pores via capillary and centrifugal forces. Annealing of AAO/substrate resulted in evaporation of the solvent, and subsequent recrystallization led to the formation of NWs within the template pores (Figure 4a). Resultant NWs were oriented perpendicular to a substrate, and the diameter was regulated by employing a specific AAO pore diameter (50–200 nm) (Figure 4c–g). The researchers applied a similar procedure for the growth of NW arrays of compositions such as $MAPbI_3$, $MAPbBr_3$, and Cs_2SnI_6.[68]

To grow free-standing vertical perovskite NWs from the solution phase, an extrusion process was employed in contrast to embedding the NWs within the pores of the template/matrix.[69] Here, NWs' growth initiates from an AAO template with well-defined pore size with both the sides open. Briefly, the AAO template was placed on an O-ring on a polydimethylsiloxane (PDMS) substrate; a pressure difference was established with the help of a syringe (Figure 4h). Perovskite precursor solution was drop-cast onto a free-standing AAO template to fill the pores, where a low-pressure region was created between PDMS and AAO with the help of the O-ring and syringe. Due to the pressure gradient, the perovskite solution expeditiously packs the AAO template pores from the top and extrudes out from the bottom of the

https://doi.org/10.1021/acsaem.1c03284
ACS Appl. Energy Mater. 2022, 5, 1342–1377

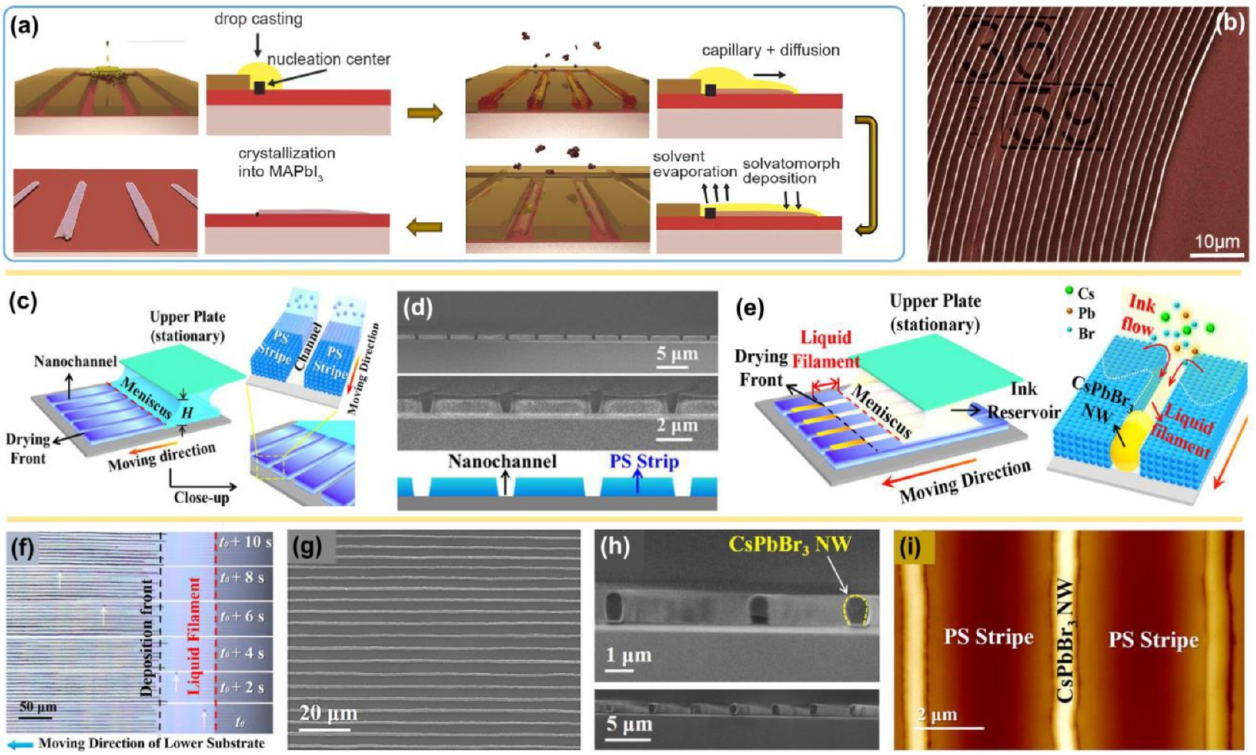

Figure 5. (a) Pictorial illustration of the growth of parallelly aligned $MAPbI_3$ NWs in nanofluidic channels, where the saturated $MAPbI_3$ solution is drop-casted, driven by the capillary forces, and followed by the nucleation and further growth of NWs within the channels. (b) Colored SEM image of aligned $MAPbI_3$ NWs array. Adapted with permission from ref 72. Copyright 2016 Nature Publishing Group. (c) Graphical representation of the formation of nanochannels through solution-printing of a PS latex NPs aqueous suspension. (d) Corresponding side-view SEM images of the as-formed nanochannels. (e) Scheme of the formation of $CsPbBr_3$ NWs in nanochannels via a meniscus-assisted printing process. (f) Optical microscopic images of the growth of NWs as a function of time. (g) SEM images of the perovskite NWs array after the removal of PS stripes. (h) Cross-sectional SEM images of NWs array with high and low magnifications. (i) Atomic force microscopy (AFM) image of $CsPbBr_3$ NWs existing within the nanochannels of PS strips. Adapted with permission from ref 74. Copyright 2020 Wiley-VCH.

AAO template. Further, the careful transfer of AAO template with extruded perovskite NWs onto the glass spacers, followed by annealing at 120 °C, resulted in the formation of 1D perovskite NWs. The length of the perovskite NWs was directly influenced by the time as well as the pressure gradient to which the template was subjected. Upholding the pressure gradient for longer and shorter periods resulted in longer and shorter length NWs, respectively (Figure 4i).[69] Figure 4j,k shows dry transfer of extruded perovskite NWs onto a substrate under different periods. Further, TEM studies on a single perovskite NW substantiate the single-crystalline nature, as shown in Figure 4l, and SAED patterns recorded at three various locations on the NW show identical diffraction patterns.

Recently, Lin et al. reported a synthesis procedure similar to that mentioned earlier where the AAO template was packed via inkjet-printing and vacuum-pumping (Figure 4m),[70] in contrast to the above report. Perovskite precursor ink was prepared by mixing equimolar concentration $PbBr_2$:MABr in DMF and then heated at 90 °C for 24 h. Throughout the printing process, a vacuum pump was used beneath the AAO template to guide the perovskite ink into the pores of the AAO. Finally, the AAO template filled with perovskite ink was annealed at 90 °C for 2 h to dry the perovskite NWs within the AAO pores, and the corresponding SEM image is shown in Figure 4n. Optical microscopic images of different printing patterns of perovskite NWs within the AAO template under UV illumination (Figure 4o) and a PL image of AAO pores containing the perovskite NWs (Figure 4p) are presented. This template method makes it possible to grow NWs within the pores along with oriented guidance, tunable diameter, and uniform alignment, which improves the stability of NWs by protecting them against moisture via the surrounding template material. The printing process is high quality, simple, and inexpensive and allows for a rapid fabrication process that can enable mass production for device applications.

In contrast to the AAO template, a PDMS rectangular groove template (RGT) was utilized to grow the array of NWs on arbitrary substrates.[71] Spatially confined template allowed for the directional growth of $MAPbBr_3$ NWs along the template grooves. This method produced horizontally aligned, uniform geometries and highly ordered perovskite NWs.

The template method establishes a route to develop oriented perovskite NWs arrays of various compositions, which could be methodically modified in terms of their length, spacing, and diameter from the judicious selection of the AAO template. Also, the presence of template material provides additional protection from the surroundings, where the moisture/water molecules can only diffuse vertically from the top surface of the NWs, leading to a slower decomposition rate, which resulted in the enhanced stability of NWs existing within the template pores.

1.1.8. Nanochannel-Assisted Growth Method. To selectively grow the NWs with a spatial position, liquid−solid growth of perovskite NWs through a graphoepitaxial method was achieved within the pre-patterned open nanofluidic

https://doi.org/10.1021/acsaem.1c03284
ACS Appl. Energy Mater. 2022, 5, 1342−1377

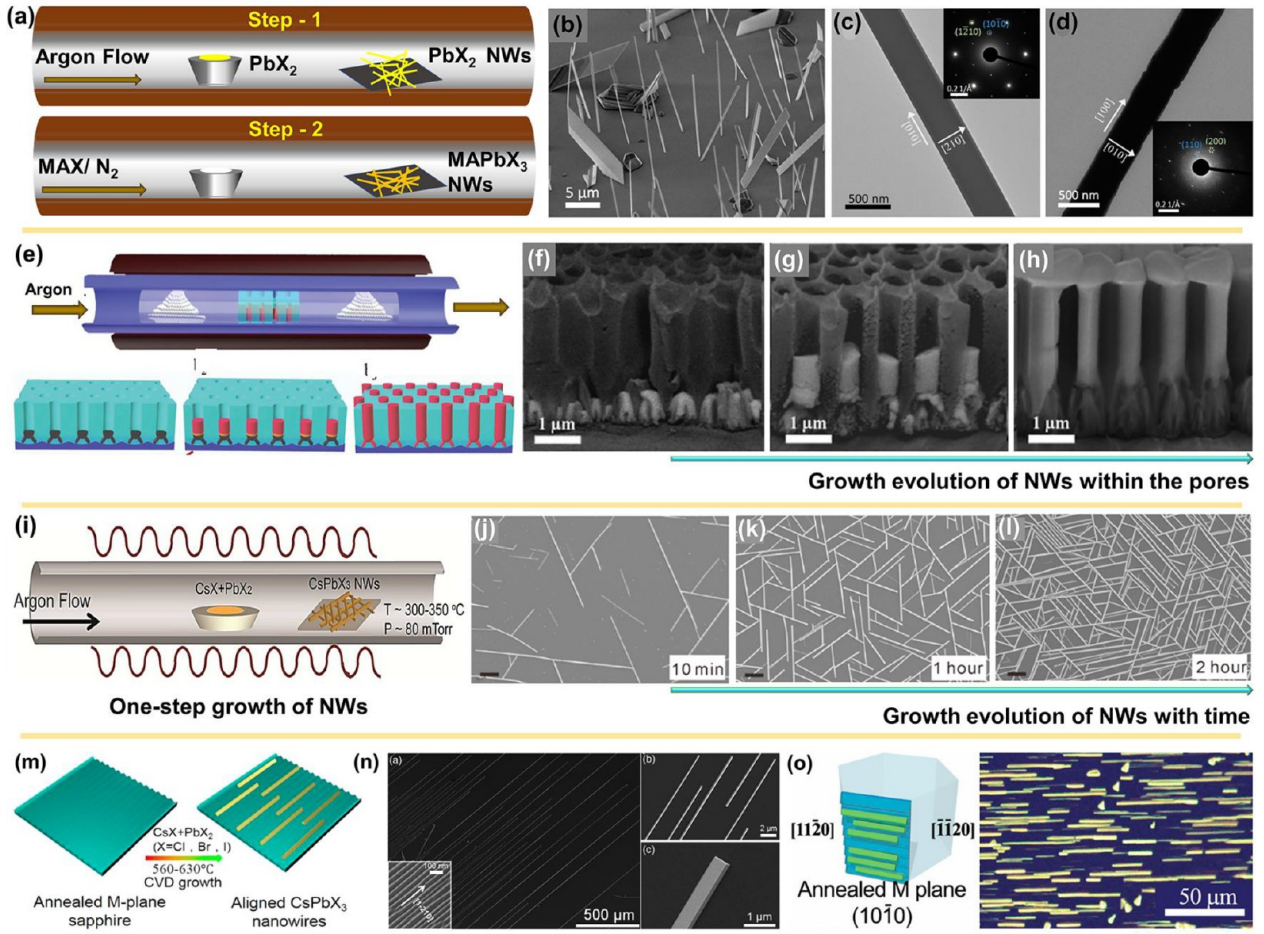

Figure 6. (a) Schematic of a two-step growth of perovskite NWs. (b) SEM image of PbI_2 NWs grown via the first step on a silicon substrate. (c, d) TEM images of PbI_2 and final $MAPbI_3$ NWs. The inset shows the corresponding SAED patterns. Adapted with permission from ref 76. Copyright 2015 American Chemical Society. (e) Schematic of a CVD process for perovskite NWs growth in a template. The bottom images show a schematic of the initial, intermediate, and final stages of the template during the growth of NWs. (f–h) Cross-sectional SEM images of the AAO template at different growth durations. Adapted with permission from ref 77. Copyright 2017 Royal Society of Chemistry. (i) Schematic of the one-step growth of perovskite NWs. (j–l) SEM images of $CsPbBr_3$ NWs and their network grown on p-mica with different reaction time from 10 min to 2 h. Adapted with permission from ref 79. Copyright 2017 American Chemical Society. (m) Schematic of the graphoepitaxial growth of NWs on M-plane sapphire substrate. Adapted with permission from ref 86. Copyright 2018 American Chemical Society. (n) Different magnification SEM images of the directional $CsPbBr_3$ NWs grown along the faceted M-plane sapphire. Adapted with permission from ref 85. Copyright 2017 American Chemical Society. (o) Graphoepitaxial growth of $CsPbBr_3$ NWs and dark-field optical microscopic image of grown NWs. Adapted with permission from ref 87. Copyright 2018 American Chemical Society.

channels on an etched Si substrate.[72] A schematic illustration of the growth procedure of NWs is shown in Figure 5a. Briefly, a saturated $MAPbI_3$:DMF solution was dropped onto one side of the pre-patterned nanochannels array-Si substrate. The perovskite solution then diffused into nanochannels through capillary forces. Formation of stable clusters of nuclei of intermediate-phase $MAPbI_3$:DMF within the channel entrances initiated the growth of NWs within nanochannels. Solvent-evaporation-induced supersaturation-driven recrystallization was responsible for the successful growth of $MAPbI_3$ NWs. Figure 5b shows a colored SEM image of ultralong $MAPbI_3$ NWs. Later, a similar method was also implemented by Zhou et al. for the growth of $MAPbI_3$ NWs.[73]

To obtain an array of aligned and crystalline perovskite NWs on desired substrates through the solution-printing process, a capillary-assisted solution-printing (CASP) technique was employed.[74] A schematic representation of the printing-assisted channel formation and subsequent growth of NWs is depicted in Figure 5c–e. Briefly, the meniscus-assisted solution-printing of polystyrene (PS) latex NPs in an aqueous suspension yielded aligned, periodic cracks (i.e., nanochannels separated by PS stripes) over a large area (Figure 5c,d). These printed nanochannels were utilized for the subsequent growth of perovskite NWs through CASP from the perovskite precursor solution, indicating a yellow appearance that signifies the formation of $CsPbBr_3$ NWs (Figure 5e).[74] Finally, PS stripes were dissolved with toluene, followed by annealing at 250 °C, resulting in the formation of a perovskite NWs array. Corresponding optical microscopic, SEM, and AFM images of the aligned perovskite NWs are depicted in Figure 5f–i, which reveal the formation of uniformly aligned and crack-free NWs. Perovskite NWs designed from this nanochannel-assisted growth method possessed controlled size, cross-sectional shapes, aspect ratios, position, and orientation, which are highly desirable for the scale-up fabrication and subsequent device integration.

Solution-phase synthesis methods of perovskite NWs demonstrated remarkable advantages in fabricating large-area

https://doi.org/10.1021/acsaem.1c03284
ACS Appl. Energy Mater. 2022, 5, 1342–1377

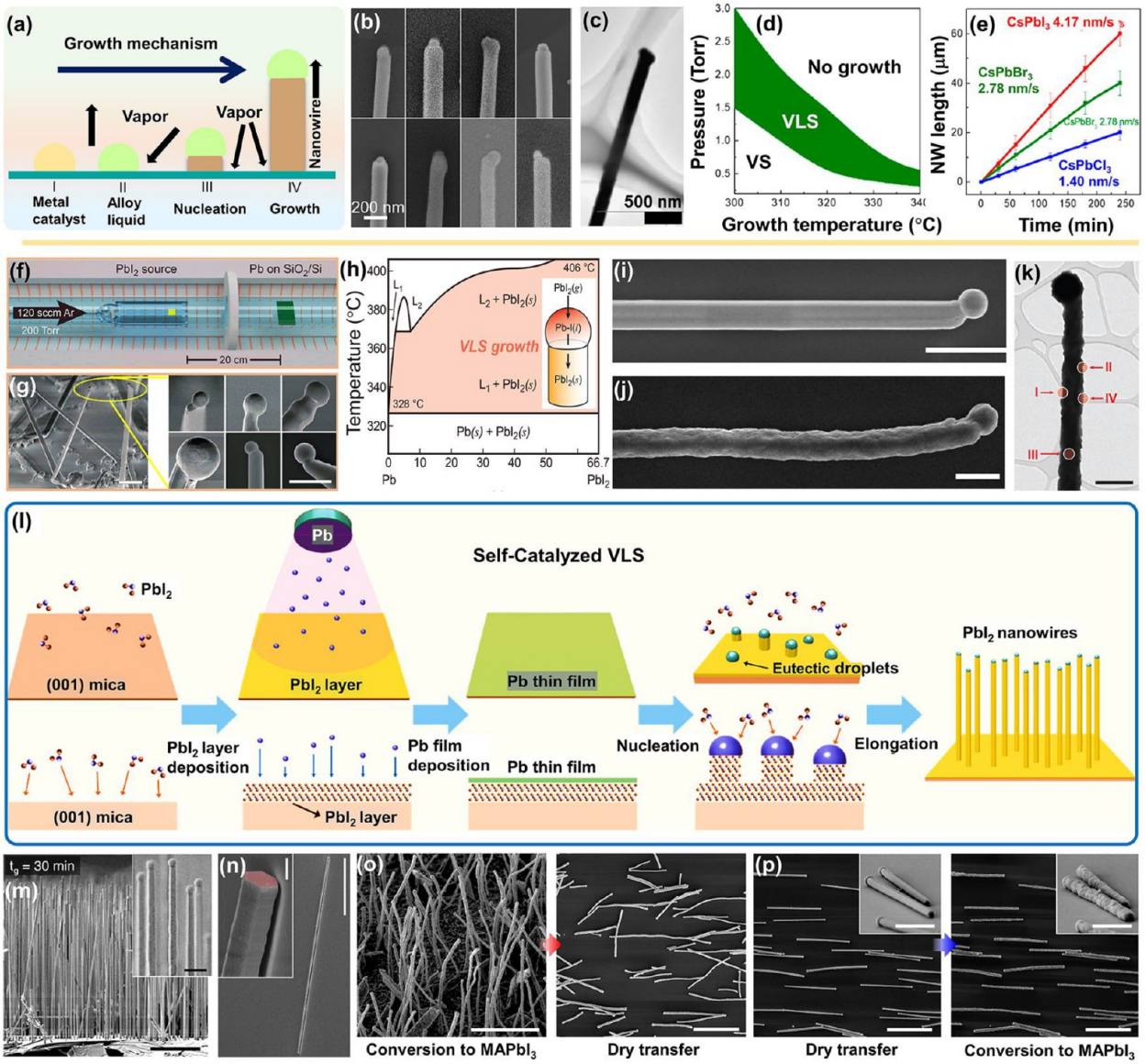

Figure 7. (a) Schematic representation of catalyst-based VLS growth mechanism of perovskite NWs. (b) SEM images of individual $CsPbBr_3$ NWs grown with Sn as catalytic seeds. (c) TEM image of VLS-grown $CsPbCl_3$ NWs with a catalytic tip. (d) VLS growth window for $CsPbBr_3$ NWs versus temperature and pressure. (e) Length of $CsPbX_3$ NWs versus the growth time. Adapted with permission from ref 91. Copyright 2019 American Chemical Society. (f) Schematic of CVD reactor with two different temperature zones (source powder, left, and growth substrate, right) for NWs growth. (g) Tilt-view SEM image of NWs grown on the substrate; scale bar, 5 μm. SEM images of PbI_2 NWs containing spherical Pb tips at the top of the NW; scale bar, 1 μm. (h) Pb−I binary-phase diagram: shaded region is the area where a liquid Pb droplet supersaturates with I and acts as a catalyst for the growth of NWs. The inset is a schematic of the VLS growth of PbI_2 NWs. (i) SEM image of a VLS-grown individual PbI_2 NW with a Pb catalyst tip; scale bar, 1 μm. (j) Corresponding SEM image of a converted $MAPbI_3$ NW; scale bar, 1 μm. (k) TEM image of a $MAPbI_3$ NW; scale bar, 500 nm. Adapted with permission from ref 92. Copyright 2017 American Chemical Society. (l) Diagrammatic illustration of the self-catalyzed VLS growth of PbI_2 NWs. (m) Side- and 45° tilt-view (inset) SEM images of epitaxially grown PbI_2 NWs from the PbI_2/mica substrate for 30 min. Scale bars, 10 μm. (n) 45° tilt-view SEM image of a PbI_2 NW dry-transferred onto SiO_2. Scale bar, 10 μm. The inset shows a magnified image of the bottom of a NW with a hexagonal cross-section (false-colored in red); scale bar, 200 nm. (o, p) SEM images of conversion-sequence-dependent morphology of $MAPbI_3$ NWs, where the vertically grown NWs first converted into $MAPbI_3$ and were then dry-transferred, and vice versa. Adapted with permission from ref 93. Copyright 2019 American Chemical Society.

and NWs-array-based devices for advanced optoelectronic applications.[75] However, perovskite NWs may be influenced by the presence of organic ligands or surfactants during the synthesis process, which will further affect the NWs' physical, optical, and electronic properties due to their insulating nature. Besides, to obtain better crystallinity and lower defect density, the vapor-phase methods were employed by many other groups for the preparation of perovskite NWs.

1.2. Vapor-Phase Synthesis of Perovskite NWs.

Alternatively, the preparation of perovskite NWs through vapor-phase growth offers great potential for precise control over the crystallinity, morphology, dimension, and composition. Chemical vapor deposition, epitaxial growth, graphoepitaxial growth, and vapor−liquid−solid growth techniques were extensively followed for the preparation of perovskite NWs and demonstrated high-quality single-crystalline perovskite NWs.

https://doi.org/10.1021/acsaem.1c03284
ACS Appl. Energy Mater. 2022, 5, 1342−1377

1.2.1. Chemical Vapor Deposition (CVD) Method. Xing et al. demonstrated a two-step CVD procedure for the synthesis of highly crystalline $MAPbI_3$, $MAPbBr_3$, and $MAPbI_xCl_{3-x}$ perovskite NWs (Figure 6a).[76] Briefly, at first, PbI_2 NWs were directly grown on SiO_2/Si substrate by evaporating the PbI_2 powder in a thermal CVD tube furnace at 380 °C and 200 Torr pressure for 15 min. Figure 6b,c shows SEM images of the obtained PbI_2 NWs on SiO_2/Si substrate, where PbI_2 NWs were grown vertically on the substrate with a rectangular or nearly square cross-section with an aspect ratio ranging from 1 to 20. Further, as-prepared PbI_2 NWs (Figure 6c) were converted into $MAPbI_3$ NWs in the same CVD system through a gas−solid heterophase reaction with the help of MAI, where MAI vapor molecules were intercalated into the interval sites of PbI_6 octahedron layers and resulted in the formation of perovskite NWs (Figure 6d). The geometry of the converted perovskite NWs still holds the same shape with a slightly higher roughness than the initial PbI_2 NWs (Figure 6c,d). SAED pattern analysis confirmed the single-crystalline nature of both the PbI_2 and $MAPbI_3$ NWs (inset of Figure 6c,d). By following a similar procedure with slight changes in the tube furnace growth conditions, preparation of $MAPbBr_3$, $MAPbCl_3$, $MAPbI_xBr_{3-x}$, and $MAPbBr_xCl_{3-x}$ perovskite NWs was also demonstrated.[76] To grow array of NWs with a precisely controlled geometry within the pores of the AAO template, a CVD method was employed.[77,78] Initially, the AAO template was prepared by a two-step anodization followed by electrodeposition of Pb/Sn metal catalyst on one side of the AAO template. The metal-catalyst-deposited AAO template was kept at the center of the tube furnace, and two quartz containers consisting of MAI powder were placed on either side of the furnace (Figure 6e).[77] During annealing at 180 °C, evaporated MAI molecules diffused into the bottom of the AAO nanochannels/pores and reacted with metal catalyst particles. The process was continued for 3 h to form the full-fledged perovskite NWs within the AAO pores. Figure 6f−h shows the growth evolution of 1D perovskite NWs within the AAO pores for different time intervals. At first, MAI vapor reacts with Sn/Pb catalyst within the template to form initial PbI_2/SnI_2 NWs, and then the excess MAI vapor reacts with PbI_2/SnI_2 to form $MAPbI_3$ or $MASnI_3$ NWs.[77] It is a vapor−solid−solid (VSS) process in which MAI vapor diffuses downward through solid NWs to form the perovskite NWs within the pores of the AAO template.

To reduce the number of steps involved in the growth of perovskite NWs, Chen et al. demonstrated a single-step CVD process for the epitaxial growth of horizontally oriented $CsPbX_3$ NWs or NWs networks (Figure 6i).[79] Here, epitaxial growth of in-plane $CsPbX_3$ NWs with controlled crystallographic orientations on the (001) plane of phlogopite (p-mica) or muscovite mica (m-mica) substrates was achieved. Briefly, a mixture of CsX and PbX_2 powders with a molar ratio of 1:1 was placed in the middle of the heating zone (300−350 °C) of the furnace, where the evaporated precursors were transported by carrier gas onto mica substrate, followed by the growth of surface-bound NWs due to the asymmetric lattice match between $CsPbBr_3$ and mica along the different crystallographic directions. A variety of $CsPbBr_3$ structures, including single wires, Y-shaped branches, networks, and nearly continuous epitaxial $CsPbBr_3$ films, were observed for the extended growth durations (Figure 6j−l). Similarly, various groups have also achieved well-defined epitaxially grown ultrathin $CsPbX_3$ NWs arrays and $MAPbX_3$ NWs arrays on m-mica or Si/SiO_2 substrates by a facile CVD method.[80−84]

Similarly, a single-step CVD method was employed to grow in-plane-aligned ultralong directional single-crystalline NWs using the graphoepitaxial effect on annealed M-plane (Figure 6m) and C-plane sapphire substrates.[85−88] It involves a specific substrate with nanogrooves/steps on its surface, oriented in a particular direction. Graphoepitaxially nucleated nanocrystal seeds generated by the vapor precursor continue to grow into directional NWs with particular orientation along the pre-defined shaped nanogrooves via the graphoepitaxial effect, driven by the maximum interface area between the substrate and NWs. Briefly, a mixture of CsBr and $PbBr_2$ powders was placed at the center of a heating zone, and annealed M-plane sapphire substrates were loaded into a tube furnace in a silica boat downstream. At elevated temperatures, evaporated CsBr and $PbBr_2$ vapors were transported to the substrates zone, followed by deposition and nucleation of seeds on the sapphire substrate methodically due to the van der Waals epitaxy of the substrates that drive the formation of NWs.[85,86] Figure 6n shows different magnification SEM images of the obtained $CsPbBr_3$ NWs on M-plane sapphire substrate. Here, all the perovskite NWs were grown along the pre-defined grooves on an M-plane sapphire substrate with a triangular cross-section, which was thermodynamically favorable by exposing the (100) surfaces with low surface energy. Similarly, Oksenberg et al. also reported the graphoepitaxial growth of $CsPbBr_3$ NWs (Figure 6o).[87] Perovskite NWs achieved from CVD growth methods are believed to be highly favorable and desirable for device integration owing to their high quality and single-crystalline nature.

1.2.2. Vapor−Liquid−Solid (VLS) Method. The VLS method is another category of vapor-phase growth of NWs, where either external catalyst particles or one of the constituent elements itself (acting as a catalyst) guides the development of NWs.[89,90] Figure 7a schematically describes the catalyst-based VLS growth mechanism of NWs. Briefly, small catalyst particles are situated on a substrate within the tube furnace/vacuum chamber and heated to opportune temperatures in the presence of precursor materials. As the precursor vapor approaches a catalyst particle, a small alloy droplet is formed with the vapor atoms of the precursor material, which further continues to enter the liquid alloy droplet and is dissolved in it until the supersaturation stage is reached. After reaching supersaturation, the alloy particle precipitates the precursor atoms in order to re-establish the stable composition of catalyst and precursor within the binary liquid alloy. During the growth process, the alloy droplet detaches/displaces from the substrate and rides on top of the growing NW, and the NW continues to grow in length until the catalyst is consumed or the growth conditions are changed. Here, crystallization takes place at the liquid−solid interface, whereas in vapor−solid growth, crystallization takes place at the vapor−solid interface. The main advantages of this method include the regulation of the NW's diameter through the selection of the size of catalyst particle, tuning the length of the NW through the growth duration, position-selective growth of NWs by patterning the catalyst particles, and growth of multisegment heterostructure NWs.

In a typical study, all-inorganic halide perovskite $CsPbX_3$ NWs were synthesized through a Sn-catalyzed VLS growth method.[91] Briefly, for the growth of NWs, CsX:PbX_2 mixed powder was evaporated in a quartz tube furnace, where the

https://doi.org/10.1021/acsaem.1c03284
ACS Appl. Energy Mater. 2022, 5, 1342−1377

evaporated atoms were deposited onto the Sn-catalyst-coated substrates kept in the low-temperature heating zone of a two-zone CVD system. The NWs' growth preceded through supersaturation of Cs and Br in the liquid Sn−Pb alloy catalyst particle. SEM and TEM images confirmed the growth of defect-free single-crystalline NWs, and the physical emergence of a spherical catalyst particle on top of the NWs corroborates the VLS growth mechanism (Figure 7b,c).

The growth of NWs through the VLS mechanism is mainly affected by their growth temperature, growth pressure, and growth duration (Figure 7d,e).[91] Growth-pressure variation for a fixed growth condition established that the threshold growth pressure is beneficial to suppress the evaporation of source materials to promote efficient VLS growth. Further increment in the growth pressure beyond the threshold value suppresses VLS growth and promotes VS growth that results in the formation of shorter NWs.[91] A growth-temperature-controlled study also confirmed a narrow growth window for the preparation of $CsPbX_3$ NWs.[91] At lower growth temperatures, the VS growth mechanism dominates over VLS growth and also shortens the diffusion length of adatoms which fall on the substrate and sidewalls of NWs. At elevated growth temperatures, evaporation of alloy particles and re-evaporation of the adatoms lead to the complete absence of NWs. Similarly, the growth rate is also different for dissimilar halide-based perovskite NWs. $CsPbI_3$ NWs exhibited a higher growth rate than $CsPbBr_3$ and $CsPbCl_3$ NWs (Figure 7e), which is highly dependent on the melting points of the precursor compounds.[91] Hence, it is crucial to maintain a favorably narrow window for the effective growth of perovskite NWs using the VLS growth method.

1.2.3. Self-Catalyzed VLS Method. In contrary to a catalyzed VLS growth method, one of the constituent element itself acts as a catalyst for the growth of NWs, which is coined as self-catalyzed VLS growth.[92] Akin to a VLS mechanism, the only difference is whether the catalyst particle is a foreign element or a constituent element of the material's composition.

Mayers et al. were the first to report the growth of perovskite NWs by a self-catalyzed VLS method,[92] where two steps were involved for the growth of NWs. Concisely, at first, lead halide (PbX_2; X = Cl^-, Br^-, I^-) NWs were synthesized by self-catalyzed VLS growth employing Pb as a catalyst particle (Figure 7f). For the growth of PbX_2 NWs, liquid Pb particles were supersaturated with vapor species of Pb and X halide, which resulted in crystallization of PbX_2 NWs at the liquid−solid interface. In the case of PbI_2 NWs growth, Pb forms an alloy with I halides at a temperature above 328 °C (Figure 7g,h). Further, a continuous supply of Pb and I from the evaporation zone resulted in supersaturation of the Pb−I alloy liquid droplet, and PbI_2 precipitated as a NW at the interface of the liquid alloy particle and the solid surface of the substrate (Figure 7g,h). In the second stage, single-crystalline PbX_2 NWs (Figure 7i) were converted into $MAPbX_3$ NWs through a low-temperature vapor-phase procedure. The vapor phase of MAX intercalates and reacts with PbX_2 NWs in a different temperature zone, resulting in the formation of $MAPbX_3$ NWs (Figure 7j). The morphology of the converted $MAPbX_3$ NWs appears with a higher rough surface and a large linear expansion and becomes polycrystalline (Figure 7j,k).

Similarly, Shim et al. also reported the self-catalyzed VLS growth of PbI_2 NWs using PbI_2 thin film as an epitaxial substrate layer (Figure 7l).[93] Here, a PbI_2 thin film was exposed to the flow of additional PbI_2 vapor while heating above the eutectic temperature of the Pb−I system to initiate the formation of catalytic liquid droplets, followed by supersaturation-induced crystallization for the growth of aligned PbI_2 NWs. Figure 7m shows SEM images of the side view and 45° tilt view of PbI_2 NWs grown on PbI_2/mica for a growth time (t_g) of 30 min at 250 °C, where the NWs were mostly oriented in a vertical direction and PbI_2 NWs were dry-transferred onto SiO_2 (Figure 7n). As-grown PbI_2 NWs were further converted into $MAPbI_3$ NWs by exposure to the vapor phase of MAI. However, intercalation of MAI molecules into PbI_2 NWs causes volume expansion of the parent PbI_2 NWs that usually leads to higher roughness and a polycrystalline structure of the converted $MAPbI_3$ NWs (Figure 7o,p).[92,93] Nevertheless, Pb catalyst particles remain intact with the $APbX_3$ NWs as well, which holds them back for device integration.

2. POTENTIAL APPLICATIONS OF PEROVSKITE NANOWIRES

The dimensionality and morphology of semiconductors have consequential influences on their optical and electrical properties, thus determining their applications in various optoelectronic devices. 1D NWs offer several advantages over their thin-film counterparts, including superior antireflection, fast carrier transport, significant light trapping, superior light-harvesting, long photocarrier lifetime, and enhanced mechanical properties that are highly beneficial for improving the performance of various optoelectronic devices.[94−97] Hence, 1D perovskite NWs are widely considered to be one of the most efficacious candidates for optoelectronic device applications.

2.1. Perovskite NWs Photodetectors. Photodetectors (PDs) convert optical signals into electrical signals through the photoelectric effect. PDs have become prominent in various industrial and scientific applications. To exemplify, infrared (IR) PDs are being used in optical communications, remote control, surveillance cameras, night vision, satellite remote sensing, and analytic science; visible (Vis) PDs are used in optical imaging, electronic eyes, chemical/biological sensing; and ultraviolet (UV) PDs are used in the military, environmental monitoring, space science, etc.[98−100] Traditional PDs have been designed from the silicon, III−V group, and II−VI group semiconducting materials that rely on complicated and expensive processes.[101−103] Recently, organic−inorganic metal halide perovskites have received interest for use in PDs owing to their striking properties such as high light absorption coefficients, long charge carrier diffusion lengths, high charge carrier mobilities, and composition-tailored bandgaps in the broad wavelength region.[104−110] However, the efficiency of perovskite PDs has been limited by the trade-off between responsivity, detectivity, and response time of the PDs.[22,111] Efficient photodetection demands a high photocurrent as well as a low dark current. Importantly, a high photocurrent requires highly crystalline materials that induce efficient charge conduction,[112] whereas a low dark current needs intrinsic defects or charge trap states within the material to inhibit the conduction due to thermally excited charge carriers.[113] Thus, it betokens an irony to amalgamate both the better conduction of charge carriers for high photocurrents and high resistance for dark current suppression within a single-phase perovskite material to achieve efficient performance of the PDs. Virtually, the single-crystalline perovskites concurrently produce both high photocurrents and high dark currents.[112] On the other

https://doi.org/10.1021/acsaem.1c03284
ACS Appl. Energy Mater. 2022, 5, 1342−1377

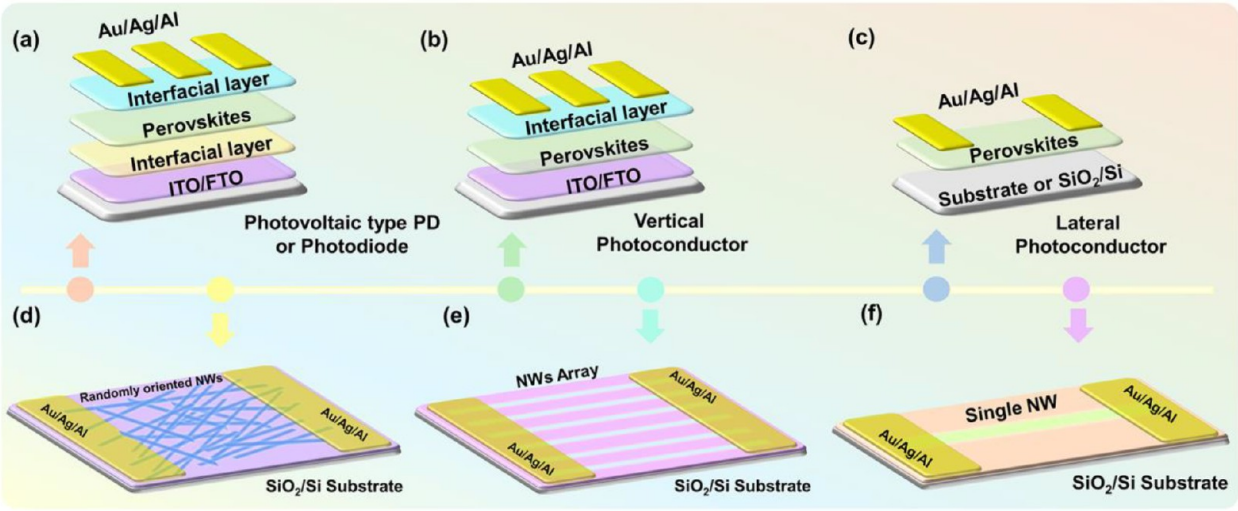

Figure 8. Schematic representation of device configuration of various types of PDs. (a) Photovoltaic type of PD or photodiode. (b) Vertical type of PD. (c) Lateral type of PD. (d) Randomly orientated NWs-based PD. (e) Parallelly aligned NWs array-based PD. (f) Single NW-based PD.

hand, polycrystalline perovskite thin films produce low photocurrents and low dark currents because of the grain boundaries that act as scattering centers,[114] thus leading to low sensitivity and responsivity. Diverse approaches have been employed to improve the performance of PDs.[39,115−118]

Recent studies have demonstrated that one of the best operational methods is to employ 1D perovskite NWs as photoactive material for the construction of the PDs. The unique geometry of the 1D perovskite NWs with high aspect ratio and large surface-to-volume ratio makes them suitable candidates to achieve high performance.[119] Herein, NWs induce high photocurrents because of their crystalline fiber-like structures, and the surface trap states of dangling bonds trap the holes, which delays the recombination of charge carriers. Delay in the recombination of electrons and holes increases the number of times that the electron travels along the NW's length direction, which contributes to the overall current conduction and enhances the internal photoconductive gain. Besides, the active volume of the NWs that produces the dark current, a source of noise, is meager compared to that in thin-film-based PDs.[115,120] Hence, these characteristics make the NWs favorable candidates to achieve efficient photodetection and high sensitivity. Perovskites NW-based PDs have attained high responsivity (R), detectivity (D), and external quantum efficiency (EQE), faster response times, etc. PDs with faster response time and high sensitivity are attractive, and the ultimate sensitivity of any PD is to detect a single photon.

2.1.1. Device Structures. According to the spatial layout of the photoactive material and the electrodes, PD architectures have been categorized into lateral (in-plane) and vertical (out-of-plane) configurations (Figure 8a−c). PDs with additional interfacial charge transport layers along with the electrodes in the vertical configuration are known as photovoltaic-type PDs or photodiodes. On the other hand, the PDs constructed from the active layer and electrodes are kenned as photoconductors; they have both the lateral and vertical configurations. Photodiodes having diminutive electrode spacing exhibit faster response times and low driving voltages since their photo-response is decided by the charge carrier transit time (τ_t) rather than the carrier lifetime (τ_l).[121,122] Moreover, the photodiodes can operate without any applied bias voltages, which provides an excellent opportunity to design self-powered PDs. However, these self-powered PDs produce low photo-currents (contribution of only photogenerated carriers) and low responsivities due to the lack of internal photoconductive gain. Moreover, the maximum EQEs of photodiodes are ≤100% under ideal conditions due to the lack of adscititious charge injection under reverse bias conditions.[121] Instead, the photoconductors can produce high photocurrents, i.e., the combination of photogenerated carriers and injected carriers under bias conditions, thus leading to high responsivity as well as EQEs greater than 100% owing to their internal photo-conductive gain.[121] The high gain is attributed to the recirculation of one type of charge carriers between the symmetrical electrode contacts before they recombine with the opposite charge carriers. However, the photoconductors exhibit relatively slow response times since they are decided by the τ_l and require high driving voltages due to their large electrode spacing.[121] This signifies that there is a trade-off between the responsivity and the response time of the PDs. Hence, it is crucial to balance both parameters to realize relatively high-performance PDs. It is worth mentioning that, in comparison to the vertical device architectures, the lateral devices are more comfortable and easier to design. By moderately truncating the electrode spacing in the lateral configuration, one can anticipate achieving high-performance PDs.

2.1.2. Figures of Merit of Photodetectors. The overall practical performance of a PD is evaluated through its key figures of merit, as listed below.

1. Responsivity (R): The ratio of photogenerated current to the input light power, which signifies how the PD responds to the incident light signal. The SI unit is A/W. It is calculated using the following equation:

$$R = (I_{light} - I_{dark})/P_{in}S = I_{photo}/P_{in}S$$

where I_{light} is the photocurrent, I_{dark} is the dark current, P_{in} (W/m^2) is the incident light intensity, and S (m^2) is the active area of the PD device.

2. Specific detectivity (D^*): The key parameter, which reflects the sensitivity of a PD or signifies the ability of a PD to detect low-light signals. The detectivity is

https://doi.org/10.1021/acsaem.1c03284
ACS Appl. Energy Mater. 2022, 5, 1342−1377

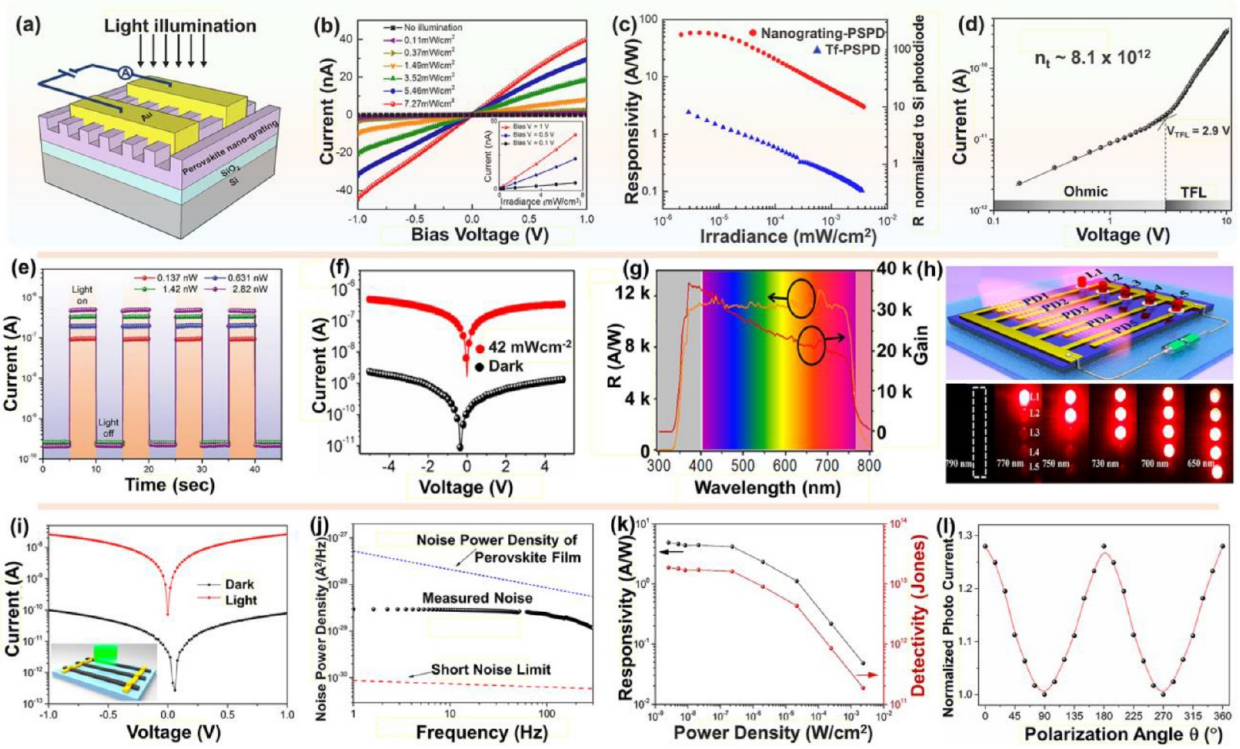

Figure 9. (a) Schematic representation of a nanograting perovskite PD. (b) Current−voltage characteristic curves of a nanograting PD with different light intensities from 0.11 to 7.27 mW/cm^2. The inset shows the current as a function of irradiance. (c) Responsivity curves of nanograting and thin-film-based perovskite PDs at an illumination of 635 nm with different light intensities. Adapted with permission from ref 130. Copyright 2016 American Chemical Society. (d) Current−voltage characteristics of single-crystalline 1D perovskite NW arrays. (e) Photoswitching characteristics of NWs array-based PD under different illumination powers. Adapted with permission from ref 132. Copyright 2017 Wiley-VCH. (f) Current−voltage curves of the PD under in the dark and under light illumination (550 nm, 42 μW cm^{-2}). (g) Responsivity and photoconductivity gain curves of the PD as a function of incident light wavelength. (h) Schematic representation of the monolithic integrated device for wavelength detection (top). Digital photograph of the integrated device under working conditions. LEDs embedded within the integrated device can serve as visual indicators for the incident light signals of different wavelengths (bottom). Adapted with permission from ref 39. Copyright 2017 American Chemical Society. (i) Dark and light current−voltage curves of the PD under 530 nm illumination with a light intensity of 2.36 mW cm^{-2}. The inset shows a schematic of the PD device structure. (j) Characteristic curves of noise current measurements at various frequencies. (k) Responsivity and detectivity curves of the PD with respect to different light intensities of the 530 nm light source at an applied bias of 1 V. (l) Polarization-dependent photocurrent characteristics of the PD as a function of the polarization angle θ. Adapted with permission from ref 131. Copyright 2016 American Chemical Society.

inversely proportional to the noise equivalent power (NEP) and can be written as follows:

$$D^* = \sqrt{S\Delta f}/\mathrm{NEP}$$

where Δf is the electrical bandwidth in Hz and S is the active area of the device. NEP is the lowest light intensity at which a PD can identify the noise:

$$\mathrm{NEP} = i_{sn}/R_\lambda$$

where i_{sn} is the shot noise current and R_λ is the responsivity at a specific wavelength. The total noise is the contribution of generation−recombination noise, shot noise, thermal noise, and $1/f$ noise. The overall noise of a PD is mainly caused by the shot noise; therefore, the shot noise current can be written as

$$i_{sn} = \sqrt{2qI_{dark}\Delta f}$$

where q is the charge of an electron. The detectivity equation can then be simplified as

$$D = R_\lambda/\sqrt{2qJ_d}$$

where $J_d = I_d/S$ is the dark current density, commonly expressed in Jones (cm·$\sqrt{Hz}$/W).

3. External quantum efficiency (EQE): The ratio of the total number of electrons/holes that are contributed to the output current to the total number of incident photons, expressed in %. The following equation calculates it:

$$\mathrm{EQE} = R_\lambda hc/q$$

where h is Planck's constant, c is the speed of light, and q is the charge of an electron.

4. Photosensitivity, or on/off ratio: The ratio of the photocurrent to the dark current; it reflects the sensitivity of a PD to the incident light signals:

$$\text{photosensitivity} = I_{light}/I_{dark}$$

5. Response time: The ability of a PD to respond quickly to the incident light signals in the time domain. In general, the response time is evaluated by the time taken by the PD to rise from 10% to 90% (rise time) and fall from 90% to 10% (fall time). An effective method to analyze

https://doi.org/10.1021/acsaem.1c03284
ACS Appl. Energy Mater. 2022, 5, 1342−1377

and evaluate the rise and fall time of a PD uses transient photocurrent measurements and use exponential equations to estimate the response time:

$$\text{Rise time equation:} \quad I = I_0 - I_0\, e^{-x/t_r}$$

$$\text{Fall time equation:} \quad I = I_0 + A_1\, e^{-x/t_f}$$

where I is the current, I_0 is the initial value of the current, A_1 is an independent variable, t_r is the rise time, t_f is the fall time, and x is the time. The response time is expressed in seconds.

6. Linear dynamic range (LDR): The responsive optical power range of a PD, where the measured photocurrent is in a linear relation with the power of the input light signal, calculated as follows:

$$\text{LDR} = 20 \log \frac{J_{max} - J_d}{J_{min} - J_d}$$

where J_{max} and J_{min} are the maximum and minimum current densities detectable by the PD and J_d is the dark current. Both J_{max} and J_{min} are photocurrents that a PD could distinguish from the dark current.

7. Photoconductive gain (G): The number of charge carriers flowing between the symmetrical electrodes before they recombine per an incident photon. It is also defined as the ratio of the charge carrier lifetime to the transit time of the charge carrier between the electrodes:

$$G = \frac{\tau_l}{\tau_t} = \frac{\tau_l}{d^2/\mu V}$$

where τ_l and τ_t are the charge carrier lifetime and transit time, d is the channel length of the PD, μ is the carrier mobility, and V is the bias voltage.

2.1.3. Nanowire-Based Photodetectors. The 1D perovskite NWs with highly crystalline nature, unique enclosing surfaces, specific crystallographic direction, reduced grain boundary, reduced recombination rates, and long charge-carrier lifetimes are suitable candidates for the realization of high-performance PDs.[39,115−122] In addition, their large surface-to-volume ratio enhances light absorption, scattering, and harvesting, which further improves the overall performance of the PDs. Recently, several reports have documented the successful fabrication of PDs from 1D NWs as photoactive material, where the PDs are designed from both single NWs as well as ensemble NWs.[57,62,73,79,85,123−141] In single NW-based PDs, only one isolated NW is used as a photoactive material/channel between the electrodes. On the other hand, in ensemble NW PDs, a bunch of NWs are arranged/oriented in either a parallel/uniform pattern or a random distribution in the space between the electrodes. Schematic representations of the NW-based PDs are shown in Figure 8d−f. In most of the cases, the self-assembled or randomly distributed NWs-based PDs showed poor device performance due to ineffective material utilization. Furthermore, randomly oriented adjacent individual NWs induce high contact resistance and increase the overall resistance of the device, which limits the overall photocurrent and response time of the PDs.[98,99,142] Also, NWs grown within the template pores were shown to reduce light absorption and limit the PD performance.[78,143] Hence, patterned or parallelly aligned (array) and single NWs are expected to generate high-performance PDs.

2.1.4. Aligned Perovskite NW-Array-Based Photodetectors. The first perovskite monolayer consists of densely aligned NWs achieved through a one-step self-assembly method followed by mask-assisted selective area treatment, which is utilized for the fabrication of PDs. The devices showed the responsivity of 1.32 A/W, detectivity of 2.5×10^{12} Jones, and response time of 0.3 ms.[129]

To precisely control the dimensions, position, and alignment of NWs, a nanoimprint lithography (NIL) technique has been utilized with Si nanograting molds (Figure 9a). The NIL-based NWs exhibited improved crystallinity and better photoconducting properties (Figure 9b). Therefore, the PDs displayed better performance, with a maximum responsivity of 24.1 A/W at 2 nW/cm^2 (466 nm) and 58.5 A/W at 4.5 nW/cm^2 (635 nm) (Figure 9c) at an applied bias of 1 V.[130] Likewise, the asymmetric wettability method has been used to precisely regulate the position, alignment, and fluid dynamics of liquids to achieve highly crystalline and crystallographically ordered 1D perovskite NWs.[132,134] The corresponding NWs are highly crystalline, having smooth surfaces with a lower trap density of 8.1×10^{12} cm^{-3} (Figure 9d) compared to the thin-film counterpart of 1.4×10^{16} cm^{-3}. Moreover, the $I-V$ curves have shown a definite transition from the ohmic region ($I \sim V$) to the trap-filling limit (TFL) region ($I \sim V^n$, $n > 3$) (Figure 9d). The $CsPbBr_3$ NWs-based PDs displayed responsivity of 1377 A/W, faster response time (rise time of 21.5 μs and fall time of 23.4 μs), and polarization-dependent photodetection,[132] whereas $CsPbI_3$ NWs-based PDs showed responsivity of 1294 A/W and detectivity of 2.6×10^{14} Jones.[134] Also, the PDs exhibited good photoswitching behavior under incident light with different powers (Figure 9e). Similarly, directional dewetting was employed to achieve 1D perovskite single-crystal NW arrays.[133] The bandgap of the 1D single crystals could be tuned from 1.7 to 3.1 eV by regulating the halide composition. The PDs designed from $MAPbBr_3$ 1D NWs exhibited enhanced responsivity of 3160 A/W, which was attributed to reduced recombination, low trap density, and long carrier lifetime.

As a matter of fact, PDs with a wide spectral response make it arduous to quantify the relative wavelength of the incoming light signals. Despite that, Deng et al. have reported an integrated device using the PDs for spectral detection.[39] Well-aligned single-crystalline perovskite NW arrays on SiO_2/Si substrate were achieved by a facile fluid-guided antisolvent vapor-assisted crystallization method.[39] The microscopic images revealed the formation of large-area continuous and uniform NW arrays with ultralong, crack-free, and smooth surfaces. The PDs designed from these arrays exhibited excellent photoconducting performance (Figure 9f) with responsivity of 12 500 A/W, photoconductive gain of over 35 000 (Figure 9g), and detectivity of 1.73×10^{11} Jones. Besides, the arrays have been used for the demonstration of integrated devices for the detection of various light signals in the wavelength range 680−780 nm. For this, the PDs were fabricated with numerous perovskite compositions ($MAPb(I_{1-x}Br_x)_3$; x = 0, 0.1, 0.2, 0.3, and 0.4) to relatively tune the light absorption and integrated with five LEDs (Figure 9h, top). The monolithic integration of PDs and LEDs systems resulted in a unique configuration and allowed sequential detection of the wavelength of the incident light signals (Figure 9h, bottom). These reports are based on microfluidics-based techniques that involve guiding the fluid flow and mass

https://doi.org/10.1021/acsaem.1c03284
ACS Appl. Energy Mater. 2022, 5, 1342−1377

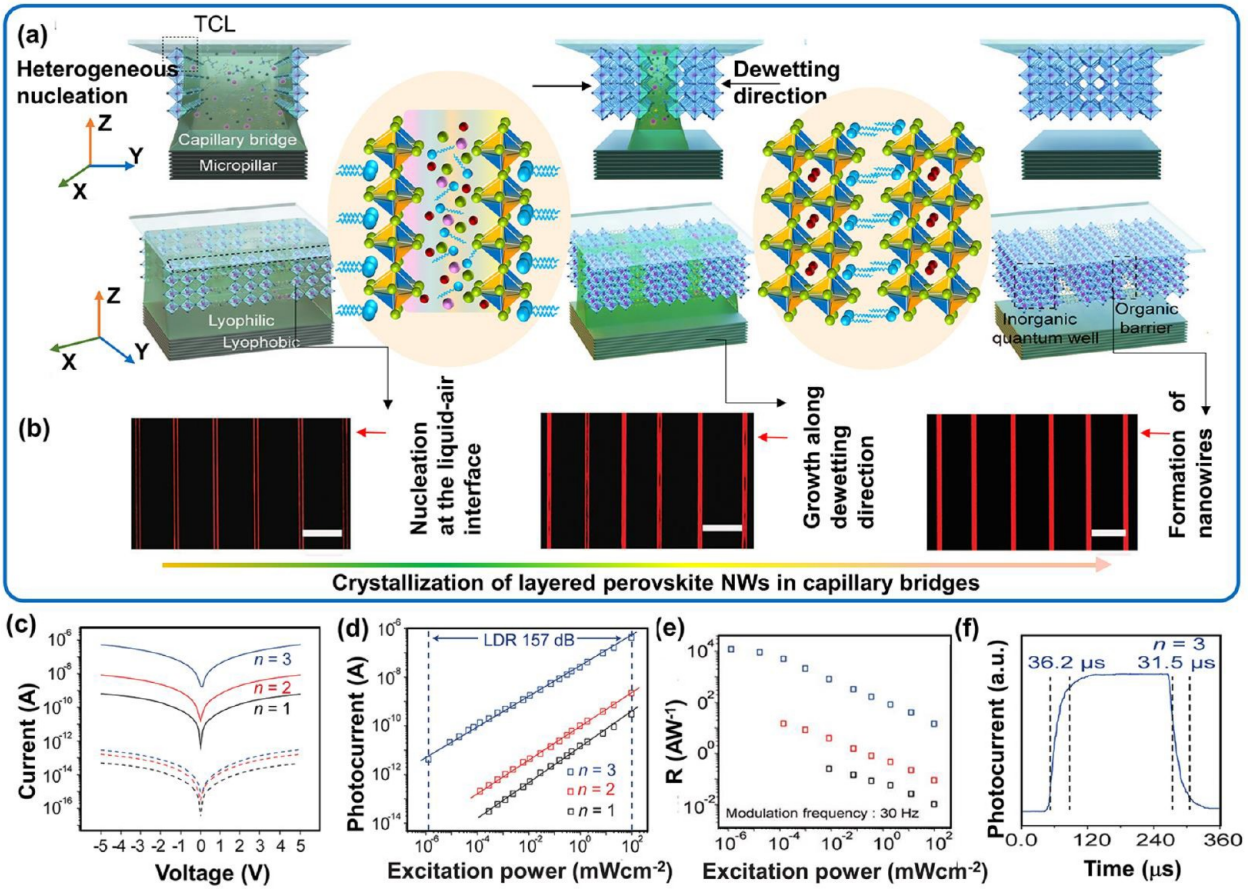

Figure 10. (a) Schematic illustration of the crystallization, growth, and formation of Q2DPe NWs in a capillary bridge rise approach. It also depicts the initial heterogeneous nucleation at the liquid−air interface, followed by growth of the perovskite crystal along the dewetting direction. (b) Observation of the initial nucleation (left), growth (middle), and formation (right) processes of the Q2DPe NWs by an in situ fluorescence microscopy imaging technique. (c) Steady-state logarithmic current−voltage curves of n = 1, 2, and 3 Q2DPe NW arrays in the dark and at an illumination power of 96.56 mW cm^{-2}. Solid and dashed lines are photocurrents and dark currents, respectively. (d) Photocurrent vs irradiance characteristic curves at an applied bias of 5 V. (e) Responsivity vs irradiance characteristic curves of the Q2DPe NWs array-based PDs of different layer numbers (n = 1, 2, 3) measured under a modulation frequency of 30 Hz. (f) Response times of Q2DPe NW arrays under a fixed illumination power of 96.56 mW cm^{-2}. Adapted with permission from ref 146. Copyright 2020 Wiley-VCH.

transport of perovskite precursors within the micro-/nanochannels to achieve the desired 1D NW structures.

To avoid the complex, multistep template-guided and sophisticated lithography methodologies, a CASP strategy has been applied to obtain aligned and highly crystalline perovskite NW arrays (Figure 5c−e).[74] Optical microscopic and SEM images showed the formation of nanochannels (Figure 5f−h). Here, the NWs' deposition occurs through the integration of a capillary-directed assembly by periodic nanochannels and solution-printing with the programmable moving substrate. The produced perovskite NW arrays have attained highly crystalline, uniform, crack-free, and smooth surfaces. The corresponding PDs fabricated from the solution-printed perovskite NWs array exhibited an ultralow dark current of 2.20 × 10^{-10} A owing to the NWs' low intrinsic carrier concentration. The PDs showed 3 orders of photocurrent under 442 nm laser at an incident light intensity of 27.03 mW cm^{-2}, maximum responsivity of 5.49 A W^{-1}, rise time and fall time of 40 and 95 ms, respectively.[74]

It should be noted that the presence of a large surface area of NWs leads to the expeditious degradation of PDs when exposed to moisture or ambient conditions. Thus, the perovskite NWs were soaked with oleic acid to passivate the surface.[131] The oleic acid-treated NWs exhibited good photoconductive behavior (Figure 9i) and possessed very low noise current (Figure 9j). Hence, the PDs designed from these NWs exhibited high detectivity of 2 × 10^{13} Jones (Figure 9k), which was attributed to the passivation of NW surface defect states through the oleic acid treatment. Moreover, it was revealed that the oleic acid passivation of NWs resulted in enhanced stability, reduced trap density, increased carrier lifetime, and increased carrier mobility.[131] Withal, the oleic acid-treated NWs exhibited a strong polarization-dependent photodetection due to its anisotropic 1D geometry (Figure 9l).

Recently, layered quasi-two-dimensional perovskites (Q2DPe) have received considerable interest in various optoelectronic device applications due to their impressive photophysical properties.[115,141,144,145] They have a conspicuous feature to tune optical and electronic properties by playing with the number of inorganic framework layers via incorporation of structurally diverse functional organic cations. The Q2DPe structure comprises consecutive inorganic octahedra framework layers and organic layers that bestow quantum-well and barrier electronic band structures, respectively. The anisotropic design of the Q2DPe integrates both the inorganic conductive channel and the resistive hopping

https://doi.org/10.1021/acsaem.1c03284
ACS Appl. Energy Mater. 2022, 5, 1342−1377

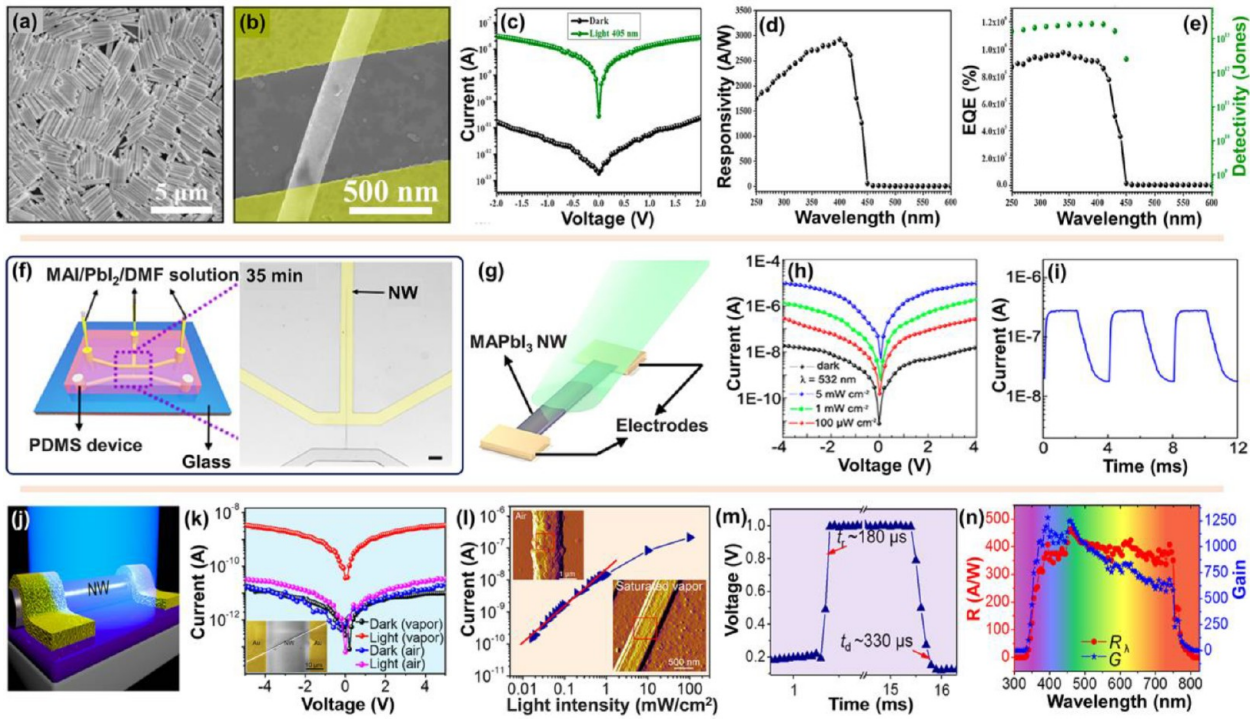

Figure 11. (a) SEM image of $CsPbI_3$ nanorods. (b) SEM image of a single NR-based PD device with metal electrodes. (c) Logarithmic current−voltage curve for the PDs in the dark and under irradiation with 405 nm light with 10.69 mW cm^{-2} intensity. (d, e) Responsivity, detectivity, and EQE curves of the PDs with various wavelengths ranging from 250 to 600 nm at a bias voltage of 2.0 V. Adapted with permission from ref 126. Copyright 2018 American Chemical Society. (f) Micro-/nanofluidic platform depicting the nanochannel for the growth of NW (right). The upper microchannel was filled with a precursor solution, while the lower was empty. The growth of a $MAPbI_3$·DMF NW appeared at a real time of 35 min (left). (g) Schematic of the PD based on a single $MAPbI_3$ NW. (h) Dark and light current−voltage curves of the $MAPbI_3$ NW under different light intensities of the 532 nm laser. (i) Temporal response curve of the PD with an illumination intensity of 100 μW cm^{-2} (532 nm) and a modulation frequency of 250 Hz under a bias of −4 V. Adapted with permission from ref 73. Copyright 2018 American Chemical Society. (j) Schematic of the individual $MAPbI_3$ NW-based PD. (k) Dark and photocurrent curves of the PD based on the $MAPbI_3$ NW synthesized under saturated vapor and in the air, respectively, with a light intensity of 60 μW cm^{-2}. The inset shows the SEM image of the PD. (l) Photocurrent versus incident light intensity curve of the PD. The inset shows the AFM images of the NWs grown in saturated vapor (bottom) and the air (top). (m) Single temporal response curve of the PD with rise and fall times. (n) Responsivity and photoconductive gain curves of the PD as a function of various incident light wavelengths. Adapted with permission from ref 57. Copyright 2018 American Chemical Society.

barrier. Recent studies on the Q2DPe revealed the existence of exotic edge states which enable the rapid dissociation of bound excitons into long-lived free charge carriers. Therefore, to reap the advantages of these edge states, the Q2DPe-based single-crystalline NWs ($(BA)_2(MA)_{n-1}Pb_nI_{3n+1}$; n represents number of layers) having a pure (101) crystallographic orientation are prepared through a capillary bridge rise approach on an asymmetric-wettability topographical template.[115] Along the NW length, it contains the alternative layer-by-layer insulating organic cation and conductive inorganic octahedra, respectively. Therefore, the charge carriers experience a high resistance path within the interior of the crystal structure and a high conducting path at the edges of the crystal.[115] The PDs designed from these Q2DPe-based NWs displayed enhanced photocurrent, low noise current, maximum responsivity of 15 000 A W^{-1}, and detectivity of 7×10^{15} Jones, which are attributed to the combination of efficient free-carries edge conduction and high resistive hopping barriers. Besides, the PDs exhibited a rise time of 27.6 μs and a fall time of 24.5 μs. The presence of different numbers of layers in Q2DPe NWs influences the PD's performance. In this Q2DPe NWs geometry: (i) along the NW length, the presence of alternative serial hopping barriers efficaciously suppresses the dark current that contributes to the high detectivity, (ii) bound excitons diffuse to the edge states where they dissociate into long-lived free carriers, which contributes to the high photocurrent and responsivity, and (iii) the NW arrays efficiently amplify the overall photoresponse.[115]

Similarly, Q2DPe single-crystalline NWs ($(ThMA)_2(MA)_{n-1}Pb_nI_{3n+1}$, where ThMA = 2-thiophenemethylamine) were obtained through the combination of capillary bridge lithography and solvent engineering approaches (Figure 10a).[146] A hybrid solvent, i.e., the mixture of DMF:DMSO = 4:1 v/v, produces the (101)-oriented single-crystalline NW arrays, whereas pure DMF or a high content of DMSO in hybrid solvent produces NWs with low crystallinity or random orientation.[146] The in situ fluorescent microscopy images revealed a clear step-by-step nucleation process at two sides of the capillary bridges (liquid−air interface), followed by continuous growth of the perovskite NWs along the dewetting direction (Figure 10b). The PDs designed from the Q2DPe NWs exhibited enhanced photocurrents (Figure 10c,d), responsivity of 11 000 A/W (Figure 10e), detectivity of 9.1×10^{15} Jones, rise time of 36.2 μs, and fall time of 31.5 μs (Figure 10f).[146] These reports have demonstrated the formation of highly crystalline Q2DPe-based 1D NWs with highly oriented/aligned arrays for the realization of high-performance photodetection, and they are believed to be highly suitable for integrated optoelectronic device applications.

https://doi.org/10.1021/acsaem.1c03284
ACS Appl. Energy Mater. 2022, 5, 1342−1377

Table 1. Figures of Merit of the Perovskite NWs-Based PDs

type of orientation	NW composition	responsivity (A/W)	detectivity (Jones)	EQE (%)	rise time	decay time	ref
NWs array	$MAPbI_3$	4.95	2×10^{13}	–	<0.1 ms	<0.1 ms	131
single NW	$MAPbI_3$	460	2.6×10^{13}	–	180 μs	330 μs	57
NWs array	$MAPbI_3$	12 500	1.73×10^{11}	–	0.34 μs	0.42 μs	39
single NW	$MAPbI_3$	4.1	6.1×10^{11}	730	–	–	117
single NW	$MAPbI_3$	410	9.1×10^{12}	–	0.22 ms	0.79 ms	73
single NW	$Cs_{0.5}(CH_3NH_3)_{0.5}PbI_3$	23	2.5×10^{11}	5.4×10^3	–	–	124
single NW	$CsPbI_3$	2.92×10^3	5.17×10^{13}	0.9×10^6	0.05 ms	0.15 ms	126
single NW	Om-$CH_3NH_3PbI_3$	11.36	1.48×10^{12}	–	84 ms	85 ms	128
NWs array	α-$CsPbI_3$	1294	2.6×10^{14}	–	0.85 ms	0.78 ms	134
aligned NWs	$MAPbI_3$	1.32	2.5×10^{12}	–	0.2 ms	0.3 ms	129
NWs array	$MAPbBr_3$	20	4.1×10^{11}	–	1.6 ms	6.4 ms	135
NWs array	$MAPbI_3$	789	10^{14}	$\sim 10^5$	432 μs	556 μs	141
NWs array	$CsPbBr_3$	5.49	–	–	95 ms	40 ms	74
NWs array	$(BA)_2(MA)_3Pb_4I_{13}$	1.5×10^4	7×10^{15}	–	27.6 μs	24.5 μs	115
NWs array	$(ThMA)_2(MA)_2Pb_3I_{10}$	1.1×10^4	9.1×10^{15}	–	36.2 μs	31.5 μs	146
single NW	$CsPbI_3$	4489	7.9×10^{12}	–	<50 ms	–	91
	$CsPbBr_3$	3306	6.0×10^{12}				
	$CsPbCl_3$	1183	6.6×10^{12}				
single NW	$CsPbBr_3$	4400	–	–	252 μs	300 μs	85

2.1.5. Single Perovskite NW-Based Photodetectors. Apart from the ensemble of NWs array, PDs were also fabricated from single, isolated, or free-standing NWs.[91] Single NWs provide ample opportunities to design miniaturized devices and can be integrated into compact nanophotonic/optoelectronic devices. Furthermore, minimizing the active device area and reducing the resistor−capacitance (RC) constant can also pave the way to design fast responsive PDs. PDs based on a single or isolated NW can be constructed from the dispersion of NWs from solution or dry transfer methods or by directly growing the NW on the target substrate, followed by the deposition of metal electrodes on the two ends of the NW, typically using electron beam lithography.

Single-crystalline all-inorganic $CsPbI_3$ perovskite NWs were prepared from a catalyst-based VLS growth mechanism,[91] as explained in section 1. The single NW-based $CsPbI_3$ PDs have exhibited high-performance photodetection with the responsivity of 4489 A/W, detectivity of 7.9×10^{12} Jones, and gain of 1564. Also, PDs from $CsPbBr_3$ were demonstrated with responsivity of 3306, detectivity of 6.0×10^{12} Jones, and gain of 1530, and from $CsPbCl_3$ with a responsivity of 1183, detectivity of 6.6×10^{12} Jones, and gain of 792.[91] Importantly, all the three NW-based PDs produced low dark currents of 0.1−1 pA under an applied bias of 5 V, which is probably owing to their minimized free carrier concentration in high-quality growth of NWs through the VLS method. Similarly, all-inorganic $CsPbI_3$ NRs of uniform distribution with an average diameter of 150 nm and length of 2 μm (Figure 11a) have been synthesized by a hot-injection method.[126] These single NR-based PDs (Figure 11b) have shown good photocurrent behavior and low dark current (Figure 11c) and screened maximum responsivity of 2920 A/W (Figure 11d), EQE of 0.9×10^6%, detectivity of 5.17×10^{13} Jones (Figure 11e), and rise time of 50 μs. Moreover, the PDs showed a stable photoresponse even after aging of the devices in ambient conditions for 1 week.[126] The ultralong NWs with a diameter of several hundreds of nanometers and length of several millimeters were achieved through graphoepitaxial effect assisted vapor growth on annealed M-plane sapphire substrates,[85] as discussed in section 1. PDs built from these individual ultralong NWs exhibited responsivity of 4400 A/W, rise time of 252 μs, and fall time of 300 μs at an applied bias of 1 V. The PDs also exhibited excellent photoswitching behavior at low operating voltages.[85] Similar ultralong NWs with smooth surfaces have been achieved by the modified ligand-assisted reprecipitation (LARP) technique. Herein, the NWs were synthesized using OAm as an inhibitor which passivates the surface of $MAPbI_3$ NWs and thereafter slows down the crystallization rate, which promotes the growth of high-quality NWs to several millimeters long.[128] The single OAm-NW-based PDs showed the enhanced responsivity of 11.36 A/W and detectivity of 1.48×10^{12} Jones compared to those without OAm. The enhanced performance is attributed to the formation of high-quality NWs with reduced defects along the surface that helps to improve the light absorption and reduce the recombination centers.[128] Most of the perovskite NWs have been prepared from organic solvents such as DMF and DMSO. In contrast, Dong et al. have reported the synthesis of $Cs_x(MA)_{1-x}PbI_3$ perovskite NWs from aqueous solution.[124] The corresponding single NW-based PDs showed the responsivity of 23 A/W and detectivity of 2.5×10^{11} Jones. Further, to selectively grow the single-crystalline perovskite NWs with a controlled number, location, and orientation, a micro-/nanofluidic fabrication technique was utilized (Figure 11f).[73] These single NW-based PDs (Figure 11g) exhibited incident power-dependent photoconduction behavior (Figure 11h) and displayed a responsivity of 410 A/W and detectivity of 9.1×10^{12} Jones with good switching behavior (Figure 11i). Moreover, PDs with excellent mechanical flexibility on polyethylene terephthalate substrates under various bending conditions were demonstrated, and the devices revealed stable behavior under bending conditions.[73]

It is worth mentioning that the preparation of perovskite NWs in ambient conditions resulted in a large number of grain boundaries/surface defects due to their vulnerability to moisture.[57] To overcome it, the perovskite NWs were directly grown on a SiO_2/Si substrate in an isolated organic solvent vapor (DCM) atmosphere, i.e., a saturated vapor-assisted crystallization (SVAC) process. The resultant single-crystalline NWs exhibited relatively enhanced stability with smooth

https://doi.org/10.1021/acsaem.1c03284
ACS Appl. Energy Mater. 2022, 5, 1342−1377

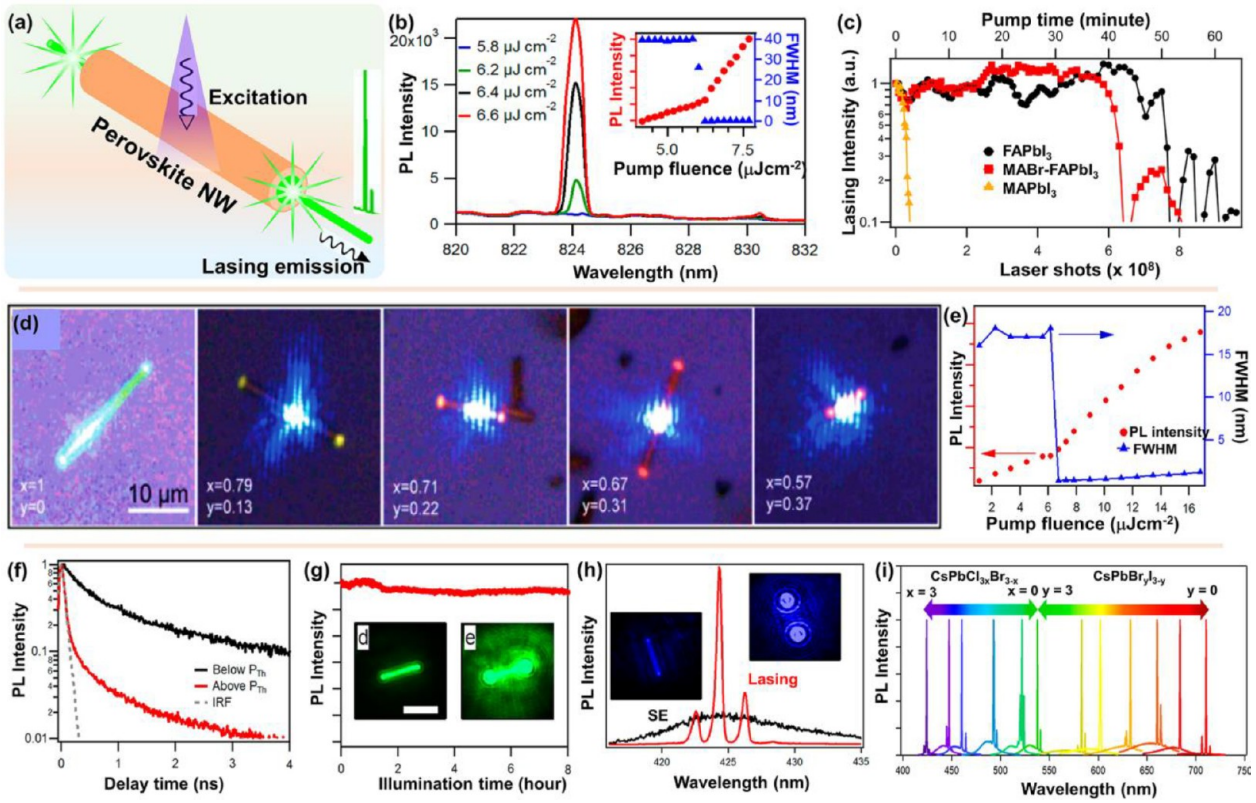

Figure 12. (a) Schematic illustration of the lasing action from a NW under excitation. (b) NW laser emission spectra as a function of the pump fluence or lasing threshold. The inset shows the emission intensity and fwhm of emission peak as a function of P, revealing the lasing threshold of ~6.2 μJ cm^{-2}. (c) Lasing emission intensity of $FAPbI_3$, MABr-stabilized $FAPbI_3$, and $MAPbI_3$ NWs as a function of pump time with a continuous illumination at room temperature (402 nm pulsed laser, 150 fs, and 250 kHz). (d) Optical microscopy images of the lasing action of NWs with various compositions ($(FA_xMA_{1-x})Pb(Br_{3-y}I_y)$). Adapted with permission from ref 151. Copyright 2016 American Chemical Society. (e) Lasing emission intensity and fwhm of emission spectra of $CsPbBr_3$ NWs as a function of pump fluence. (f) Time-resolved PL decay curves of the $CsPbBr_3$ NW above and below the P_{th} along with the instrument response function (gray dashed line). (g) Emission intensity of a $CsPbBr_3$ NW laser as a function of time with up to 8 h of continuous illumination under the excitation of a 402 nm pulsed laser (150 fs and 250 kHz) at room temperature. The inset shows the corresponding fluorescence images of the NW below and above P_{th}; scale bar, 10 μm. (h) Emission spectra of a $CsPbCl_3$ NW below and above the P_{th}. The inset shows the corresponding fluorescence images). (i) Composition-dependent tunable lasing from single-crystal NWs of $CsPbX_3$. Adapted with permission from ref 152. Copyright 2016 American Chemical Society.

surfaces and reduced grain boundaries due to the elimination of moisture intrusion during the growth conditions (inset of Figure 11l). These individual NWs-based PDs were constructed by selectively picking the NWs by a probe in the probe station and placing them on the SiO_2/Si substrate, followed by the deposition of metal contacts (Figure 11j and inset of Figure 11k). The PDs based on the NWs grown in DCM vapor conditions exhibited significantly higher photocurrent and lower dark current than the NWs grown in open-air conditions.[57] Furthermore, the PDs showed a linear dependence on incident light intensity and measured photocurrent (Figure 11l). The PDs displayed the responsivity of 460 A/W, detectivity of 2.6 × 10^{13} Jones, gain of 1279, rise time of 180 μs, and fall time of 330 μs (Figure 11m,n). Besides, the KPFM surface potential measurements on SVAC-NWs under light conditions revealed that, among the photogenerated charge carriers (electrons and holes), holes get transported to the PEDOT:PSS layer, whereas the electrons will be left in the NW, and the accumulation of free electrons in the NWs leads to the enhanced photocurrent.[57] Contrarily, in open-air-synthesized NWs, due to the presence of grain boundaries, the photogenerated electrons tend to recombine at the grain boundaries and lead to low photocurrent. Also, the PDs have shown long-term device stability; the photoresponse decreased very slightly after 45 days of storage. Notably, the PDs fabricated from the air-synthesized NWs experienced continuous degradation and were fully degraded by the ninth day.[57] These results revealed that the perovskite NWs grown in SVAC exhibit better stability and can be used for the realization of high-performance optoelectronic device applications. Overall, the aligned/single perovskite NWs-based PDs showed better photodetection performance than the thin-film and randomly oriented NWs-based PDs. However, developing new strategies to obtain stable all-inorganic perovskite NWs with reduced surface defects/grain boundaries is crucial for high-performance practical device applications. We have tabulated some PDs figures of merit in Table 1.

2.2. Perovskite NWs Lasers. NW-based lasers gained a lot of research attention after the demonstration of ultraviolet lasing from ZnO NWs in 2001.[147] NW lasers are believed to be potential building blocks for miniaturized nanoscale photonic and optoelectronic devices due to their reduced dimension, highly localized coherent output, and efficient waveguiding.[148] The added advantages with NW-based lasers are self-waveguiding along the axial direction and two end facets acting as a reflecting mirror arrangement for optical amplification. To quantify, lasers were characterized by the lasing threshold (P_{th}) that describes the critical oscillation

https://doi.org/10.1021/acsaem.1c03284
ACS Appl. Energy Mater. 2022, 5, 1342−1377

condition and the quality factor which describes the photon lifetime. Herein, a lower P_{th} fosters easy oscillations, and a high quality factor provides the efficient amplification that leads to high emission intensity.

For the first time, biexciton lasing was observed in the layered perovskite $(C_6H_{13}NH_3)_2PbI_3$ by Kondo et al. in 1998.[149] In the past couple of years, halide perovskite materials have received enormous interest in lasing applications. Compared to their 3D bulk halide perovskite counterparts, the long carrier lifetimes and low nonradiative recombination rates of perovskite NWs make them prominent candidates for lasing applications.[40,56,148,150−153] A schematic representation of the lasing action is displayed in Figure 12a. First, the lasing action from single-crystalline perovskite NWs was demonstrated by Zhu et al. in 2015, where the NWs were synthesized by the solution-dipping method.[40] The wavelength-tunable lasing phenomenon was achieved from the single-crystal lead halide perovskite NWs of $MAPbBr_3$, $MAPbI_3$, and $MAPb(Cl/Br)_3$. The NWs exhibited smooth and flat rectangular facets, which are ideal Fabry−Perot cavities for the efficient lasing phenomenon. These NWs-based lasers exhibited very low P_{th} of 220 nJ cm^{-2}, high quality factor of 3600, and lasing quantum yield (QY) approaching near unity, with emission peaked at 777 nm at RT using a 402 nm laser source for optical pumping. The lasing operation was further corroborated from the emission image of the NW below and above P_{th}. Uniform intensity across the whole NW's length below the P_{th} reveals the photoluminescence (PL), whereas strong emission at the two ends of the NW above the P_{th} confirmed the effective lasing action from the NWs.[40] Moreover, tunable lasing from the infrared and green regions was observed through the mixed-halide composition through the halide exchange during the growth of the NWs.[40] Similarly, $FAPbX_3$-based NW lasers were demonstrated by replacing MA organic cation with FA cation and their mixture (FA/MA).[151] In comparison with $MAPbX_3$ NWs, the $FAPbX_3$ NWs exhibited red-shifted emission and better thermal stability, with a low P_{th} of 6.2 μJ cm^{-2} and quality factors of 1500−2300 (Figure 12b). Importantly, it is found that the $FAPbX_3$ NWs-based lasers exhibited more stable behavior than the $MAPbX_3$ NWs at RT (Figure 12c). Lasing action in the broad wavelength region was achieved by rationally tuning the halides and organic cations composition ($(FA,MA)PbI_3$ and $(FA,MA)Pb(I,Br)_3$) (Figure 12d).[151] Similarly, lasing action was also achieved from the perovskite NWs synthesized by solution methods followed by gas-phase halide exchange, which exhibited Fabry−Perot lasing at ∼550 and 785 nm from $MAPbBr_3$ and $MAPbI_3$ NWs with a P_{th} of 9.8 and 9.2 mJ cm^{-2}, respectively, with a maximum quality factor of 1260.[56]

Recently, all-inorganic perovskite NWs have also captivated the research focus owing to their excellent stability in comparison to the hybrid organic−inorganic perovskites. Eaton et al. first reported the lasing action in all-inorganic perovskite NWs,[150] where the NWs were grown by dipping a PbI_2 thin film into a CsX−methanol solution with mild heating at 50 °C. Interestingly, these were the first surfactant-free $CsPbX_3$ NWs synthesized through a simple, low-temperature, and solution-phase process possessing excellent stability in ambient conditions. The NWs were single crystalline with well-defined facets, acting as high-quality Fabry−Perot laser cavities and contributing to the efficient lasing output. Under the excitation of a 400 ± 3 nm fs pulsed laser, the lasing action has occurred in $CsPbBr_3$ NWs with a P_{th} of 5 μJ cm^{-2} and quality factor of 1009 ± 5.[150] The NWs exhibited stable lasing action under both constant as well as pulsing excitation, which was maintained over 1 h (equivalent to 10^9 excitation cycles), and the lasing continued under ambient conditions. Besides the green lasing from $CsPbBr_3$ NWs, as-synthesized $CsPbCl_3$ NWs displayed blue lasing with a P_{th} of 86 μJ cm^{-2} and a maximum quality factor of 690 ± 70, with emission peaking at 430 nm.[150]

To extend and improve the lasing action toward the blue emissive region as well as achieve stable lasing from perovskite NWs, Fu et al. continued their efforts and have achieved broad-wavelength-tunable lasing from the near-infrared to the blue region in single-crystalline $CsPbX_3$ NWs by varying their composition.[152] Lasing action in the entire visible spectral region of 420−710 nm was demonstrated at RT from the NWs with low P_{th} and high quality factors. Single-crystalline pure halide $CsPbX_3$ NWs were synthesized by a simple solution-dipping method where a piece of lead-precursor-coated substrate was immersed in CsX−anhydrous methanol solution at 22 °C. These NWs also showed smooth surfaces and facets, which were ideal Fabry−Pérot cavities for designing the high-performance NW lasers. The lasing action was performed by optically pumping the NWs with 402 nm, 250 kHz laser pulse excitation under a N_2 atmosphere.[152] Figure 12e shows the variation of PL intensity and full-width half-maximum (fwhm) of the PL peak under different pump fluences. Below the P_{th} of ∼6.2 μJ cm^{-2}, $CsPbBr_3$ NWs displayed broad PL spectra peaked at ∼530 nm with a fwhm of ∼17 nm, and the integrated PL intensity increased slowly with pump fluence (Figure 12e). Above P_{th}, a few sharp lasing peaks emerged, and the intensity was increased quickly with pump fluence, indicating the occurrence of lasing action. The log−log plot of PL intensity with different pump fluences showed the expected S-curve pattern, screening the evolution from the spontaneous emission to the amplified spontaneous emission transition regime to laser oscillation.[152] Further, time-resolved PL decay kinetics above and below P_{th}, as shown in Figure 12f, provided strong evidence of lasing action. PL lifetimes of ∼850 and <20 ps were observed for $CsPbBr_3$ NWs below and above P_{th}, which can be easily assigned to spontaneous and stimulated lasing emission, respectively.[152] Such spontaneous and stimulated lasing emission was further strengthened by fluorescence images of $CsPbBr_3$ NWs below and above P_{th}. Below the P_{th}, uniform intensity of spontaneous emission was recorded, and above the P_{th}, maximum intensity is observed at the end faces of the NWs, along with the diffraction pattern owing to the diffraction of emitted laser light through the NW (inset of Figure 12g). Notably, the NWs exhibited stable lasing emission with no significant degradation after at least 8 h, or the equivalent of 7.2×10^9 laser shots under continuous illumination of a femtosecond pulsed laser (Figure 12g). Furthermore, blue-emitting lasing action from $CsPbCl_3$ NWs was also tested and found to be similar to that of the $CsPbBr_3$ NWs (Figure 12h). $CsPbCl_3$ NWs-based blue lasers exhibited a P_{th} of 6 μJ cm^{-2} and a quality factor of 1300, with emission peaked at 424 nm at RT.[152] Then, $CsPbCl_xBr_{3-x}$ and $CsPbBr_yI_{3-y}$ alloy NWs were synthesized with controlled stoichiometry to tune the lasing wavelength. Figure 12i shows the broad wavelength tuning action from violet to red color by $CsPb(Cl/Br/I)_3$ NWs. The superior photophysical properties of pure inorganic $CsPbCl_3$ NWs compared to the organic−inorganic $MAPbCl_3$ or $FAPbCl_3$ NWs and wide bandgap $CsPb(Br,Cl)_3$ NWs make it possible to tune the lasing action at RT over a wide range of wavelengths with better stability.[152]

https://doi.org/10.1021/acsaem.1c03284
ACS Appl. Energy Mater. 2022, 5, 1342−1377

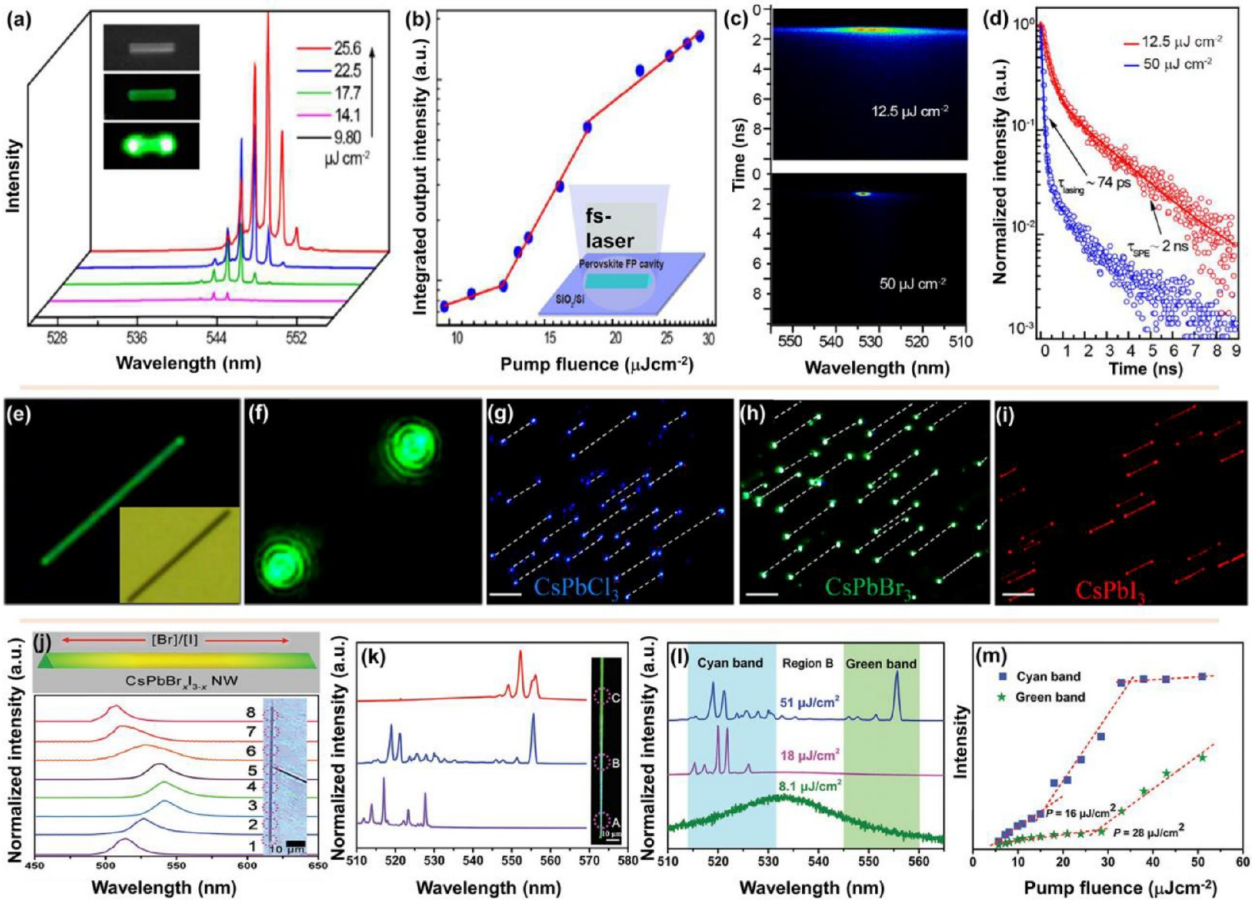

Figure 13. (a) Emission spectra of $CsPbBr_3$ triangular nanorods as a function of P_{th}. The inset shows the optical image (top) and fluorescence images of a single triangular NR below (middle) and above (bottom) the P_{th}. (b) Nonlinear response curve of laser output power as a function of pump fluence. (c) Streak-camera images of a single triangular rod below ($P \approx 12.5\ \mu J\ cm^{-2}$, top) and above ($P \approx 50\ \mu J\ cm^{-2}$, bottom) the P_{th}. (d) Corresponding time-resolved PL decay curves. Adapted with permission from ref 83. Copyright 2017 American Chemical Society. (e, f) Fluorescence images of the $CsPbBr_3$ NW below and above the P_{th}, respectively. The inset shows the optical microscopy image of a single $CsPbBr_3$ NW. (g–i) Fluorescence images of the in-plane directional $CsPbCl_3$, $CsPbBr_3$, and $CsPbI_3$ NW arrays above their P_{th}; scale bar, 10 μm. Dashed lines depict the position of the wires. Adapted with permission from ref 86. Copyright 2018 American Chemical Society. (j) Schematic of composition-graded $CsPbBr_xI_{3-x}$ NW (top) and normalized μ-PL spectra recorded at various positions (denoted with circles) of the NW (bottom). (k) μ-PL spectra collected from different positions (A, 521 nm; B, 521 and 556 nm; and C, 556 nm) of the NW above the P_{th}. (l) Pumping-fluence-dependent PL spectra of position B. (m) Integrated emission intensity of the lasing peak at 521 nm (cyan band) and 556 nm (green band) of region B as a function of pumping fluence. Adapted with permission from ref 153. Copyright 2018 Wiley-VCH.

In addition to the solution-phase methods, perovskite NWs designed from the vapor phase were also utilized for the demonstration of the lasing applications.[83,86] All-inorganic $CsPbX_3$ NWs with smooth surfaces and well-defined triangular facets were directly grown on SiO_2/Si substrates via a vapor-phase method. They exhibited room-temperature tunable lasing with low P_{th} and high quality factors. For instance, when the excitation fluence was smaller than 14.1 $\mu J\ cm^{-2}$, a spontaneous emission spectrum was observed with a peak position at 538 nm. A set of sharp peaks confirmed the lasing action above the excitation fluence of 14.1 $\mu J\ cm^{-2}$ (Figure 13a). The inset of Figure 13a shows the corresponding bright-field optical microscopy image (top) and emission images at low (middle) and high (bottom) excitation fluence of $CsPbBr_3$ triangular NWs. The output intensities from the NWs under different pump fluence are displayed in Figure 13b. Lasing action from these NWs was further confirmed from the time-resolved photoluminescence (TRPL) measurements. The detection of the PL (spontaneous emission with broad emission band and longer decay time) and lasing (stimulated emission with narrow emission band and ultrashort decay time) from the one end of the triangular NW was recorded when the excitation fluence was below (12.5 $\mu J\ cm^{-2}$) and above (50 $\mu J\ cm^{-2}$) the P_{th}, respectively (Figure 13c,d).[83]

Similarly, all-inorganic $CsPbX_3$ NWs were directly grown on annealed M-sapphire substrates using the graphoepitaxial effect via the vapor-phase growth method.[86] The lasing behavior of $CsPbX_3$ NWs was examined directly on the substrate itself at RT. The inset of Figure 13e shows the optical image of a representative single $CsPbBr_3$ NW. To examine the lasing action, the $CsPbBr_3$ NW was pumped with different pumping fluences. Spontaneous emission was observed from the whole NW at a low pumping fluence of below 4 $\mu J\ cm^{-2}$ (Figure 13e). When the excitation fluence increased to the P_{th} of 4.1 $\mu J\ cm^{-2}$ and above, strong lasing emission appeared with spatially coherent interference patterns from the two ends of the NW (Figure 13f). Therefore, at high pump intensity, the bright emission was localized at the end faces of the NW, and no light emission was observed from other parts of the NW due to the high degree of coupling of the spontaneous emission to the

https://doi.org/10.1021/acsaem.1c03284
ACS Appl. Energy Mater. 2022, 5, 1342–1377

cavity oscillation modes.[86] This study reveals the high crystalline quality and nearly perfect end facets of the as-grown $CsPbBr_3$ NW. Moreover, blue and red lasing action was also achieved from $CsPbCl_3$ and $CsPbI_3$ NWs, respectively, and Figure 13g–i displays the lasing action from the array of NWs. $CsPbX_3$ NWs were excited with a femtosecond pulse laser of 400 nm for $CsPbCl_3$ and 470 nm for $CsPbBr_3$ and $CsPbI_3$ NWs, above their P_{th} values. Bright light emission (blue, green, and red) from the two ends of all these directional $CsPbX_3$ NWs confirmed the realization of high-quality in-plane-aligned $CsPbX_3$ NW lasing action (Figure 13g–i). In addition, the quality factor values were found to be 2675, 1931, and 2256 for $CsPbBr_3$, $CsPbCl_3$, and $CsPbI_3$, respectively.[86] A similar kind of lasing behavior was achieved in various perovskite NWs. All the NWs discussed here so far have produced the single-wavelength lasing action under pump fluence or excitation.

To achieve dual-color lasing from a single NW, a composition gradient of $CsPbBr_xI_{3-x}$ NW (Figure 13j, top) with triangular facets and smooth surfaces was obtained through vapor-phase epitaxial growth on mica.[153] The graded composition with an increasing Br/I ratio from the center to the ends of the NW was achieved by desynchronized deposition of cesium lead halides along with temperature-controlled anion-exchange reaction. The graded composition resulted in different bandgaps along the NW's length, which induces a blue-shifted emission from the center to the ends owing to the excess Br at the NW's ends (Figure 13j, bottom). As a result, above the P_{th} the NW exhibited position-dependent lasing action across its length, with green and yellow colors at the ends and center, respectively.[153] Position-dependent emission properties across the NW's length screened a significant PL shift from 550 nm (2.25 eV) to 510 nm (2.43 eV) from the center to the ends, which revealed the existence of a composition difference within the single NW segment (Figure 13k). Lasing behavior from the composition-graded $CsPbBr_xI_{3-x}$ NW was studied by exciting the NW with a pulsed laser beam of 400 nm, with a focused spot of 100 μm in diameter (inset of Figure 13k). Above the P_{th}, multimode lasing was achieved at 521 and 556 nm at regions A and C (Figure 13k), respectively, owing to the composition gradient. From region B, both 521 and 556 nm lasing action was detected owing to the intermediate composition compared to that of the ends (Figure 13k). The pumping-fluence-dependent PL spectra revealed different P_{th} for cyan and green lasing, 16 and 28 $\mu J\ cm^{-2}$, respectively, similar for the individual regions A and C (Figure 13l,m).[153]

Finally, the exact underlying mechanism behind the lasing action from the perovskite NWs was understood through probing the $CsPbBr_3$ NWs with picosecond time resolution, which revealed that the lasing originates from the stimulated emission of an electron–hole plasma.[88] Anomalous blue-shifting of the lasing gain profile with time up to 25 ps was assigned as a signature for lasing involving plasmon emission.

Apart from the conventional photonic lasing applications, plasmonic and polariton lasing also garnered importance for the development of deep-subwavelength and low P_{th}.[154−156] For plasmonic lasers, the NWs were positioned on SiO_2/Ag or MgF_2/Ag substrates, where the surface plasmon polariton modes stimulated and strongly confined electromagnetic modes into a subwavelength volume around the nanoscale SiO_2 or MgF_2 layer. The plasmonic NW lasers exhibited a low P_{th} and good thermal stability. Moreover, polariton lasing was also studied in $CsPbBr_3$ NWs, where the polaritons emerged from the strong coupling between the exciton and photonic modes in a NW cavity.[156]

The performance of the lasers is quantified by the P_{th}, quality factor, and their stability under the operating conditions, which depend on several factors, such as reflectivity of the end facets and length, width, and crystal quality of the NWs. High-quality NWs produce lasing with a lower threshold owing to low defect density and nonradiative recombinations. However, the effect of the length of the NWs on the lasing performance is not well known and is essential to study. Further, electrically excited perovskite NW lasers are yet to be explored and may be the next hot field of interest. To achieve electrically excited lasing action, the material requires a high-quality gain medium with slow nonradiative decay pathways, high carrier density levels required for population inversion, large and balanced mobilities, excess free-carrier density to minimize resistive heat loss, good thermal stability, a large gain cross-section at the lasing wavelength, and sharp band tails marked by a low Urbach energy.[47] In Table 2 we have listed a few NWs-based lasers and their performances.

Table 2. Characteristic Parameters of Perovskite NWs-Based Lasers

material	lasing wavelength	P_{th}	Q	ref
$MAPbI_3$ NWs	787 nm	220 nJ cm^{-2}	3600	40
$MAPbBr_3$ NWs	550 nm	300 nJ cm^{-2}	2360 ± 30	
$MAPbI_3$ NWs	785 nm	9.2 $\mu J\ cm^{-2}$	1260	56
$MAPbBr_3$ NWs	550 nm	9.8 $\mu J\ cm^{-2}$	1260	
$(FA/MA)PbX_3$ NWs	green - red	3–30 $\mu J\ cm^{-2}$	1500–3200	151
$CsPbBr_3$ NWs	530 nm	5 $\mu J\ cm^{-2}$	1009 ± 5	150
$CsPbCl_3$ NWs	430 nm	86 $\mu J\ cm^{-2}$	690 ± 70	
$CsPbBr_3$ NWs	538 nm	6.2 $\mu J\ cm^{-2}$	2069	152
$CsPbCl_3$ NWs	424 nm	6 $\mu J\ cm^{-2}$	1300	
$CsPbBr_3$	543 nm	14.1 $\mu J\ cm^{-2}$	3500	83
$CsPbBr_3$	green	4.1 $\mu J\ cm^{-2}$	2675	86
$CsPbCl_3$	blue	11 $\mu J\ cm^{-2}$	1931	
$CsPbI_3$	red	21 $\mu J\ cm^{-2}$	2256	
$CsPbBr_xI_{3-x}$	521 and 556 nm	16 and 28 $\mu J\ cm^{-2}$		153

2.3. Perovskite NWs Light-Emitting Diodes. Light-emitting-diodes (LEDs) convert electrical signals into light signals, where the emission wavelength or color is decided by the energy bandgap of the active emissive layer. Recently, perovskites have been established as potential candidates for the development of efficient LEDs. The high performance of LEDs is attributed to their high photoluminescence quantum yields (PLQYs), tunable color emission, wide color gamut, and high charge carrier mobilities.[157−162] Along with the bulk-phase (3D) and quantum structures (0D)-based perovskite thin films, 1D NWs withal have motivated considerable research interest in designing the LEDs.[41,163,164] The large aspect ratio of perovskite NWs is propitious for better light

https://doi.org/10.1021/acsaem.1c03284
ACS Appl. Energy Mater. 2022, 5, 1342−1377

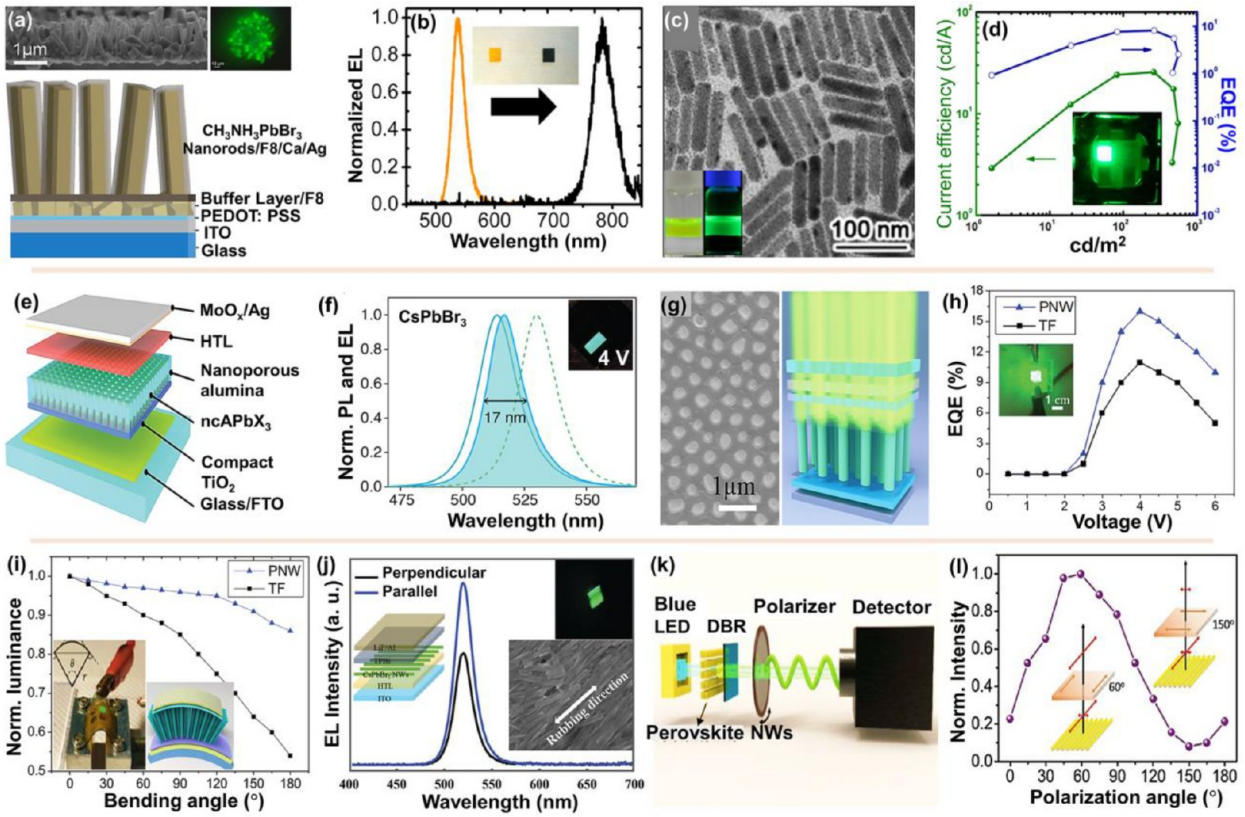

Figure 14. (a) Cross-sectional SEM image of perovskite nanorods array (top left), electroluminescence image of the perovskite NR array-based LED (top right), and schematic of the device structure of a vertically grown $MAPbBr_3$ NRs array-based LED (bottom). (b) Normalized EL spectra of $MAPbBr_3$ and $MAPbI_3$ NRs array-based LEDs. Adapted with permission from ref 163. Copyright 2015 American Chemical Society. (c) TEM image of $CsPbBr_3$ NRs with the aspect ratio of 5.0. The inset shows digital photographs of the perovskite NRs solution under normal light (left) and UV irradiation of 365 nm (right). (d) Current efficiency/EQE vs luminance curves of the NWs-based LED. The inset shows a digital photograph of the LED operated at 5 V. Adapted with permission from ref 164. Copyright 2019 American Chemical Society. (e) Schematic of the multilayered LED device structure with NWs grown within the AAO template. (f) Recorded EL spectra (filled curve) of a $CsPbBr_3$ NWs-based LED with bulk (dashed line) and confined PL spectra (solid line). The inset shows a digital photograph of the operating $CsPbBr_3$ LED at 4 V and displaying cyan-green EL over the entire area. Adapted with permission from ref 165. Copyright 2016 arXiv. (g) Top-view SEM image of the perovskite NWs grown within the PAM template (right) and schematic representation of the multilayer LED device structure with the vertically grown NWs and the illustration of the light emission from the NWs (left). (h) EQE vs V curves of the perovskite NWs and thin-film-based LEDs. The inset shows a digital photograph of the LED operated at 4 V with an active device area of 1 cm^2. (i) Mechanical flexibility test of the perovskite NWs-based and thin-film-based LEDs with different bending angles. The inset shows the working LED at bending condition (left) and a scheme of the NWs-based LED under bending conditions (right). Adapted with permission from ref 41. Copyright 2020 American Chemical Society. (j) Recorded EL spectra of dry-rubbed $CsPbBr_3$ NWs-based LED in two orthogonal directions. The inset shows a scheme of the multilayer device structure (left), a digital photograph of the working $CsPbBr_3$ NWs LED (top right), and a SEM image of the mechanically dry-rubbed $CsPbBr_3$ NWs (bottom right). Adapted with permission from ref 166. Copyright 2020 Royal Society of Chemistry. (k) Schematic representation of the polarization experimental through-plane optical device setup using a GaN LED, perovskite NW/AAO, DBR layer, polarizer, and detector. (l) Polarized emission characteristics of perovskite NW arrays. The inset illustrates the angle of the polarizer located at 60° and 150° relative to the NWs array. Adapted with permission from ref 167. Copyright 2020 Wiley-VCH.

propagation, and perovskite NWs have relatively better light extraction efficiency than the bulk-phase or NCs-based thin films, as realized from the finite-difference time domain (FDTD) modeling.[41] These characteristics make the NWs favorable for photonic circuit integrations. Few reports have demonstrated the incorporation of perovskite NWs and NRs for the fabrication of LEDs.[41,163,164]

In 2015, for the first time, Wong et al. demonstrated the fabrication of LEDs using perovskite NR arrays as an active emissive layer.[163] The high-quality $MAPbBr_3$ perovskite NR arrays were directly grown on a glass/ITO/PEDOT:PSS layer by coating the saturated methanolic solution of $PbAc_2$ and further converted into $MAPbI_3$ NRs through anion-exchange reaction with MAI vapor while preserving their initial geometry. The obtained NRs exceeded 1 μm in length and 100 nm in diameter and also exhibited a square cross-section (Figure 14a). Upon employing the NRs as an active layer for the fabrication of green and red color LEDs, the corresponding LEDs exhibited the maximum emission peaks at 533 and 782 nm, respectively (Figure 14b).[163] To grow the perovskite NRs/NWs in a facile solution medium, Yang et al. reported the preparation of monodispersed $CsPbBr_3$ NRs (Figure 14c) with tunable aspect ratios of 2.0, 2.5, 3.0, 5.0, 7.5, and 17.0 through an interfacial conversion from the initial Cs_4PbBr_6 nanocrystals by a water-triggered transformation reaction.[164] The resultant $CsPbBr_3$ NRs exhibited a high PLQY of 87%. Fascinatingly, these NRs present a higher valence band position (−5.99 eV) than the conventional $CsPbBr_3$ nanocubes (−6.17 eV), which induces better hole injection by reducing the band offset and is crucial for achieving high-performance LEDs. The $CsPbBr_3$

https://doi.org/10.1021/acsaem.1c03284
ACS Appl. Energy Mater. 2022, 5, 1342−1377

Table 3. Performance Parameters of Perovskite NWs-Based LEDs

material	type	LED device structure	wavelength (color)	L	CE	EQE	ref
$MAPbI_3$, $MAPbBr_3$ NRs	vertical array	ITO/PEDOT:PSS/buffer layer/F8/perovskite NRs/F8/Ca/Ag	782 nm, 533 nm	–	–	–	163
$CsPbBr_3$ NRs	colloidal NR thin films	ITO/PEDOT:PSS/TFB/perovskite NRs/TPBi/LiF/Al	520 nm	2557	25.7	8.2	164
MABr-modified $CsPbBr_3$ NWs	template-assisted vertical array	ITO/PEDOT:PSS/$CsPbBr_3$ NWs/TPBi/LiF/Al	green	12016	–	16	41
$CsPbBr_3$ NWs	template-assisted vertical array	FTO/TiO_2/$CsPbBr_3$ NWs/HTL/MoO_x/Ag	518 nm	100	–	–	165
$CsPbBr_3$ NWs	oriented by mechanical rubbing	ITO/PEDOT:PSS/PolyTPD/PVK $CsPbBr_3$ NWs/TPBi/LiF/Al	519 nm	3.88	–	0.08	166

NRs-based LEDs exhibited a peak wavelength of 520 nm, maximum brightness of 2557 cd/m^2, current efficiency of 25.7 cd/A, and EQE of 8.2% (Figure 14d).[164] Furthermore, the color-tunable emission within the visible region from blue to the red has been achieved in NRs through the anion-exchange reactions with NaCl and NaI, respectively.[164]

In general, tunable emission from perovskites has been achieved through the mixed-halide compositions. However, color-tunable emission in single halide composition-based perovskite NWs was accomplished by fine-tuning the bandgap through the quantum confinement effect in a nanoporous alumina template, which does not involve the conventional manipulation of the mixed-halide stoichiometry.[165] Reducing the pore size of the template resulted in the blue-shift emission spectra through an efficacious quantum confinement effect. Nanoporous alumina containing the perovskite NWs was used as an active emissive layer for the demonstration of the NWs-based LEDs. The LED device structure is comprised of glass/FTO/compact TiO_2/NWs in nanoporous alumina/HTL/MoO_x/Ag (Figure 14e), and the corresponding PL and EL spectra are presented in Figure 14f. The LEDs exhibited the maximum brightness of over 100 cd/m^2 and a turn-on voltage of 2.5 V. The low brightness exhibited by the devices may be attributed to the improper growth of the NWs or inferior contact/junction between the NWs subsisting within the pores of the template and charge-transport layers.[165] Similarly, the perovskite NWs array was designed by utilizing a porous alumina membrane (PAM) (Figure 14g, left panel), where the NWs were grown within the template pores via capillary-effect-assisted growth.[41] The geometry of the NWs was tuned by selecting the different dimensions of the PAM templates. These NWs-based LEDs exhibited relatively improved device performance and stability compared to the thin-film LEDs counterparts. A schematic representation of the emission from the NWs-based LEDs is displayed in Figure 14g (right panel). The NWs-based green LEDs displayed a maximum brightness of 12 016 cd/m^2 and a maximum EQE of 16% (Figure 14h), which are better than the thin-film-based LEDs' maximum brightness of 10 953 cd/m^2 and EQE of 11% (Figure 14h). The increased EQE is attributed to the better light extraction efficiency of the NWs owing to the leaky mode behavior in the NWs at the emission wavelength. The enhanced stability is due to the template protection of NWs against the lateral incursion of external moisture and oxygen.[41] Besides, the NWs-based LEDs demonstrated better mechanical flexibility and bendability as compared to thin-film LEDs (Figure 14i), which is an added advantage. Each NW is surrounded by template packaging material which has excellent mechanical robustness; thus, bending the device does not introduce any crack line within the NWs as long as the PAM holds it. On the contrary, the polycrystalline thin-film counterparts engender the crack lines when subjected to bending conditions of certain degrees, consequently leading to notable performance degradation under bending conditions compared to NWs (Figure 14i).[41]

Along with the conventional light emission, the NWs have additionally exhibited a polarization effect owing to the anisotropic nature of their 1D geometry.[166−168] Herein, $CsPbBr_3$ NWs were synthesized by the hot-injection colloidal synthesis method, and the oriented NWs-based thin films were achieved by using a mechanical rubbing method (inset of Figure 14j).[166] The oriented NWs-based thin films showed polarized PL behavior and were also used for the fabrication of polarized LEDs (Figure 14j). The devices exhibited a turn-on voltage of 6.5 V and an EQE of 0.08%.[166] Similarly, the highly ordered perovskite NWs arrays were fabricated within the AAO template by employing an inkjet-printing process.[167] The NWs were grown in the AAO template by inkjet-printing on one side while applying vacuum-pumping on another side of the template to guide the ink flow into the AAO pores. A schematic illustration of the experimental polarization setup is shown in Figure 14k. The perovskite NWs arrays exhibited a cycle of sine fluctuation subjected to the rotation of the polarizer from 0° to 180° (Figure 14l), which indicates a high polarization effect of the NWs. The polarized emission measurements revealed the maximum and minimum intensities at 60° and 150°, respectively (Figure 14l).[167] Likewise, recently, 3D-printed nanocomposite inks were developed comprising perovskite NWs suspended in a polystyrene−polyisoprene−polystyrene block copolymer matrix.[168] Alignment of the NWs was achieved through a programmed printing path, and they exhibited highly polarized absorption and emission properties. These NWs were also used for the demonstration of polarized full-color display applications. Tunable emission was realized from the pixel array subjected to the rotation of the polarizer, where the red, green, and blue colors were obtained when the polarizers were parallel to the print directions, whereas the mixed colors of yellow (red + green), purple (red + blue), and cyan (blue + green) were achieved when the polarizers were positioned at 30°.[168] These studies revealed that these composites can provide new avenues for the development of functional devices for, e.g., encryption, optical displays, and information storage.

The 1D perovskite NWs have great potential to engender high EQE LEDs owing to their better light extraction efficiency and anisotropic directional nature. Despite the NWs showing better light propagation and efficient light extraction capacity, the research on perovskite NWs-based LEDs is still at infancy. Hence, effective growth of vertically aligned NWs and establishment of better contact between the charge transport/injection layers with NWs existing within the templates

https://doi.org/10.1021/acsaem.1c03284
ACS Appl. Energy Mater. 2022, 5, 1342−1377

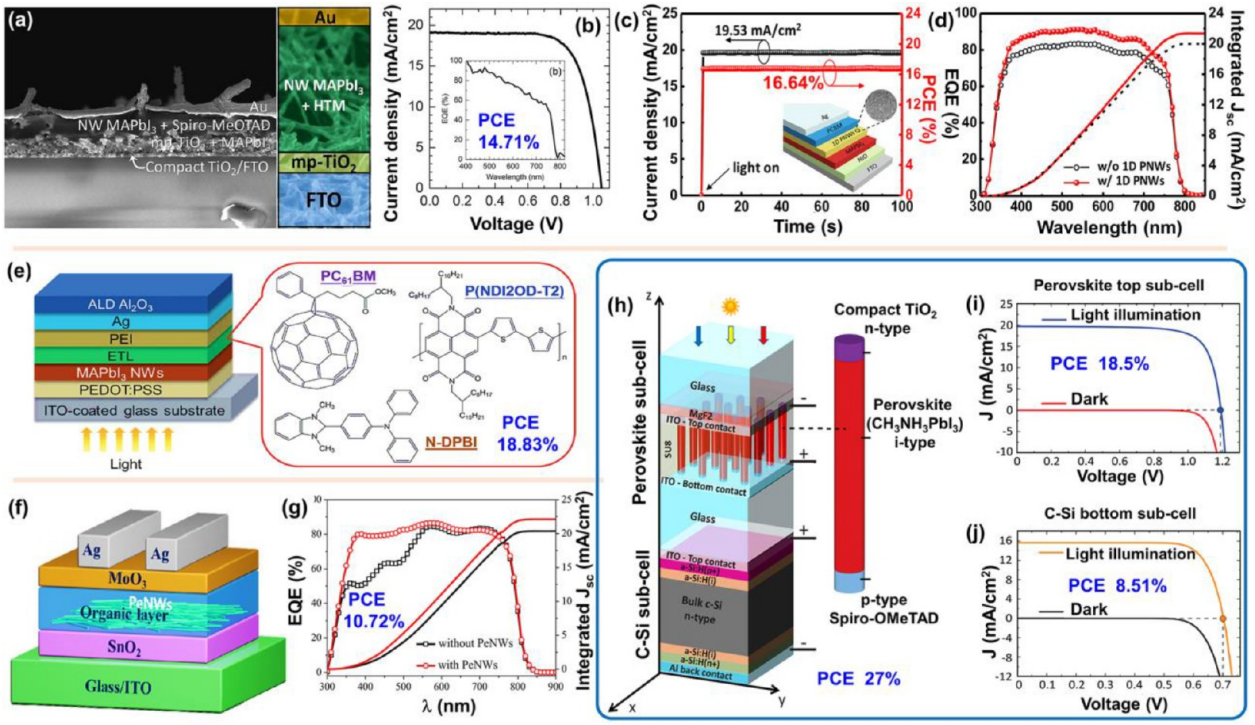

Figure 15. (a) Cross-sectional SEM image of the multilayer solar cell (left) with corresponding false color coding for each layer (right). (b) Current−voltage characteristics measured at AM 1.5G illumination with a light intensity of 98.6 mW/cm^2. Adapted with permission from ref 49. Copyright 2015 American Chemical Society. (c) J_{SC} and PCE stability test of the corresponding PV device at the maximum outputs with the voltage of 0.85 V. The inset shows the device structure of a PV with 1D NWs on the surface of a $MAPbI_3$ thin film. (d) EQE and integrated J_{SC} curve of the PV vs wavelength. Adapted with permission from ref 173. Copyright 2018 IOP Publishing Group. (e) Schematic representation of the PV device architecture and the molecular structures of ETLs used. Adapted with permission from ref 42. Copyright 2017 Royal Society of Chemistry. (f) Schematic diagram of the PV device with the combination of perovskite NWs and organic layer. (g) EQE spectra and J_{SC} curves of the PVs with and without the perovskite NWs. Adapted with permission from ref 174. Copyright 2020 American Chemical Society. (h) Schematic of NWs or nanopillars array-based perovskite/c-Si tandem PV. The PV cell comprises a top subcell composed of periodically arranged nanopillar perovskites ($MAPbI_3$) and a c-Si heterojunction bottom subcell. (i) $J-V$ characteristics of the top $MAPbI_3$ perovskite subcell under light and dark illumination conditions. (j) $J-V$ characteristics of the bottom c-Si subcell under light and dark illumination conditions. Adapted with permission from ref 175. Copyright 2017 American Chemical Society.

are prerequisites for the development of high-performance LEDs. A few perovskite NWs-based LEDs' performances are presented in Table 3.

2.4. Perovskite NWs Photovoltaic Cells. Perovskite thin films have been studied extensively for the demonstration of their PV applications. Perovskites have excellent light absorption, longer diffusion lengths, and low-temperature solution processability, which make them the most promising material for next-generation PV applications.[27,169−172] On the other hand, perovskite NWs have an inherently large surface area that improves the light absorption capacity, and carrier confinement in the other two dimensions eases the charge transport on account of their highly crystalline 1D structure. Moreover, the 1D NWs have been found to exhibit significant advantages over bulk-phase thin films, including better light trapping, better lateral conductivity, better charge carrier separation/extraction, and excellent mechanical flexibility, which are highly beneficial for high-performance, flexible PV device applications.[49,50]

Halide perovskites-based $MAPbI_3$ NWs were employed for the fabrication of photovoltaic cells for the first time in 2015, where the devices displayed a PCE of 14.71% at AM 1.5G.[49] Here, $MAPbI_3$ NWs were synthesized by rationally controlling the DMF solvent in an IPA solution of MAI via a two-step spin-coating process. A cross-sectional SEM image, multilayer schematic representation of the fabricated PV devices, and their characteristic curves are displayed in Figure 15a,b. The devices displayed a short-circuit current density (J_{sc}) of 19.12 mA cm^{-2}, an open-circuit voltage (V_{oc}) of 1.052 V, and a fill factor (FF) of 0.721. The NWs-based PV devices exhibited enhanced lateral conductivity and faster charge carrier separation than the bulk-phase $MAPbI_3$ thin films (cuboid), leading to the best performance of $MAPbI_3$ NWs-based PVs. Here, NWs established better contact with the hole-transporting material (HTM) owing to their increased surface area that improves hole extraction in perovskite NWs for enhanced performance.[49]

To further ameliorate the PCE of perovskite NWs-based PV devices, a p-i-n-type inverted structure FTO/NiO/$MAPbI_3$ film/1D $MAPbI_3$ NWs/PCBM/Ag configuration was devised.[173] The PV devices using the combination of both the perovskite thin film and 1D NWs exhibited an improved PCE of 16.66%, V_{oc} of 1.07 V, J_{sc} of 21.51 mA cm^{-2}, and FF of 0.723, along with negligible hysteresis (Figure 15c). Notably, the devices with 1D NWs showed enhanced charge carrier transport between the $MAPbI_3$ thin film and electron transport layer (ETL) as a fast migration channel that leads to high EQE of 91% (Figure 15d) and better PCE stability in ambient conditions over 30 days. Furthermore, a similar p-i-n-type inverted structure was configured as ITO/PEDOT:PSS/

https://doi.org/10.1021/acsaem.1c03284
ACS Appl. Energy Mater. 2022, 5, 1342−1377

Table 4. Performance of the Reported Perovskite NWs-Based PVs

orientation type	materials	J_{SC} (mA/cm^2)	V_{OC} (V)	FF	PCE (%)	ref
random	$MAPbI_3$	19.12	1.052 V	0.721	14.71	49
random	$MAPbI_3$	23.8 ± 0.1	1.04	0.746	18.74	50
random	$MAPbI_3$	22.47 ± 0.70	1.12 ± 0.013	0.70 ± 0.01	17.62 ± 0.46	51
random	$CsPbBr_3$	2.96	0.851	0.445	1.21	58
random	$MAPbI_3$ thin film and NWs	21.51	1.07	0.723	16.66	173
random	$MAPbI_3$	21.39	1.01	0.80	18.83	42
random	$MAPbI_3$	23.92	0.819	0.547	10.72	174

$MAPbI_3$ NWs/doped ETL/polyethylenimine (PEI)/Ag cathode/ALD Al_2O_3 encapsulation layer, where the devices demonstrated an improved PCE of 18.83%, V_{oc} of 1.01 V, J_{sc} of 21.39 mA cm^{-2}, and FF of 0.80, with hysteresis-less $J-V$ characteristics. (Figure 15e).[42] The improved PCE was attributed to doping the P(NDI2OD-T2) ETL with the air-stable dopant 4-(1,3-dimethyl-2,3-dihydro-1*H*-benzimidazol-2-yl)-*N*,*N*-diphenylaniline (N-DPBI), which enhanced the electron extraction properties by minimizing resistive losses and improved the surface coverage of the P(NDI2OD-T2) ETL on the $MAPbI_3$ NW layer. Besides, the Al_2O_3-encapsulated NWs-based devices retained almost 92% of their initial efficiency over 6000 h, which demonstrates that the devices exhibit excellent ambient stability.

The PCE of $MAPbI_3$ NWs-based solar cells was further improved to 18.7% in 2018.[50] The PV cells were fabricated using different morphologies of $MAPbI_3$ perovskites, including the compact bulk-phase thin films and NWs. The NWs-based PV devices exhibited an enhanced PCE of 18.7%, compared to the thin-film-based perovskite PV cell with a PCE of 14.03%.[50] The NWs-based PVs displayed a maximum J_{sc} of 23.8 ± 0.1 mA cm^{-2}, V_{oc} of 1.04 V, and FF of 0.746, and showed hysteresis-free curves, which implies no accumulation of charge carriers and efficient charge carrier transfer within the device. Despite employing the perovskite NWs as the individual active layer in the PV devices, very recently the efficient non-fullerene acceptor-based organic solar cell with additional $MAPbI_3$ NWs was documented (Figure 15f) and exhibited a PCE of 10.72% in 2020.[174] Here, the perovskite NWs incorporated at the interface of SnO_2 and PBDB-T-SF:IT-4F, which effectively solved the incompatibility between the two dissimilar materials without affecting their intrinsic properties.[174] This combination improved and stabilized the PV's performance compared to that of the PVs without the NWs (Figure 15g).

As a matter of fact, organic perovskites are sensitive to the open ambient conditions, and ergo the degradation of the device. Hence, a need of the hour is to develop stable perovskite compositions for their long-term utilization for practical applications. To further improve the PV device stability, all-inorganic $CsPbX_3$ perovskite NWs were employed as an active layer for the fabrication.[58] The first all-inorganic perovskite NWs-based PV device was demonstrated in 2017, with the structure FTO glass/TiO_2 compact layer/$CsPbX_3$ NWs/spiro-OMeTAD/Au. Nevertheless, the devices showed lower PCEs of 0.11% and 1.21% for $CsPbI_3$ and $CsPbBr_3$ NWs, respectively.[58] Though the devices displayed poor performance, they exhibited excellent stability by retaining 99% of the initial PCE over 5500 h aging at ambient conditions, which hints that accelerating the PCEs of all-inorganic PVs to the level of their counterparts is crucial for practical PV applications.

One of the efficacious approaches to improve the efficiency of perovskite PVs is their integration in a tandem configuration with a different type of PVs as dual-junction PVs. Here, a tandem PV cell was demonstrated using a nanopillar array of $MAPbI_3$ in combination with the c-silicon.[175] A novel four-terminal nanopillared perovskite/c-Si tandem solar cell was investigated through a predictive 3D finite-element-based optoelectrical model and displayed a simulated efficiency of 27%. A schematic representation of the device is shown in Figure 15h. It is the combination of a nanopillared perovskite $MAPbI_3$ as top subcell and a c-Si heterojunction as bottom subcell. The efficiency contributions were 18.5% and 8.51% from the top and bottom subcells (Figure 15i,j), respectively, and a total PCE of 27% was achieved for the complete tandem cell.[175] A comparative study and an investigation of nanopillar perovskite-based tandem cells and planar perovskite film-based tandem cells were also performed and found that the relative efficiency enhancement of about 21% is in favor of the nanopatterned perovskite. This reveals that the aligned NWs are the best option for achieving high PCEs rather than the randomly oriented perovskite NWs as well as thin-film-based planar perovskite PV cells.[175]

The numerical modeling approach revealed the capacity of the NWs to enhance the efficiency of PV devices. However, there are no significant experimental reports on the effective vertical or parallel alignment of NWs-based PV devices. The reported NWs-based PVs produced lower PCEs than the thin-film-based PVs because of the difficulty in growing vertically oriented NWs without a template. Although the template-assisted growth of NWs provides high-quality vertically aligned NWs, their absorbance and charge transport properties are affected by the presence of the template material. Moreover, the template material establishes poor contacts between perovskite NWs and charge transport layers (CTLs); thus, the separated electron and hole charge carriers cannot be collected effectively by the electrodes. Hence, it is a prerequisite to develop free-standing vertically aligned NWs without the template. Therefore, obtaining vertically oriented high-quality NWs and improving the connectivity between the NWs and CTLs are crucial to achieve immense progress in the realm of PV applications. In Table 4 we summarize the performances of some perovskite NWs-based PVs.

2.5. Perovskite NWs Field-Effect Transistors. Field-effect transistors (FETs) are another crucial type of electronic components for advanced technological device applications. Fundamental electrical properties of individual NWs are usually studied in the FET geometry. Recently, perovskite NWs were employed as superior candidates for the realization of FET applications owing to their fewer grain boundaries, low defect density, superior charge carrier mobilities, and better conductivities. There are only a handful of reports documenting perovskite NWs-based FETs. It is challenging to design

https://doi.org/10.1021/acsaem.1c03284
ACS Appl. Energy Mater. 2022, 5, 1342−1377

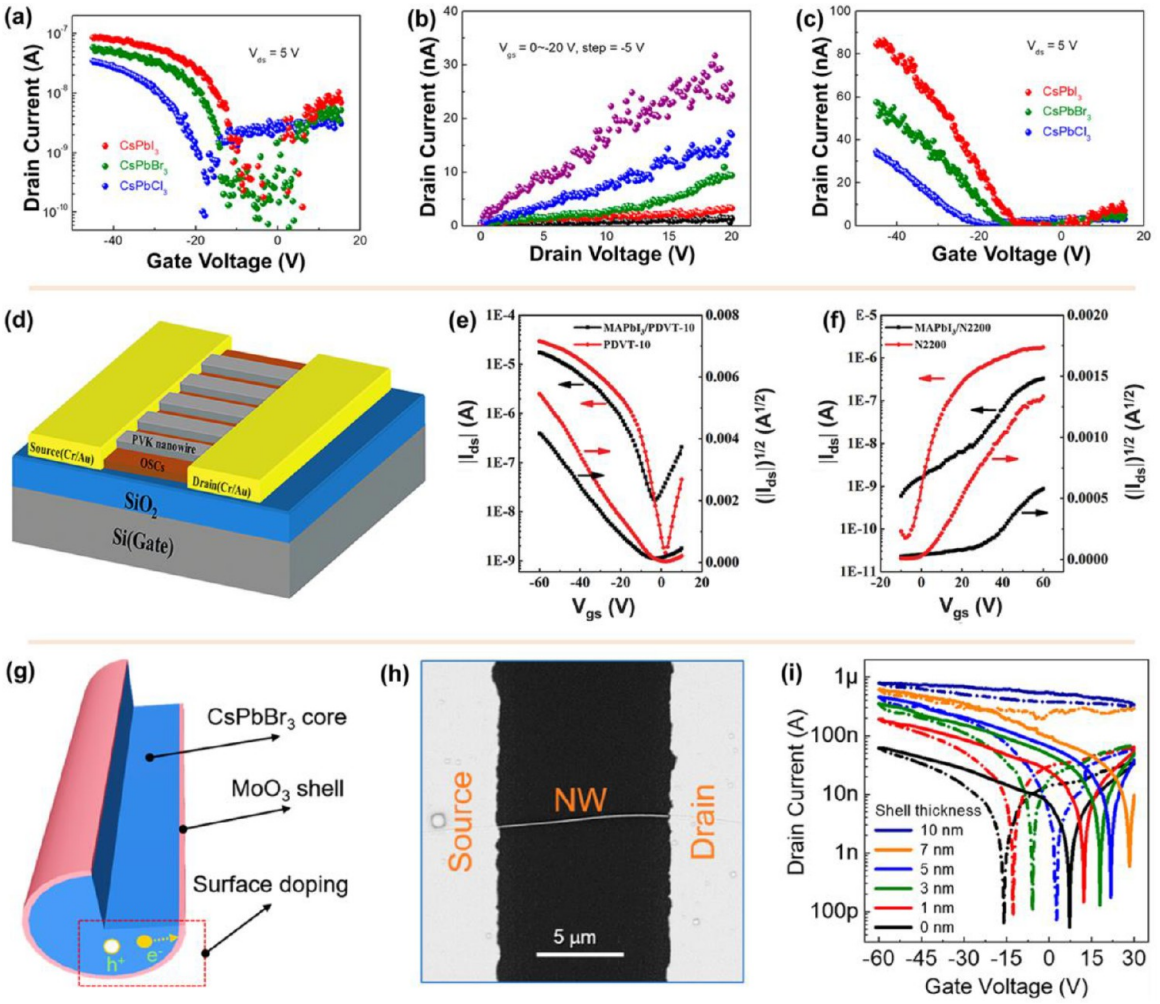

Figure 16. (a) Transfer characteristics of the VLS-grown single $CsPbX_3$ NW-based FETs (logarithmic *Y*-axis). (b) Output characteristics of the $CsPbBr_3$ NW FETs. (c) Transfer characteristics of the $CsPbX_3$ NW FETs. Adapted with permission from ref 91. Copyright 2019 American Chemical Society. (d) Schematic diagram of the phototransistor, where the channel comprises $MAPbI_3$/OSC NW heterojunctions. (e) Comparison of the transfer characteristics (I_{ds}−V_{gs}) of $MAPbI_3$/PDVT-10 NW heterojunction transistors and pure PDVT-10 NW transistors. (f) Comparison of the transfer characteristics (I_{ds}−V_{gs}) of $MAPbI_3$/N2200 NW heterojunction transistors and pure N2200 NW transistors. Adapted with permission from ref 177. Copyright 2020 Royal Society of Chemistry. (g) Schematic of the surface charge transfer doping on a $CsPbBr_3$/MoO_3 core−shell NW. (h) SEM image of the single NW FET with source and drain. (i) Forward (solid lines) and backward (dashed lines) transfer characteristic curves of $CsPbBr_3$/MoO_3 NW-based FETs with different MoO_3 (shell) thicknesses under a source−drain voltage of 5 V. Adapted with permission from ref 43. Copyright 2020 American Chemical Society.

multi-terminal FETs based on individual perovskite NWs since most of the NWs were grown on mica or sapphire substrates or directly grown within the pores of a template.

Meng et al. reported the design and fabrication of bottom-gate top-contact (BGTC) configured FETs from the perovskite NWs grown by VLS growth mechanism.[91] For the fabrication of NWs-based FETs, a dry-transfer technique was employed to transfer the as-grown NWs onto the desired SiO_2/Si substrate. Drain and source regions were defined by shadow masks, and Ti/Au electrodes were deposited by an electron beam evaporation technique. The transfer characteristics (I_{ds}−V_{gs} curves) of three different $CsPbX_3$ NW-based FET devices were obtained by sweeping the gate voltage (V_{gs}) from 15 to −45 V at a constant source−drain voltage (V_{ds}) of 5 V (Figure 16a). All the three NW-based FETs displayed the dominant p-type behavior with a slight n-type conductance at positive gate voltages. The current on/off ratios (I_{on}/I_{off}) were found to be in the order of 10^2−10^3. Figure 16b shows the output characteristic curves (I_{ds}−V_{ds} curves) of $CsPbBr_3$ NW devices resulting from sweeping the drain voltage (V_{ds}) from 0 to 20 V at a different gate-source voltage (V_{gs}). Drain current (I_{ds}) is gradually increased with the decrease of V_{gs} from 0 to −20 V with a step of −5 V. The increase in I_{ds} with a decrease of V_{gs} confirms the dominant p-type conducting nature of $CsPbBr_3$ NWs. This p-type conduction behavior could be attributed to two reasons. First, the acceptor-like interface trap states located at the amorphous oxide shells fully deplete the electrons in NWs owing to their high surface-to-volume ratios in dominant p-type conduction. Second, the NWs are self-doped with the residual Sn species during the VLS growth by the diffusion of catalyst particles, which is confirmed from the EDS analysis on the NWs. Hence, the oxidized Sn or Sn^{2+} results in Sn^{4+} ions that could act as p-type dopants of the NWs, causing them to exhibit p-type conduction behavior. COSMOL software was used to predict the hole field-effect mobility values, which were approximated to be 3.05, 2.17, and 1.06 $cm^2/(V{\cdot}s)$ for $CsPbI_3$, $CsPbBr_3$, and $CsPbCl_3$ NW FETs, respectively. The differences in charge carrier mobilities for

https://doi.org/10.1021/acsaem.1c03284
ACS Appl. Energy Mater. 2022, 5, 1342−1377

Table 5. Characteristic Parameters of Perovskite NWs-Based FETs

type of orientation	material	behavior	mobility ($cm^2/(V·s)$)	concentration (cm^{-3})	ref
single NW	$CsPbI_3$	P-type	3.05	3.62×10^{18}	91
	$CsPbBr_3$	P-type	2.17	3.29×10^{18}	
	$CsPbCl_3$	P-type	1.06	2.49×10^{18}	
horizontally aligned NWs	$MAPbI_3$/PVDT-10	P-type	0.28	–	177
	$MAPbI_3$/N2200	N-type	0.05	–	
single NW	$CsPbBr_3$	P-type	1.5	5.92×10^{18}	43
	$CsPbBr_3$–MoO_3 core–shell NW	P-type	23.3	$>9.55 \times 10^{18}$	

ionic (polar) semiconductors were explained using the Frohlich coupling mechanism. Frohlich interactions were found to be enhanced in $APbBr_3$ with respect to $APbI_3$ (for A = MA, FA). This enhancement was attributed to the higher ionicity of the Pb–Br bond as compared with the Pb–I bond. The marked decrease in the mobility across the halide series from $CsPbI_3$ to $CsPbCl_3$ is due to the increasing ionicity of the Pb–X bond. Further, threshold voltage (V_{th}) values of the FET devices were calculated from Figure 16c. The V_{th} values are found to be −10.9, −13.9, and −21.5 V for the FETs based on $CsPbI_3$, $CsPbBr_3$, and $CsPbCl_3$ NWs, respectively. These different V_{th} values of the FET devices were found to be dependent on the carrier concentration. It was also anticipated that p- to n-channel switching behavior could be achieved in perovskite NWs via careful manipulation of interface trap states.[91]

Chen et al. reported a hybrid phototransistor based on and organic semiconductor and $CsPbI_3$ perovskite NRs in the form of a bilayer structure.[176] $CsPbI_3$ NR film was coated on Si/SiO_2 substrate by dip-coating technique as the first layer. The second layer, benzothiophene (C8BTBT) organic semiconductor, was deposited by vacuum thermal evaporation. Then drain and source regions were deposited by shadow masking with 5 μm channel length. Interestingly, the fabricated hybrid transistor exhibited long-term stability. Similarly, $MAPbI_3$/organic semiconductor (OSC) (PDVT-10 and N2200) NW heterojunction-based transistors and phototransistors were fabricated.[177] Figure 16d shows a schematic of the bottom-gate and bottom-contact FET with a channel consisting of $MAPbI_3$/OSC NW heterojunctions. Two types of FET devices were fabricated using the combination of $MAPbI_3$ NWs with PDVT-10 OSC and $MAPbI_3$ NWs with N2200 OSC, respectively. The transfer characteristics of the heterojunction FET devices ($MAPbI_3$/PDVT-10, $MAPbI_3$/N2200) exhibited strong p-type and n-type FET characteristic behavior, respectively (Figure 16e,f). It was observed that $MAPbI_3$/OSC NW heterojunction-based FET devices exhibited strong responses to both the light and gate modulation. Also, the responsivity of the $MAPbI_3$/PDVT-10-based transistors, found to be 350 A W^{-1}, is the highest among the individual organic phototransistors.[177] Hence, $MAPbI_3$/OSC NW heterojunction-based transistors may be the best alternative to enhance the performance via the effective selection of the different OSCs.

Very recently, $CsPbBr_3$–MoO_3 core–shell NWs (Figure 16g) were achieved through CVD-grown perovskite NWs followed by the thermal evaporation of the MoO_3 shell layer.[43] The core–shell NWs were transferred onto p^+-Si/SiO_2 substrate, followed by depositing the drain and source top metal contacts for the realization of bottom-gate FET device configuration (Figure 16h). Figure 16i displays the dual-sweep transfer characteristic curves of core–shell NW-FET devices with various MoO_3 thicknesses ranging from 0 to 10 nm. As the MoO_3 thickness increased from 0 to 10 nm, the I_{on} increased from 62 to 790 nA. The corresponding core–shell NWs with 10 nm MoO_3-based FET devices exhibited a highest hole mobility of 23.3 $cm^2/(V·s)$. With MoO_3 surface passivation, the FET devices exhibited a dominant p-type behavior with increasing conductance with the decreasing gate voltage (V_g), implying that the injected holes via surface doping dominate the carrier transport in the FET device channel.[43] On the other hand, pristine $CsPbBr_3$ NWs-based FETs exhibited ambipolar transfer characteristics, possibly due to the balanced effective mass of holes and electrons of $CsPbBr_3$ NWs. Contrary to the conventional doping, this surface doping (non-invasive doping) does not introduce any impurity into the perovskite crystal lattice, thereby completely eliminating the charge carrier scattering by ionized dopants that leads to the enhanced carrier mobility of core–shell NWs.[43] Further increasing the MoO_3 thickness up to 50 nm resulted in a moderate FET device performance with relatively increased resistance, which confirmed that the MoO_3 shell itself is not acting as a conducting channel in core–shell NW FETs, but the interfacial electron transfer from $CsPbBr_3$ to MoO_3 is responsible for the enhanced FET performance.[43] In core–shell NW FETs, MoO_3 shell passivation effectively suppressed the environmental degradation of the perovskite core and enhances the stability of NW-based FETs. More importantly, MoO_3 shelling improved both the electrical performance and the stability of the NWs. Such core–shell NWs-based PDs showed responsivity of 2.36×10^3 A W^{-1} and EQE of over 5.48×10^5 %.[43]

The perovskite NWs exhibit higher hole mobilities than the inorganic nanocrystals, comparable to those of the organic FETs. FETs made of perovskite NWs are expected to have great potential in the future as they are further explored. Reported studies are limited to a few halide perovskite NWs (Table 5). There is a large opportunity for the development of high-performance FETs based on single perovskite NWs of various halide perovskites.

2.6. Other Applications of Perovskite NWs. Perovskite NWs have been also incorporated for the demonstration of other novel applications such as image sensor,[104] waveguide,[178] and thermoelectric[179] devices. Gu et al. realized the proof-of-concept image sensor with 1024 photodiode pixels from the vertically aligned $MAPbI_3$ NWs array.[104] The NWs array was grown within the PAM template through a CVD growth technique with an ultrahigh NWs density of 4×10^8–10^9 cm^{-2} at a size scale of 9 cm^2. A schematic representation of a 3D NWs-array-based image sensor device is depicted in Figure

https://doi.org/10.1021/acsaem.1c03284
ACS Appl. Energy Mater. 2022, 5, 1342–1377

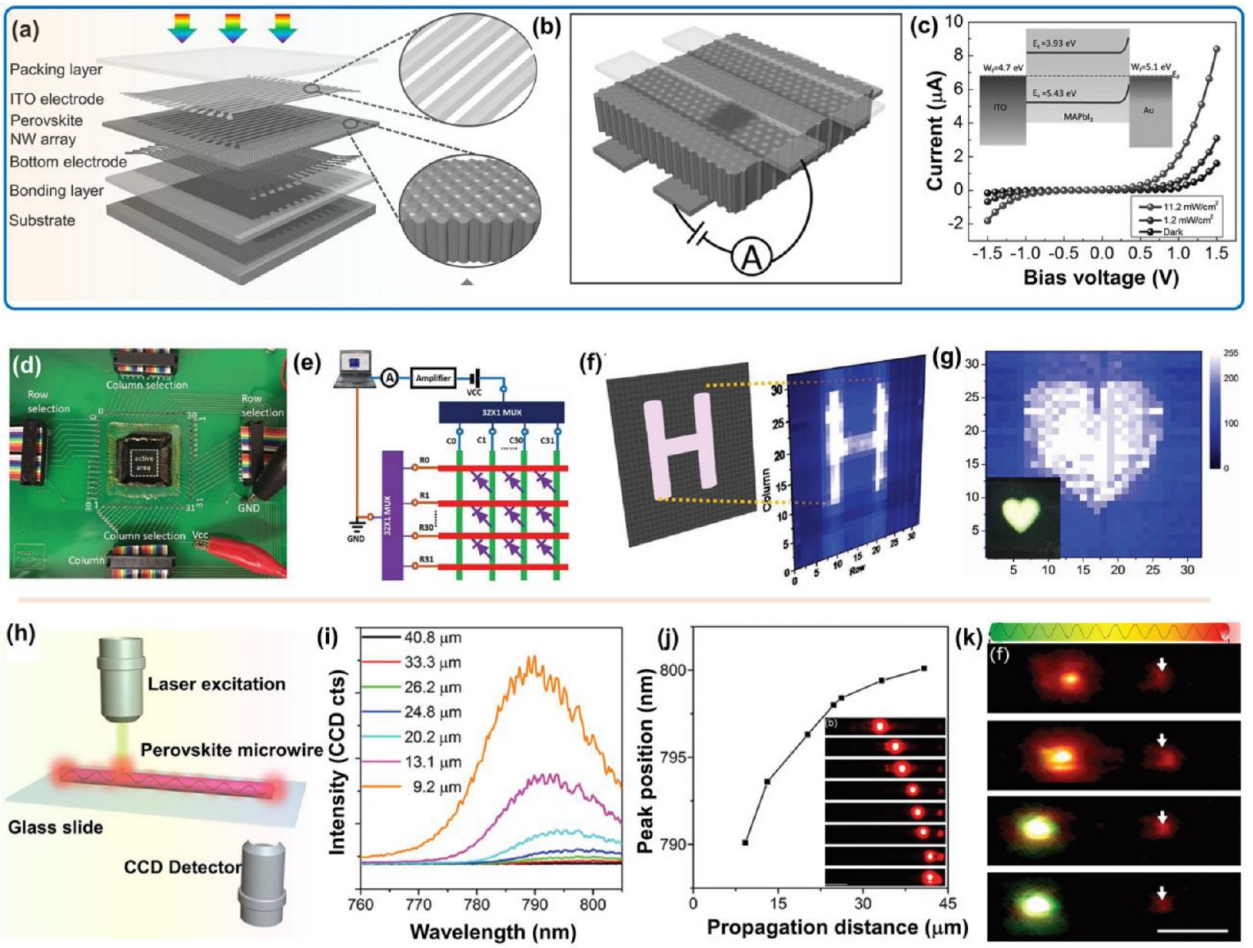

Figure 17. (a) Schematic of the multilayer device structure of the $MAPbI_3$ NW array-based image sensor. (b) Schematic of a single-pixel measurement of the image sensor. (c) Dark and light (white light) characteristic curves of the single-pixel device. The inset shows the energy band structure of a single-pixel device under zero bias in the dark conditions. (d) Digital photographic image of $MAPbI_3$ NW-based image sensor mounted on a printed circuit board. (e) Pictorial representation of the measurement setup. (f) Original and imaged letter "H". (g) Original and imaged heart symbol. Adapted with permission from ref 104. Copyright 2016 Wiley-VCH (h) Schematic illustration of the setup for waveguide measurement. (i) Spatially resolved PL spectra out-coupled at the right tip of the $MAPbI_3$ NW with different propagation distances from 9.2 to 40.8 μm. (j) PL peak position of the out-coupled light from the right end of the NW versus propagation distance. The inset shows the corresponding dark-field images of a $MAPbI_3$ NW. (k) Schematic illustrations of light propagation in a composition-graded perovskite NW along the long axis (top) and darkfield PL images of the composition-graded perovskite NW under local excitation; scale bar, 5 μm. Adapted with permission from ref 178. Copyright 2016 Royal Society of Chemistry.

17a. The bottom (Au, 100 nm) and top (ITO, 100 nm) electrodes were designed with the help of a shadow mask by using thermal evaporation and sputtering, respectively. Each pixel has a footprint of 200 × 200 μm with a periodicity of 400 μm, which consists of approximately 1.6×10^5 perovskite NWs, where each pixel works as a PD/photodiode (Figure 17b). Measured $I-V$ characteristic curves of individual pixels under the illumination of different light intensities are shown in Figure 17c. The devices showed good photoresponse under light illumination. The asymmetric nature of the $I-V$ curve revealed a rectification behavior, which implies that the pixel device is acting as a Schottky photodiode.[104] Overall, the device showed responsivity of over 35 mAW^{-1}, specific detectivity of 10^{10} Jones, rise time of 20.47 ms, and fall time of 13.81 ms. Moreover, the full-fledged image sensor mounted on a printed circuit board along with the image sensing characterization of original and imaged patterns are displayed in Figure 17d–g. The resolved projections of imaged characters "H" and a heart symbol on the image sensor indicate the effective imaging function of the 3D NWs array (Figure 17 f,g). In addition, the 3D NWs-array-based image sensor also demonstrated excellent mechanical flexibility under various bending conditions,[104] which can be applicable for use in wearable/flexible electronics, artificial skin, and electronic eye applications.

Wang et al. demonstrated optical waveguiding phenomena from 1D perovskite NWs with minimal propagation losses.[178] Here, NWs were designed through the combination of a solution process for PbI_2 NWs, followed by vapor-phase conversion with the help of MAI for obtaining $MAPbI_3$ NWs. The NWs were excited with a finely focused laser (Figure 17h), and the corresponding PL spectra (Figure 17i) and images (inset of Figure 17j) were recorded. Herein, the laser spot traveled along the NW's length and was detected at another end, revealing an impressive waveguiding behavior.[178] Besides, the strong out-coupling PL at the rightmost tip revealed a directional propagation of down-converted light, where the photocarriers propagate through the grain boundaries followed by the recombination at the NW tip. Notably, the out-coupled light was weakened with the increase in distance owing to the

https://doi.org/10.1021/acsaem.1c03284
ACS Appl. Energy Mater. 2022, 5, 1342−1377

propagation losses, and the red-shift in the PL spectra revealed the re-absorption and re-emission of the propagated light within the NW (Figure 17j).[178] For $MAPbI_3$ NWs, the propagation loss was found to be 0.30 dB μm^{-1} for a propagation distance of 100 μm. Similarly, the waveguiding nature was also studied for other halide compositions such as $MAPbBr_3$, $MAPbBr_3I_{3-x}$, and composition-graded NWs. Similar behavior was observed from $MAPbBr_3$ and $MAPbBr_3I_{3-x}$ NWs exhibiting green- and orange-colored emissions, respectively. In the case of composition-graded NWs, the light changes from green to red, depending on the excitation position, and the red light was out-coupled at the rightmost tip of the NW owing to the decreasing bandgap (gradient) from left to right (Figure 17k).[178]

Lee et al. investigated the thermal conducting properties of all-inorganic halide perovskite NWs such as $CsPbI_3$, $CsPbBr_3$, and $CsSnI_3$ where the NWs were synthesized using the solution-phase method.[179] The RT lattice thermal conductivities of $CsPbI_3$, $CsPbBr_3$, and $CsSnI_3$ NWs were found to be 0.45 ± 0.05, 0.42 ± 0.04, and 0.38 ± 0.04 W m^{-1} K^{-1}, respectively, which were commensurate with and even smaller than those of various crystals. The obtained ultralow thermal conductivity was mainly attributed to the cluster rattling mechanism. Moreover, $CsSnI_3$ exhibited ultralow thermal conductivity, a high electrical conductivity of 282 S·cm^{-1}, and a high hole mobility of 394 $cm^2/(V·s)$, which makes it a promising material for unique electrically conductive thermal insulator-based applications.[179] Despite the progression of these applications, more efforts are required to expand the horizons of the perovskite NWs.

3. CONCLUSION AND FUTURE DIRECTION

To conclude, 1D perovskite NWs are believed to be the most promising candidates for various photonic applications as alternatives to their polycrystalline bulk-phase thin film and nanocrystal counterparts, yet much more effort is required to obtain high-quality and uniform NWs. In this Review, we have scrupulously discussed the recent progress accomplished with the hybrid organic−inorganic and all-inorganic 1D perovskite NWs, spanning from their various synthesis methods, including their guiding and growth mechanisms for each method, to their potential optoelectronic applications, such as PDs, lasers, LEDs, PVs, and FETs. There is a strong relationship between the perovskites' morphologies and their optoelectronic properties. Mainly, 1D perovskite NWs have revealed exceptional performance in various applications owing to their strong quantum confinement effect, tunable optical bandgap, large surface area, better charge transport, and unique one-directional anisotropic geometry. The figures of merit or characteristic parameters of the devices were summarized in a table format for each application. These NWs have demonstrated impressive PD performance in both the single and aligned NWs arrays with high responsivity, response times, and detectivity owing to good light absorption, low defect density, low recombination rate, superior mobility, and long charge carrier lifetime. The perovskite NWs have exhibited low lasing threshold values and high optical gain that are crucial for efficient lasing applications. The FETs designed from the perovskite NWs have displayed enhanced mobilities and stability, paving the way for them to become next-generation materials for FETs. However, moderate performance was achieved from both the perovskite NWs-based PVs and LEDs despite their having better light absorption, charge separation and extraction, light trapping and harvesting, and propagation capabilities than the polycrystalline, bulk-phase, or nanocrystal thin films. The compromises in performances may be attributed to improper contacts between the NWs and CTLs due to the presence of the surrounding template material. In the present scenario, perovskite NWs have attracted considerable research interests in fundamental science as well as in potential future device applications due to their exceptional properties other than dimensionalities.

Despite the excellent progress and high performance from perovskite NWs-based optoelectronic and electronic devices, considerable challenges remain in their growth methods and their integration into device applications. Foremost is the optimization of growth methods to achieve high-quality NWs along with uniform size distribution, aspect ratios, reliable reproducibility, etc. Second is the chemical, thermal, and ambient stability of the perovskites, which must be addressed for their successful integration into practical applications and to accomplish long-term device reliability. Third, techniques are required to achieve orderly aligned NWs over a specific large area. Fourth is the need to gain precise control over the position and microfabrication for the realization of miniaturized nano-optoelectronic devices. Fifth, low-temperature and template-free methodologies must be devised to grow highly ordered and vertically aligned NWs for their integration into multilayer LEDs and PVs, which can significantly improve their performances. Besides, in template-assisted NWs, establishing better contact between the template NWs/CTLs may lead to improved device performance along with the enhanced ambient stability. The PDs and lasers exhibited better device performance from the hybrid organic−inorganic NWs compared to the all-inorganic NWs, yet displayed poor stability, which is the most prominent bottleneck that needs to be addressed to develop the optoelectronic devices for practical applications as well as need to improve the performance of all-inorganic perovskite NWs-based devices. Moreover, the preparation of single-crystalline NWs made up of layered quasi-2D perovskites may be the best alternative for the realization of stable perovskites for various next-generation integrated optoelectronics. Despite the unabating race for high performance, addressing the long-term stability and realizing sustainable devices, the synergistic efforts through global consortia are expected to accomplish the aforementioned challenges.

AUTHOR INFORMATION

Corresponding Author

Murali Banavoth − *Solar Cells and Photonics Research Laboratory, School of Chemistry, University of Hyderabad, Hyderabad 500046 Telangana State, India;* orcid.org/0000-0002-7806-2274; Email: murali.banavoth@uohyd.ac.in

Authors

Gundam Sandeep Kumar − *Solar Cells and Photonics Research Laboratory, School of Chemistry, University of Hyderabad, Hyderabad 500046 Telangana State, India;* orcid.org/0000-0002-9339-8817

Ranadeep Raj Sumukam − *Solar Cells and Photonics Research Laboratory, School of Chemistry, University of Hyderabad, Hyderabad 500046 Telangana State, India*

https://doi.org/10.1021/acsaem.1c03284
ACS Appl. Energy Mater. 2022, 5, 1342−1377

Rakesh Kumar Rajaboina − *Department of Physics, National Institute of Technology (NIT), Warangal 506004 Telangana State, India*

Ramu Naidu Savu − *Solar Cells and Photonics Research Laboratory, School of Chemistry, University of Hyderabad, Hyderabad 500046 Telangana State, India*

Mudavat Srinivas − *Department of Physics, University College of Science, Osmania University, Hyderabad 500007 Telangana State, India*

Complete contact information is available at: https://pubs.acs.org/10.1021/acsaem.1c03284

Author Contributions

#G.S.K. and R.R.S. contributed equally.

Notes

The authors declare no competing financial interest.

■ ACKNOWLEDGMENTS

G.S.K. and R.R.S. acknowledge the Council of Scientific and Industrial Research (CSIR) for Research Associate (RA) and Senior Research Fellowship (SRF), respectively. M.B. acknowledges the Department of Science and Technology (DST), Indo-Korea grant (No. INT/Korea/P-40), and EEQ/2017/000304 grants. R.R. acknowledges NIT Warangal. This work was supported by the School of Chemistry, University of Hyderabad, IoE grant (97020058).

■ REFERENCES

(1) Ha, S.-T.; Su, R.; Xing, J.; Zhang, Q.; Xiong, Q. Metal halide perovskite nanomaterials: synthesis and applications. *Chem. Sci.* **2017**, *8*, 2522−2536.

(2) Zhumekenov, A. A.; Saidaminov, M. I.; Haque, M. A.; Alarousu, E.; Sarmah, S. P.; Murali, B.; Dursun, I.; Miao, X.-H.; Abdelhady, A. L.; Wu, T.; et al. Formamidinium Lead Halide Perovskite Crystals with Unprecedented Long Carrier Dynamics and Diffusion Length. *ACS Energy Lett.* **2016**, *1*, 32−37.

(3) Murali, B.; Kolli, H. K.; Yin, J.; Ketavath, R.; Bakr, O. M.; Mohammed, O. F. Single Crystals: The Next Big Wave of Perovskite Optoelectronics. *ACS Materials Lett.* **2020**, *2*, 184−214.

(4) Chen, J.; Zhou, Y.; Fu, Y.; Pan, J.; Mohammed, O. F.; Bakr, O. M. Oriented Halide Perovskite Nanostructures and Thin Films for Optoelectronics. *Chem. Rev.* **2021**, *121*, 12112.

(5) Jung, E. H.; Jeon, N. J.; Park, E. Y.; Moon, C. S.; Shin, T. J.; Yang, T.-Y.; Noh, J. H.; Seo, J. Efficient, Stable and Scalable Perovskite Solar Cells using Poly(3-hexylthiophene). *Nature* **2019**, *567*, 511−515.

(6) Jiang, Q.; Zhao, Y.; Zhang, X.; Yang, X.; Chen, Y.; Chu, Z.; Ye, Q.; Li, X.; Yin, Z.; You, J. Surface Passivation of Perovskite Film for Efficient Solar Cells. *Nat. Photonics* **2019**, *13*, 460−466.

(7) Kim, J.-H.; Kim, Y. R.; Park, B.; Hong, S.; Hwang, I.-W.; Kim, J.; Kwon, S.; Kim, G.; Kim, H.; Lee, K. Simultaneously Passivating Cation and Anion Defects in Metal Halide Perovskite Solar Cells Using a Zwitterionic Amino Acid Additive. *Small* **2021**, *17* (3), 2005608.

(8) Lim, K.-G.; Han, T.-H.; Lee, T.-W. Engineering electrodes and metal halide perovskite materials for flexible/stretchable perovskite solar cells and light-emitting diodes. *Energy Environ. Sci.* **2021**, *14* (4), 2009−2035.

(9) Wang, Z.; Lin, Q.; Chmiel, F. P.; Sakai, N.; Herz, L. M.; Snaith, H. J. Efficient Ambient-Air-Stable Solar Cells with 2D−3D HeterostructuredButylammonium-Caesium-Formamidinium Lead Halide Perovskites. *Nat. Energy* **2017**, *2*, 17135.

(10) Tavakoli, M. M.; Saliba, M.; Yadav, P.; Holzhey, P.; Hagfeldt, A.; Zakeeruddin, S. M.; Grätzel, M. Synergistic Crystal and Interface Engineering for Efficient and Stable Perovskite Photovoltaics. *Adv. Energy Mater.* **2019**, *9*, 1802646.

(11) Reddy, S. H.; Sumukam, R. R.; Murali, B. Can Perovskite Inspired Bismuth Halide Nanocrystals Outperform Their Lead Counterparts? *J. Mater. Chem. A* **2020**, *8*, 12951−12963.

(12) Nie, R.; Sumukam, R. R.; Reddy, S. H.; Banavoth, M.; Seok, S. I. Lead-Free Perovskite Solar Cells Enabled by Hetero-Valent Substitutes. *Energy Environ. Sci.* **2020**, *13*, 2363−2385.

(13) Pourdavoud, N.; Haeger, T.; Mayer, A.; Cegielski, P. J.; Giesecke, A. L.; Heiderhoff, R.; Olthof, S.; Zaefferer, S.; Shutsko, I.; Henkel, A.; et al. Room-Temperature Stimulated Emission and Lasing in Recrystallized Cesium Lead Bromide Perovskite Thin Films. *Adv. Mater.* **2019**, *31*, 1903717.

(14) Chen, S.; Zhang, C.; Lee, J.; Han, J.; Nurmikko, A. High-Q, Low-Threshold Monolithic Perovskite Thin-Film Vertical-Cavity Lasers. *Adv. Mater.* **2017**, *29*, 1604781.

(15) Lei, L.; Dong, Q.; Gundogdu, K.; So, F. Metal Halide Perovskites for Laser Applications. *Adv. Funct. Mater.* **2021**, *31*, 2010144.

(16) Pacchioni, G. Highly efficient perovskite LEDs. *Nature Reviews Materials* **2021**, *6*, 108−108.

(17) Hassan, Y.; Park, J. H.; Crawford, M. L.; Sadhanala, A.; Lee, J.; Sadighian, J. C.; Mosconi, E.; Shivanna, R.; Radicchi, E.; Jeong, M.; Yang, C.; Choi, H.; Park, S. H.; Song, M. H.; De Angelis, F.; Wong, C. Y.; Friend, R. H.; Lee, B. R.; Snaith, H. J. Ligand-engineered bandgap stability in mixed-halide perovskite LEDs. *Nature* **2021**, *591*, 72−77.

(18) Shang, Y.; Liao, Y.; Wei, Q.; Wang, Z.; Xiang, B.; Ke, Y.; Liu, W.; Ning, Z. Highly Stable Hybrid Perovskite Light-Emitting Diodes Based on Dion-Jacobson Structure. *Sci. Adv.* **2019**, *5*, No. eaaw8072.

(19) Kumar, G. S.; Sumukam, R. R.; Murali, B. Quasi-2D Perovskite Emitters: A Boon for Efficient Blue Light-Emitting Diodes. *J. Mater. Chem. C* **2020**, *8*, 14334.

(20) Yang, Z.; Deng, Y.; Zhang, X.; Wang, S.; Chen, H.; Yang, S.; Khurgin, J.; Fang, N. X.; Zhang, X.; Ma, R. High-Performance Single-Crystalline Perovskite Thin-Film Photodetector. *Adv. Mater.* **2018**, *30*, 1704333.

(21) Zhang, M.; Zhang, F.; Wang, Y.; Zhu, L.; Hu, Y.; Lou, Z.; Hou, Y.; Teng, F. High-Performance Photodiode-Type Photodetectors Based on Polycrystalline Formamidinium Lead Iodide Perovskite Thin Films. *Sci. Rep.* **2018**, *8*, 11157.

(22) Wang, H.-P.; Li, S.; Liu, X.; Shi, Z.; Fang, X.; He, J.-H. *Low-Dimensional Metal Halide Perovskite Photodetectors* **2021**, *33* (7), 2003309.

(23) Best Research-Cell Efficiency Chart, https://www.nrel.gov/pv/cell.

(24) Kim, Y.-H.; Kim, S.; Kakekhani, A.; Park, J.; Park, J.; Lee, Y.-H.; Xu, H.; Nagane, S.; Wexler, R. B.; Kim, D.-H.; Jo, S. H.; Martínez-Sarti, L.; Tan, P.; Sadhanala, A.; Park, G.-S.; Kim, Y.-W.; Hu, B.; Bolink, H. J.; Yoo, S.; Friend, R. H.; Rappe, A. M.; Lee, T.-W. Comprehensive defect suppression in perovskite nanocrystals for high-efficiency light-emitting diodes. *Nat. Photonics* **2021**, *15*, 148−155.

(25) Deng, Y.; Peng, E.; Shao, Y.; Xiao, Z.; Dong, Q.; Huang, J. Scalable Fabrication of Efficient OrganoleadTrihalidePerovskite Solar Cells with Doctor-Bladed Active Layers. *Energy Environ. Sci.* **2015**, *8*, 1544−1550.

(26) Xiao, Z.; Wang, D.; Dong, Q.; Wang, Q.; Wei, W.; Dai, J.; Zeng, X.; Huang, J. Unraveling the Hidden Function of a Stabilizer in a Precursor in Improving Hybrid Perovskite Film Morphology for High Efficiency Solar Cells. *Energy Environ. Sci.* **2016**, *9*, 867−872.

(27) Kim, J. Y.; Lee, J.-W.; Jung, H. S.; Shin, H.; Park, N.-G. High-Efficiency Perovskite Solar Cells. *Chem. Rev.* **2020**, *120*, 7867−7918.

(28) Luo, D.; Su, R.; Zhang, W.; Gong, Q.; Zhu, R. Minimizing Non-Radiative Recombination Losses in Perovskite Solar Cells. *Nat. Rev. Mater.* **2020**, *5*, 44−60.

(29) Jena, A. K.; Kulkarni, A.; Miyasaka, T. Halide Perovskite Photovoltaics: Background, Status, and Future Prospects. *Chem. Rev.* **2019**, *119*, 3036−3103.

(30) Kwon, K. C.; Hong, K.; Van Le, Q.; Lee, S. Y.; Choi, J.; Kim, K.-B.; Kim, S. Y.; Jang, H. W. Inhibition of Ion Migration for Reliable Operation of Organolead Halide Perovskite-Based Metal/Semiconductor/Metal Broadband Photodetectors. *Adv. Funct. Mater.* **2016**, *26*, 4213−4222.
(31) Eames, C.; Frost, J. M.; Barnes, P. R. F.; O'Regan, B. C.; Walsh, A.; Islam, M. S. Ionic Transport in Hybrid Lead Iodide Perovskite Solar Cells. *Nat. Commun.* **2015**, *6*, 7497.
(32) Wang, Q.; Chen, B.; Liu, Y.; Deng, Y.; Bai, Y.; Dong, Q.; Huang, J. Scaling Behavior of Moisture-Induced Grain Degradation in Polycrystalline Hybrid Perovskite Thin Films. *Energy Environ. Sci.* **2017**, *10*, 516−522.
(33) Huang, J.; Tan, S.; Lund, P. D.; Zhou, H. Impact of H2O on Organic−Inorganic Hybrid Perovskite Solar Cells. *Energy Environ. Sci.* **2017**, *10*, 2284−2311.
(34) Hong, K.; Le, Q. V.; Kim, S. Y.; Jang, H. W. Low-Dimensional Halide Perovskites: Review and Issues. *J. Mater. Chem. C* **2018**, *6*, 2189−2209.
(35) Xu, X.; Zhang, X.; Deng, W.; Jie, J.; Zhang, X. 1D Organic−Inorganic Hybrid Perovskite Micro/Nanocrystals: Fabrication, Assembly, and Optoelectronic Applications. *Small Methods* **2018**, *2*, 1700340.
(36) Quan, L. N.; Kang, J.; Ning, C.-Z.; Yang, P. Nanowires for Photonics. *Chem. Rev.* **2019**, *119*, 9153−9169.
(37) Horváth, E.; Spina, M.; Szekrényes, Z.; Kamarás, K.; Gaal, R.; Gachet, D.; Forró, L. Nanowires of Methylammonium Lead Iodide ($CH_3NH_3PbI_3$) Prepared by Low Temperature Solution-Mediated Crystallization. *Nano Lett.* **2014**, *14*, 6761−6766.
(38) Qiu, T.; Hu, Y.; Xu, F.; Yan, Z.; Bai, F.; Jia, G.; Zhang, S. Recent Advances In One-Dimensional Halide Perovskites for Optoelectronic Applications. *Nanoscale* **2018**, *10*, 20963−20989.
(39) Deng, W.; Huang, L.; Xu, X.; Zhang, X.; Jin, X.; Lee, S.-T.; Jie, J. Ultrahigh-Responsivity Photodetectors from Perovskite Nanowire Arrays for Sequentially Tunable Spectral Measurement. *Nano Lett.* **2017**, *17*, 2482−2489.
(40) Zhu, H.; Fu, Y.; Meng, F.; Wu, X.; Gong, Z.; Ding, Q.; Gustafsson, M. V.; Trinh, M. T.; Jin, S.; Zhu, X. Y. Lead Halide Perovskite Nanowire Lasers with Low Lasing Thresholds and High Quality Factors. *Nat. Mater.* **2015**, *14*, 636−642.
(41) Zhang, Q.; Zhang, D.; Gu, L.; Tsui, K.-H.; Poddar, S.; Fu, Y.; Shu, L.; Fan, Z. Three-Dimensional Perovskite Nanophotonic Wire Array-Based Light-Emitting Diodes with Significantly Improved Efficiency and Stability. *ACS Nano* **2020**, *14*, 1577−1585.
(42) Chang, C.-Y.; Tsai, B.-C.; Lin, M.-Z.; Huang, Y.-C.; Tsao, C.-S. An Integrated Approach Towards the Fabrication of Highly Efficient and Long-Term Stable Perovskite Nanowire Solar Cells. *J. Mater. Chem. A* **2017**, *5*, 22824−22833.
(43) Meng, Y.; Lai, Z.; Li, F.; Wang, W.; Yip, S.; Quan, Q.; Bu, X.; Wang, F.; Bao, Y.; Hosomi, T. Perovskite Core−Shell Nanowire Transistors: Interfacial Transfer Doping and Surface Passivation. *ACS Nano* **2020**, *14*, 12749.
(44) García de Arquer, F. P.; Sargent, E. H. Perovskite Nanowires Find an Edge. *Nat. Electron.* **2018**, *1*, 380−381.
(45) Quan, L. N.; Rand, B. P.; Friend, R. H.; Mhaisalkar, S. G.; Lee, T.-W.; Sargent, E. H. Perovskites for Next-Generation Optical Sources. *Chem. Rev.* **2019**, *119*, 7444−7477.
(46) Long, G.; Sabatini, R.; Saidaminov, M. I.; Lakhwani, G.; Rasmita, A.; Liu, X.; Sargent, E. H.; Gao, W. Chiral-Perovskite Optoelectronics. *Nat. Rev. Mater.* **2020**, *5*, 423−439.
(47) Sutherland, B. R.; Sargent, E. H. Perovskite Photonic Sources. *Nat. Photonics* **2016**, *10*, 295−302.
(48) Fu, Y.; Zhu, H.; Chen, J.; Hautzinger, M. P.; Zhu, X. Y.; Jin, S. Metal Halide Perovskite Nanostructures for Optoelectronic Applications and the Study of Physical Properties. *Nat. Rev. Mater.* **2019**, *4*, 169−188.
(49) Im, J.-H.; Luo, J.; Franckevičius, M.; Pellet, N.; Gao, P.; Moehl, T.; Zakeeruddin, S. M.; Nazeeruddin, M. K.; Grätzel, M.; Park, N.-G. Nanowire Perovskite Solar Cell. *Nano Lett.* **2015**, *15*, 2120−2126.
(50) Singh, R.; Suranagi, S. R.; Yang, S. J.; Cho, K. Enhancing the Power Conversion Efficiency of Perovskite Solar Cells Via the Controlled Growth of Perovskite Nanowires. *Nano Energy* **2018**, *51*, 192−198.
(51) Wang, S.; Yan, S.; Wang, M.; Chang, L.; Wang, J.; Wang, Z. Construction of Nanowire $CH_3NH_3PbI_3$-Based Solar Cells with 17.62% Efficiency by Solvent Etching Technique. *Sol. Energy Mater. Sol. Cells* **2017**, *167*, 173−177.
(52) Wang, R.; Wang, F.; Zhou, W.; Fan, J. Z.; García de Arquer, F. P.; Xu, K.; Sargent, E. H.; Ning, Z. Colloidal-Quantum-Dot-in-Perovskite Nanowires. *Infrared Phys. Technol.* **2019**, *98*, 16−22.
(53) Asuo, I. M.; Gedamu, D.; Ka, I.; Gerlein, L. F.; Fortier, F.-X.; Pignolet, A.; Cloutier, S. G.; Nechache, R. High-performance Pseudo-Halide Perovskite Nanowire Networks for Stable and Fast-Response Photodetector. *Nano Energy* **2018**, *51*, 324−332.
(54) Wang, Y.; Lin, R.; Zhu, P.; Zheng, Q.; Wang, Q.; Li, D.; Zhu, J. Cation Dynamics Governed Thermal Properties of Lead Halide Perovskite Nanowires. *Nano Lett.* **2018**, *18*, 2772−2779.
(55) Petrov, A. A.; Pellet, N.; Seo, J.-Y.; Belich, N. A.; Kovalev, D. Y.; Shevelkov, A. V.; Goodilin, E. A.; Zakeeruddin, S. M.; Tarasov, A. B.; Graetzel, M. New Insight into the Formation of Hybrid Perovskite Nanowires via Structure Directing Adducts. *Chem. Mater.* **2017**, *29*, 587−594.
(56) He, X.; Liu, P.; Wu, S.; Liao, Q.; Yao, J.; Fu, H. Multi-color Perovskite Nanowire Lasers Through Kinetically Controlled Solution Growth Followed by Gas-Phase Halide Exchange. *J. Mater. Chem. C* **2017**, *5*, 12707−12713.
(57) Xu, X.; Zhang, X.; Deng, W.; Huang, L.; Wang, W.; Jie, J.; Zhang, X. Saturated Vapor-Assisted Growth of Single-Crystalline Organic−Inorganic Hybrid Perovskite Nanowires for High-Performance Photodetectors with Robust Stability. *ACS Appl. Mater. Interfaces* **2018**, *10*, 10287−10295.
(58) Liao, J.-F.; Li, W.-G.; Rao, H.-S.; Chen, B.-X.; Wang, X.-D.; Chen, H.-Y.; Kuang, D.-B. Inorganic cesium lead halide CsPbX3 nanowires for long-term stable solar cells. *Sci. China Mater.* **2017**, *60*, 285−294.
(59) Dou, L.; Lai, M.; Kley, C. S.; Yang, Y.; Bischak, C. G.; Zhang, D.; Eaton, S. W.; Ginsberg, N. S.; Yang, P. Spatially resolved multicolor $CsPbX_3$ nanowire heterojunctions via anion exchange. *Proc. Natl. Acad. Sci. U. S. A.* **2017**, *114*, 7216.
(60) Zhang, D.; Eaton, S. W.; Yu, Y.; Dou, L.; Yang, P. Solution-Phase Synthesis of Cesium Lead Halide Perovskite Nanowires. *J. Am. Chem. Soc.* **2015**, *137*, 9230−9233.
(61) Zhang, D.; Yu, Y.; Bekenstein, Y.; Wong, A. B.; Alivisatos, A. P.; Yang, P. Ultrathin Colloidal Cesium Lead Halide Perovskite Nanowires. *J. Am. Chem. Soc.* **2016**, *138*, 13155−13158.
(62) Pradhan, B.; Kumar, G. S.; Sain, S.; Dalui, A.; Ghorai, U. K.; Pradhan, S. K.; Acharya, S. Size Tunable Cesium Antimony Chloride Perovskite Nanowires and Nanorods. *Chem. Mater.* **2018**, *30*, 2135−2142.
(63) Wang, A.; Yan, X.; Zhang, M.; Sun, S.; Yang, M.; Shen, W.; Pan, X.; Wang, P.; Deng, Z. Controlled Synthesis of Lead-Free and Stable Perovskite Derivative Cs_2SnI_6 Nanocrystals via a Facile Hot-Injection Process. *Chem. Mater.* **2016**, *28*, 8132−8140.
(64) Penn, R. L.; Banfield, J. F. Imperfect Oriented Attachment: Dislocation Generation in Defect-Free Nanocrystals. *Science* **1998**, *281*, 969.
(65) Tong, Y.; Bohn, B. J.; Bladt, E.; Wang, K.; Müller-Buschbaum, P.; Bals, S.; Urban, A. S.; Polavarapu, L.; Feldmann, J. From Precursor Powders to $CsPbX_3$ Perovskite Nanowires: One-Pot Synthesis, Growth Mechanism, and Oriented Self-Assembly. *Angew. Chem.* **2017**, *56*, 13887−13892.
(66) Sun, J. K.; Huang, S.; Liu, X. Z.; Xu, Q.; Zhang, Q. H.; Jiang, W. J.; Xue, D. J.; Xu, J. C.; Ma, J. Y.; Ding, J.; et al. Polar Solvent Induced Lattice Distortion of Cubic CsPbI3 Nanocubes and Hierarchical Self-Assembly into Orthorhombic Single-Crystalline Nanowires. *J. Am. Chem. Soc.* **2018**, *140*, 11705−11715.

https://doi.org/10.1021/acsaem.1c03284
ACS Appl. Energy Mater. 2022, 5, 1342−1377

(67) He, L.; Pan, S.; Lin, Z.; Peng, J. Rapid Route to Polar Solvent-Directed Growth of Perovskite Nanowires. *ACS Appl. Nano Mater.* **2019**, *2*, 7910−7915.
(68) Ashley, M. J.; O'Brien, M. N.; Hedderick, K. R.; Mason, J. A.; Ross, M. B.; Mirkin, C. A. Templated Synthesis of Uniform Perovskite Nanowire Arrays. *J. Am. Chem. Soc.* **2016**, *138*, 10096−10099.
(69) Oener, S. Z.; Khoram, P.; Brittman, S.; Mann, S. A.; Zhang, Q.; Fan, Z.; Boettcher, S. W.; Garnett, E. C. Perovskite Nanowire Extrusion. *Nano Lett.* **2017**, *17*, 6557−6563.
(70) Lin, C.-H.; Li, T.-Y.; Zhang, J.; Chiao, Z.-Y.; Wei, P.-C.; Fu, H.-C.; Hu, L.; Yu, M.-J.; Ahmed, G. H.; Guan, X.; et al. Designed growth and patterning of perovskite nanowires for lasing and wide color gamut phosphors with long-term stability. *Nano Energy* **2020**, *73*, 104801.
(71) Liu, P.; He, X.; Ren, J.; Liao, Q.; Yao, J.; Fu, H. Organic−Inorganic Hybrid Perovskite Nanowire Laser Arrays. *ACS Nano* **2017**, *11*, 5766−5773.
(72) Spina, M.; Bonvin, E.; Sienkiewicz, A.; Náfrádi, B.; Forró, L.; Horváth, E. Controlled growth of $CH_3NH_3PbI_3$ nanowires in arrays of open nanofluidic channels. *Sci. Rep.* **2016**, *6*, 19834.
(73) Zhou, Q.; Park, J. G.; Nie, R.; Thokchom, A. K.; Ha, D.; Pan, J.; Seok, S. I.; Kim, T. Nanochannel-Assisted Perovskite Nanowires: From Growth Mechanisms to Photodetector Applications. *ACS Nano* **2018**, *12*, 8406−8414.
(74) Pan, S.; Zou, H.; Wang, A. C.; Wang, Z.; Yu, J.; Lan, C.; Liu, Q.; Wang, Z. L.; Lian, T.; Peng, J.; et al. Rapid Capillary-Assisted Solution Printing of Perovskite Nanowire Arrays Enables Scalable Production of Photodetectors. *Angew. Chem.* **2020**, *59*, 14942−14949.
(75) Deng, W.; Zhang, X.; Huang, L.; Xu, X.; Wang, L.; Wang, J.; Shang, Q.; Lee, S.-T.; Jie, J. Aligned Single-Crystalline Perovskite Microwire Arrays for High-Performance Flexible Image Sensors with Long-Term Stability. *Adv. Mater.* **2016**, *28*, 2201−2208.
(76) Xing, J.; Liu, X. F.; Zhang, Q.; Ha, S. T.; Yuan, Y. W.; Shen, C.; Sum, T. C.; Xiong, Q. Vapor Phase Synthesis of Organometal Halide Perovskite Nanowires for Tunable Room-Temperature Nanolasers. *Nano Lett.* **2015**, *15*, 4571−4577.
(77) Tavakoli, M. M.; Waleed, A.; Gu, L.; Zhang, D.; Tavakoli, R.; Lei, B.; Su, W.; Fang, F.; Fan, Z. A non-catalytic vapor growth regime for organohalide perovskite nanowires using anodic aluminum oxide templates. *Nanoscale* **2017**, *9*, 5828−5834.
(78) Waleed, A.; Tavakoli, M. M.; Gu, L.; Wang, Z.; Zhang, D.; Manikandan, A.; Zhang, Q.; Zhang, R.; Chueh, Y.-L.; Fan, Z. Lead-Free Perovskite Nanowire Array Photodetectors with Drastically Improved Stability in Nanoengineering Templates. *Nano Lett.* **2017**, *17*, 523−530.
(79) Chen, J.; Fu, Y.; Samad, L.; Dang, L.; Zhao, Y.; Shen, S.; Guo, L.; Jin, S. Vapor-Phase Epitaxial Growth of Aligned Nanowire Networks of Cesium Lead Halide Perovskites ($CsPbX_3$, X = Cl, Br, I). *Nano Lett.* **2017**, *17*, 460−466.
(80) Gao, Y.; Zhao, L.; Shang, Q.; Zhong, Y.; Liu, Z.; Chen, J.; Zhang, Z.; Shi, J.; Du, W.; Zhang, Y.; et al. Ultrathin $CsPbX_3$ Nanowire Arrays with Strong Emission Anisotropy. *Adv. Mater.* **2018**, *30*, 1801805.
(81) Sun, M.; Fang, Q.; Zhang, Z.; Xie, D.; Sun, Y.; Xu, J.; Li, W.; Ren, T.; Zhang, Y. All-Inorganic Perovskite Nanowires−InGaZnO-Heterojunction for High-Performance Ultraviolet−Visible Photodetectors. *ACS Appl. Mater. Interfaces* **2018**, *10*, 7231−7238.
(82) Wang, Y.; Sun, X.; Shivanna, R.; Yang, Y.; Chen, Z.; Guo, Y.; Wang, G.-C.; Wertz, E.; Deschler, F.; Cai, Z.; et al. Photon Transport in One-Dimensional Incommensurately Epitaxial $CsPbX_3$ Arrays. *Nano Lett.* **2016**, *16*, 7974−7981.
(83) Zhou, H.; Yuan, S.; Wang, X.; Xu, T.; Wang, X.; Li, H.; Zheng, W.; Fan, P.; Li, Y.; Sun, L.; et al. Vapor Growth and Tunable Lasing of Band Gap Engineered Cesium Lead Halide Perovskite Micro/Nanorods with Triangular Cross Section. *ACS Nano* **2017**, *11*, 1189−1195.
(84) Oksenberg, E.; Merdasa, A.; Houben, L.; Kaplan-Ashiri, I.; Rothman, A.; Scheblykin, I. G.; Unger, E. L.; Joselevich, E. Large Lattice Distortions and Size-Dependent Bandgap Modulation in Epitaxial Halide Perovskite Nanowires. *Nat. Commun.* **2020**, *11*, 489.
(85) Shoaib, M.; Zhang, X.; Wang, X.; Zhou, H.; Xu, T.; Wang, X.; Hu, X.; Liu, H.; Fan, X.; Zheng, W.; et al. Directional Growth of Ultralong $CsPbBr_3$ Perovskite Nanowires for High-Performance Photodetectors. *J. Am. Chem. Soc.* **2017**, *139*, 15592−15595.
(86) Wang, X.; Shoaib, M.; Wang, X.; Zhang, X.; He, M.; Luo, Z.; Zheng, W.; Li, H.; Yang, T.; Zhu, X.; et al. High-Quality In-Plane Aligned $CsPbX_3$ Perovskite Nanowire Lasers with Composition-Dependent Strong Exciton−Photon Coupling. *ACS Nano* **2018**, *12*, 6170−6178.
(87) Oksenberg, E.; Sanders, E.; Popovitz-Biro, R.; Houben, L.; Joselevich, E. Surface-Guided $CsPbBr_3$ Perovskite Nanowires on Flat and Faceted Sapphire with Size-Dependent Photoluminescence and Fast Photoconductive Response. *Nano Lett.* **2018**, *18*, 424−433.
(88) Schlaus, A. P.; Spencer, M. S.; Miyata, K.; Liu, F.; Wang, X.; Datta, I.; Lipson, M.; Pan, A.; Zhu, X. Y. How Lasing Happens in $CsPbBr_3$ Perovskite Nanowires. *Nat. Commun.* **2019**, *10*, 265.
(89) Wagner, R. S.; Ellis, W. C. Vapor□Liquid□Solid Mechanism of Single Crystal Growth. *Appl. Phys. Lett.* **1964**, *4*, 89−90.
(90) Güniat, L.; Caroff, P.; Fontcuberta i Morral, A. Vapor Phase Growth of Semiconductor Nanowires: Key Developments and Open Questions. *Chem. Rev.* **2019**, *119*, 8958−8971.
(91) Meng, Y.; Lan, C.; Li, F.; Yip, S.; Wei, R.; Kang, X.; Bu, X.; Dong, R.; Zhang, H.; Ho, J. C. Direct Vapor−Liquid−Solid Synthesis of All-Inorganic Perovskite Nanowires for High-Performance Electronics and Optoelectronics. *ACS Nano* **2019**, *13*, 6060−6070.
(92) Meyers, J. K.; Kim, S.; Hill, D. J.; Cating, E. E. M.; Williams, L. J.; Kumbhar, A. S.; McBride, J. R.; Papanikolas, J. M.; Cahoon, J. F. Self-Catalyzed Vapor−Liquid−Solid Growth of Lead Halide Nanowires and Conversion to Hybrid Perovskites. *Nano Lett.* **2017**, *17*, 7561−7568.
(93) Shim, H.; Shin, N. VLS Homoepitaxy of Lead Iodide Nanowires for Hybrid Perovskite Conversion. *J. Phys. Chem. Lett.* **2019**, *10*, 6741−6749.
(94) Yan, R.; Gargas, D.; Yang, P. Nanowire Photonics. *Nat. Photonics* **2009**, *3*, 569−576.
(95) Bai, S.; Wu, W.; Qin, Y.; Cui, N.; Bayerl, D. J.; Wang, X. High-Performance Integrated ZnO Nanowire UV Sensors on Rigid and Flexible Substrates. *Adv. Funct. Mater.* **2011**, *21*, 4464−4469.
(96) Zhu, J.; Yu, Z.; Burkhard, G. F.; Hsu, C.-M.; Connor, S. T.; Xu, Y.; Wang, Q.; McGehee, M.; Fan, S.; Cui, Y. Optical Absorption Enhancement in Amorphous Silicon Nanowire and Nanocone Arrays. *Nano Lett.* **2009**, *9*, 279−282.
(97) Fan, Z.; Razavi, H.; Do, J.-w.; Moriwaki, A.; Ergen, O.; Chueh, Y.-L.; Leu, P. W.; Ho, J. C.; Takahashi, T.; Reichertz, L. A.; et al. Three-Dimensional Nanopillar-Array Photovoltaics on Low-Cost and Flexible Substrates. *Nat. Mater.* **2009**, *8*, 648−653.
(98) Zheng, Z.; Gan, L.; Li, H.; Ma, Y.; Bando, Y.; Golberg, D.; Zhai, T. A Fully Transparent and Flexible Ultraviolet−Visible Photodetector Based on Controlled ElectrospunZnO-CdOHeterojunction-Nanofiber Arrays. *Adv. Funct. Mater.* **2015**, *25*, 5885−5894.
(99) Huang, S.; Guo, C. F.; Zhang, X.; Pan, W.; Luo, X.; Zhao, C.; Gong, J.; Li, X.; Ren, Z. F.; Wu, H. Buckled Tin Oxide Nanobelt Webs as Highly Stretchable and Transparent Photosensors. *Small* **2015**, *11*, 5712−5718.
(100) Li, C.; Huang, W.; Gao, L.; Wang, H.; Hu, L.; Chen, T.; Zhang, H. Recent Advances in Solution-Processed Photodetectors Based on Inorganic and Hybrid Photo-Active Materials. *Nanoscale* **2020**, *12*, 2201−2227.
(101) Zhang, X.; Wu, D.; Geng, H. Heterojunctions Based on II-VI Compound Semiconductor One-Dimensional Nanostructures and Their Optoelectronic Applications. *Crystals* **2017**, *7*, 307.
(102) Shi, L.; Nihtianov, S. Comparative Study of Silicon-Based Ultraviolet Photodetectors. *IEEE Sens. J.* **2012**, *12*, 2453−2459.
(103) LaPierre, R. R.; Robson, M.; Azizur-Rahman, K. M.; Kuyanov, P. A Review of III−V Nanowire Infrared Photodetectors and Sensors. *J. Phys. D Appl. Phys.* **2017**, *50*, 123001.

https://doi.org/10.1021/acsaem.1c03284
ACS Appl. Energy Mater. 2022, 5, 1342−1377

(104) Gu, L.; Tavakoli, M. M.; Zhang, D.; Zhang, Q.; Waleed, A.; Xiao, Y.; Tsui, K.-H.; Lin, Y.; Liao, L.; Wang, J.; et al. 3D Arrays of 1024-Pixel Image Sensors based on Lead Halide Perovskite Nanowires. *Adv. Mater.* **2016**, *28*, 9713−9721.
(105) Bao, C.; Yang, J.; Bai, S.; Xu, W.; Yan, Z.; Xu, Q.; Liu, J.; Zhang, W.; Gao, F. High Performance and Stable All-Inorganic Metal Halide Perovskite-Based Photodetectors for Optical Communication Applications. *Adv. Mater.* **2018**, *30*, 1803422.
(106) Miao, J.; Zhang, F. Recent Progress on Highly Sensitive Perovskite Photodetectors. *J. Mater. Chem. C* **2019**, *7*, 1741−1791.
(107) Wu, D.; Zhou, H.; Song, Z.; Zheng, M.; Liu, R.; Pan, X.; Wan, H.; Zhang, J.; Wang, H.; Li, X.; et al. Welding Perovskite Nanowires for Stable, Sensitive, Flexible Photodetectors. *ACS Nano* **2020**, *14*, 2777−2787.
(108) Tong, G.; Jiang, M.; Son, D.-Y.; Qiu, L.; Liu, Z.; Ono, L. K.; Qi, Y. Inverse Growth of Large-Grain-Size and Stable Inorganic PerovskiteMicronanowirePhotodetectors. *ACS Appl. Mater. Interfaces* **2020**, *12*, 14185−14194.
(109) Li, X.; Yu, D.; Chen, J.; Wang, Y.; Cao, F.; Wei, Y.; Wu, Y.; Wang, L.; Zhu, Y.; Sun, Z.; et al. Constructing Fast Carrier Tracks into Flexible Perovskite Photodetectors To Greatly Improve Responsivity. *ACS Nano* **2017**, *11*, 2015−2023.
(110) Gong, M.; Sakidja, R.; Goul, R.; Ewing, D.; Casper, M.; Stramel, A.; Elliot, A.; Wu, J. Z. High-Performance All-Inorganic $CsPbCl_3$ Perovskite Nanocrystal Photodetectors with Superior Stability. *ACS Nano* **2019**, *13*, 1772−1783.
(111) Lin, Q.; Armin, A.; Burn, P. L.; Meredith, P. Filterless Narrowband Visible Photodetectors. *Nat. Photonics* **2015**, *9*, 687−694.
(112) Saidaminov, M. I.; Adinolfi, V.; Comin, R.; Abdelhady, A. L.; Peng, W.; Dursun, I.; Yuan, M.; Hoogland, S.; Sargent, E. H.; Bakr, O. M. Planar-Integrated Single-Crystalline Perovskite Photodetectors. *Nat. Commun.* **2015**, *6*, 8724.
(113) Liu, X.; Gu, L.; Zhang, Q.; Wu, J.; Long, Y.; Fan, Z. All-Printable Band-Edge Modulated ZnO Nanowire Photodetectors with Ultra-High Detectivity. *Nat. Commun.* **2014**, *5*, 4007.
(114) de Quilettes, D. W.; Vorpahl, S. M.; Stranks, S. D.; Nagaoka, H.; Eperon, G. E.; Ziffer, M. E.; Snaith, H. J.; Ginger, D. S. Impact of Microstructure on Local Carrier Lifetime in Perovskite Solar Cells. *Science* **2015**, *348*, 683.
(115) Feng, J.; Gong, C.; Gao, H.; Wen, W.; Gong, Y.; Jiang, X.; Zhang, B.; Wu, Y.; Wu, Y.; Fu, H.; et al. Single-Crystalline Layered Metal-Halide Perovskite Nanowires for Ultrasensitive Photodetectors. *Nat. Electron.* **2018**, *1*, 404−410.
(116) Tang, X.; Zu, Z.; Shao, H.; Hu, W.; Zhou, M.; Deng, M.; Chen, W.; Zang, Z.; Zhu, T.; Xue, J. All-Inorganic PerovskiteCsPb$(Br/I)_3$Nanorods for Optoelectronic Application. *Nanoscale* **2016**, *8*, 15158−15161.
(117) Gao, R.; Li, G.; Han, Y.; Xi, Y.; Ji, T.; Tian, Y.; Tian, B.; Hao, Y.; Wu, Y.; Cui, Y. Carrier lifetime exceeding 81 ns in single crystalline perovskite nanowires enable large on-off ratio photodetectors. *Org. Electron.* **2020**, *83*, 105744.
(118) Wang, M.; Tian, W.; Cao, F.; Wang, M.; Li, L. Flexible and Self-Powered Lateral Photodetector Based on Inorganic Perovskite $CsPbI_3$−$CsPbBr_3$ Heterojunction Nanowire Array. *Adv. Funct. Mater.* **2020**, *30*, 1909771.
(119) Wang, Y.; Song, L.; Chen, Y.; Huang, W. Emerging New-Generation Photodetectors Based on Low-Dimensional Halide Perovskites. *ACS Photonics* **2020**, *7*, 10−28.
(120) Zhang, X.; Chen, S.; Wang, X.; Pan, A. Controlled Synthesis and Photonics Applications of Metal Halide Perovskite Nanowires. *Small Methods* **2019**, *3*, 1800294.
(121) Zhao, Y.; Li, C.; Shen, L. Recent advances on organic-inorganic hybrid perovskite photodetectors with fast response. *InfoMat* **2019**, *1*, 164−182.
(122) Hao, D.; Zou, J.; Huang, J. Recent developments in flexible photodetectors based on metal halide perovskite. *InfoMat* **2020**, *2*, 139−169.
(123) Wang, S.; Wang, K.; Gu, Z.; Wang, Y.; Huang, C.; Yi, N.; Xiao, S.; Song, Q. Solution-Phase Synthesis of Cesium Lead Halide Perovskite Microrods for High-Quality Microlasers and Photodetectors. *Adv. Opt. Mater.* **2017**, *5*, 1700023.
(124) Dong, D.; Deng, H.; Hu, C.; Song, H.; Qiao, K.; Yang, X.; Zhang, J.; Cai, F.; Tang, J.; Song, H. Bandgap tunable $Cs_x(CH_3NH_3)_{1-x}PbI_3$ perovskite nanowires by aqueous solution synthesis for optoelectronic devices. *Nanoscale* **2017**, *9*, 1567−1574.
(125) Lai, M.; Kong, Q.; Bischak, C. G.; Yu, Y.; Dou, L.; Eaton, S. W.; Ginsberg, N. S.; Yang, P. Structural, optical, and electrical properties of phase-controlled cesium lead iodide nanowires. *Nano Res.* **2017**, *10*, 1107−1114.
(126) Yang, T.; Zheng, Y.; Du, Z.; Liu, W.; Yang, Z.; Gao, F.; Wang, L.; Chou, K.-C.; Hou, X.; Yang, W. Superior Photodetectors Based on All-Inorganic Perovskite $CsPbI_3$ Nanorods with Ultrafast Response and High Stability. *ACS Nano* **2018**, *12*, 1611−1617.
(127) Gui, P.; Chen, Z.; Li, B.; Yao, F.; Zheng, X.; Lin, Q.; Fang, G. High-Performance Photodetectors Based on Single All-Inorganic $CsPbBr_3$ Perovskite Microwire. *ACS Photonics* **2018**, *5*, 2113−2119.
(128) He, X.; Jian, C.; Hong, W.; Cai, Q.; Liu, W. Ultralong $CH_3NH_3PbI_3$ nanowires synthesized by a ligand-assisted reprecipitation strategy for high-performance photodetectors. *J. Mater. Chem. C* **2020**, *8*, 7378−7383.
(129) Deng, H.; Dong, D.; Qiao, K.; Bu, L.; Li, B.; Yang, D.; Wang, H.-E.; Cheng, Y.; Zhao, Z.; Tang, J.; et al. Growth, patterning and alignment of organolead iodide perovskite nanowires for optoelectronic devices. *Nanoscale* **2015**, *7*, 4163−4170.
(130) Wang, H.; Haroldson, R.; Balachandran, B.; Zakhidov, A.; Sohal, S.; Chan, J. Y.; Zakhidov, A.; Hu, W. Nanoimprinted Perovskite Nanograting Photodetector with Improved Efficiency. *ACS Nano* **2016**, *10*, 10921−10928.
(131) Gao, L.; Zeng, K.; Guo, J.; Ge, C.; Du, J.; Zhao, Y.; Chen, C.; Deng, H.; He, Y.; Song, H.; et al. Passivated Single-Crystalline $CH_3NH_3PbI_3$ Nanowire Photodetector with High Detectivity and Polarization Sensitivity. *Nano Lett.* **2016**, *16*, 7446−7454.
(132) Feng, J.; Yan, X.; Liu, Y.; Gao, H.; Wu, Y.; Su, B.; Jiang, L. Crystallographically Aligned Perovskite Structures for High-Performance Polarization-Sensitive Photodetectors. *Adv. Mater.* **2017**, *29*, 1605993.
(133) Gao, H.; Feng, J.; Pi, Y.; Zhou, Z.; Zhang, B.; Wu, Y.; Wang, X.; Jiang, X.; Jiang, L. Bandgap Engineering of Single-Crystalline Perovskite Arrays for High-Performance Photodetectors. *Adv. Funct. Mater.* **2018**, *28*, 1804349.
(134) Chen, G.; Feng, J.; Gao, H.; Zhao, Y.; Pi, Y.; Jiang, X.; Wu, Y.; Jiang, L. Stable α-CsPbI3 Perovskite Nanowire Arrays with Preferential Crystallographic Orientation for Highly Sensitive Photodetectors. *Adv. Funct. Mater.* **2019**, *29*, 1808741.
(135) Li, S.-X.; Xu, Y.-S.; Li, C.-L.; Guo, Q.; Wang, G.; Xia, H.; Fang, H.-H.; Shen, L.; Sun, H.-B. Perovskite Single-Crystal Microwire-Array Photodetectors with Performance Stability beyond 1 Year. *Adv. Mater.* **2020**, *32*, 2001998.
(136) Tong, G.; Jiang, M.; Son, D.-Y.; Ono, L. K.; Qi, Y. 2D Derivative Phase Induced Growth of 3D All Inorganic Perovskite Micro−Nanowire Array Based Photodetectors. *Adv. Funct. Mater.* **2020**, *30*, 2002526.
(137) Kumar, G. S.; Sarkar, P. K.; Pradhan, B.; Hossain, M.; Rao, K. D. M.; Acharya, S. Large-area transparent flexible guanidinium incorporated $MAPbI_3$ microstructures for high-performance photodetectors with enhanced stability. *NanoscaleHoriz.* **2020**, *5*, 696−704.
(138) Asuo, I. M.; Fourmont, P.; Ka, I.; Gedamu, D.; Bouzidi, S.; Pignolet, A.; Nechache, R.; Cloutier, S. G. Highly Efficient and Ultrasensitive Large-Area Flexible Photodetector Based on Perovskite Nanowires. *Small* **2019**, *15*, 1804150.
(139) Tang, X.; Zhou, H.; Pan, X.; Liu, R.; Wu, D.; Wang, H. All-Inorganic Halide Perovskite Alloy Nanowire Network Photodetectors with High Performance. *ACS Appl. Mater. Interfaces* **2020**, *12*, 4843−4848.
(140) Deng, H.; Yang, X.; Dong, D.; Li, B.; Yang, D.; Yuan, S.; Qiao, K.; Cheng, Y.-B.; Tang, J.; Song, H. Flexible and Semitransparent

https://doi.org/10.1021/acsaem.1c03284
ACS Appl. Energy Mater. 2022, 5, 1342−1377

OrganoleadTriiodidePerovskite Network Photodetector Arrays with High Stability. *Nano Lett.* **2015**, *15*, 7963−7969.
(141) Rao, K. D. M.; Hossain, M.; Umesh; Roy, A.; Ghosh, A.; Kumar, G. S.; Moitra, P.; Kamilya, T.; Acharya, S.; Bhattacharya, S. Transparent, flexible $MAPbI_3$ perovskite microwire arrays passivated with ultra-hydrophobic supramolecular self-assembly for stable and high-performance photodetectors. *Nanoscale* **2020**, *12*, 11986−11996.
(142) Hossain, M.; Kumar, G. S.; BarimarPrabhava, S. N.; Sheerin, E. D.; McCloskey, D.; Acharya, S.; Rao, K. D. M.; Boland, J. J. Transparent, Flexible Silicon Nanostructured Wire Networks with Seamless Junctions for High-Performance Photodetector Applications. *ACS Nano* **2018**, *12*, 4727−4735.
(143) Waleed, A.; Tavakoli, M. M.; Gu, L.; Hussain, S.; Zhang, D.; Poddar, S.; Wang, Z.; Zhang, R.; Fan, Z. All Inorganic Cesium Lead Iodide Perovskite Nanowires with Stabilized Cubic Phase at Room Temperature and Nanowire Array-Based Photodetectors. *Nano Lett.* **2017**, *17*, 4951−4957.
(144) Zhang, F.; Lu, H.; Tong, J.; Berry, J. J.; Beard, M. C.; Zhu, K. Advances in two-dimensional organic−inorganic hybrid perovskites. *Energy Environ. Sci.* **2020**, *13*, 1154−1186.
(145) Wang, K.; Wu, C.; Yang, D.; Jiang, Y.; Priya, S. Quasi-Two-Dimensional Halide Perovskite Single Crystal Photodetector. *ACS Nano* **2018**, *12*, 4919−4929.
(146) Zhao, Y.; Qiu, Y.; Gao, H.; Feng, J.; Chen, G.; Jiang, L.; Wu, Y. Layered-Perovskite Nanowires with Long-Range Orientational Order for Ultrasensitive Photodetectors. *Adv. Mater.* **2020**, *32*, 1905298.
(147) Huang, M. H.; Mao, S.; Feick, H.; Yan, H.; Wu, Y.; Kind, H.; Weber, E.; Russo, R.; Yang, P. Room-Temperature Ultraviolet Nanowire Nanolasers. *Science* **2001**, *292*, 1897.
(148) Eaton, S. W.; Fu, A.; Wong, A. B.; Ning, C.-Z.; Yang, P. Semiconductor nanowire lasers. *Nat. Rev. Mater.* **2016**, *1*, 16028.
(149) Kondo, T.; Azuma, T.; Yuasa, T.; Ito, R. Biexciton Lasing in the Layered Perovskite-Type Material $(C_6H_{13}NH_3)_2PbI_4$. *Solid State Commun.* **1998**, *105*, 253−255.
(150) Eaton, S. W.; Lai, M.; Gibson, N. A.; Wong, A. B.; Dou, L.; Ma, J.; Wang, L.-W.; Leone, S. R.; Yang, P. Lasing in robust cesium lead halide perovskite nanowires. *Proc. Natl. Acad. Sci. U. S. A.* **2016**, *113*, 1993.
(151) Fu, Y.; Zhu, H.; Schrader, A. W.; Liang, D.; Ding, Q.; Joshi, P.; Hwang, L.; Zhu, X. Y.; Jin, S. Nanowire Lasers of Formamidinium Lead Halide Perovskites and Their Stabilized Alloys with Improved Stability. *Nano Lett.* **2016**, *16*, 1000−1008.
(152) Fu, Y.; Zhu, H.; Stoumpos, C. C.; Ding, Q.; Wang, J.; Kanatzidis, M. G.; Zhu, X.; Jin, S. Broad Wavelength Tunable Robust Lasing from Single-Crystal Nanowires of Cesium Lead Halide Perovskites ($CsPbX_3$, X = Cl, Br, I). *ACS Nano* **2016**, *10*, 7963−7972.
(153) Huang, L.; Gao, Q.; Sun, L.-D.; Dong, H.; Shi, S.; Cai, T.; Liao, Q.; Yan, C.-H. Composition-Graded Cesium Lead Halide Perovskite Nanowires with Tunable Dual-Color Lasing Performance. *Adv. Mater.* **2018**, *30*, 1800596.
(154) Shang, Q.; Zhang, S.; Liu, Z.; Chen, J.; Yang, P.; Li, C.; Li, W.; Zhang, Y.; Xiong, Q.; Liu, X.; et al. Surface Plasmon Enhanced Strong Exciton−Photon Coupling in Hybrid Inorganic−Organic Perovskite Nanowires. *Nano Lett.* **2018**, *18*, 3335−3343.
(155) Yu, H.; Ren, K.; Wu, Q.; Wang, J.; Lin, J.; Wang, Z.; Xu, J.; Oulton, R. F.; Qu, S.; Jin, P. Organic−inorganic perovskite plasmonic nanowire lasers with a low threshold and a good thermal stability. *Nanoscale* **2016**, *8*, 19536−19540.
(156) Du, W.; Zhang, S.; Shi, J.; Chen, J.; Wu, Z.; Mi, Y.; Liu, Z.; Li, Y.; Sui, X.; Wang, R.; et al. Strong Exciton−Photon Coupling and Lasing Behavior in All-Inorganic $CsPbBr_3$ Micro/Nanowire Fabry-Pérot Cavity. *ACS Photonics* **2018**, *5*, 2051−2059.
(157) Tan, Z.-K.; Moghaddam, R. S.; Lai, M. L.; Docampo, P.; Higler, R.; Deschler, F.; Price, M.; Sadhanala, A.; Pazos, L. M.; Credgington, D.; et al. Bright light-emitting diodes based on organometal halide perovskite. *Nat. Nanotechnol.* **2014**, *9*, 687−692.
(158) Zhao, B.; Bai, S.; Kim, V.; Lamboll, R.; Shivanna, R.; Auras, F.; Richter, J. M.; Yang, L.; Dai, L.; Alsari, M.; et al. High-efficiency perovskite−polymer bulk heterostructure light-emitting diodes. *Nat. Photonics* **2018**, *12*, 783−789.
(159) Chiba, T.; Hayashi, Y.; Ebe, H.; Hoshi, K.; Sato, J.; Sato, S.; Pu, Y.-J.; Ohisa, S.; Kido, J. Anion-exchange red perovskite quantum dots with ammonium iodine salts for highly efficient light-emitting devices. *Nat. Photonics* **2018**, *12*, 681−687.
(160) Lin, K.; Xing, J.; Quan, L. N.; de Arquer, F. P. G.; Gong, X.; Lu, J.; Xie, L.; Zhao, W.; Zhang, D.; Yan, C.; et al. Perovskite light-emitting diodes with external quantum efficiency exceeding 20%. *Nature* **2018**, *562*, 245−248.
(161) Protesescu, L.; Yakunin, S.; Bodnarchuk, M. I.; Krieg, F.; Caputo, R.; Hendon, C. H.; Yang, R. X.; Walsh, A.; Kovalenko, M. V. Nanocrystals of Cesium Lead Halide Perovskites ($CsPbX_3$, X = Cl, Br, and I): Novel Optoelectronic Materials Showing Bright Emission with Wide Color Gamut. *Nano Lett.* **2015**, *15*, 3692−3696.
(162) Song, J.; Li, J.; Li, X.; Xu, L.; Dong, Y.; Zeng, H. Quantum Dot Light-Emitting Diodes Based on Inorganic Perovskite Cesium Lead Halides ($CsPbX_3$). *Adv. Mater.* **2015**, *27*, 7162−7167.
(163) Wong, A. B.; Lai, M.; Eaton, S. W.; Yu, Y.; Lin, E.; Dou, L.; Fu, A.; Yang, P. Growth and Anion Exchange Conversion of $CH_3NH_3PbX_3$ Nanorod Arrays for Light-Emitting Diodes. *Nano Lett.* **2015**, *15*, 5519−5524.
(164) Yang, D.; Li, P.; Zou, Y.; Cao, M.; Hu, H.; Zhong, Q.; Hu, J.; Sun, B.; Duhm, S.; Xu, Y.; et al. Interfacial Synthesis of Monodisperse $CsPbBr_3$ Nanorods with Tunable Aspect Ratio and Clean Surface for Efficient Light-Emitting Diode Applications. *Chem. Mater.* **2019**, *31*, 1575−1583.
(165) Demchyshyn, S.; Roemer, J.; Groiss, H.; Heilbrunner, H.; Ulbricht, C.; Apaydin, D.; Rütt, U.; Bertram, F.; Hesser, G.; Scharber, M. Solid-State Nanopore Confinement for Band Gap Engineering of Metal-Halide Perovskites. *arXiv Preprint* **2016**, No. arXiv:1607.04661[cond-mat.mtrl-sci].
(166) Wei, Y.; Xu, Y.; Wang, Q.; Wang, J.; Lu, H.; Zhu, J. $CsPbBr_3$ nanowire polarized light-emitting diodes through mechanical rubbing. *ChemComm.* **2020**, *56*, 5413−5416.
(167) Lin, C.-H.; Kang, C.-Y.; Wu, T.-Z.; Tsai, C.-L.; Sher, C.-W.; Guan, X.; Lee, P.-T.; Wu, T.; Ho, C.-H.; Kuo, H.-C.; et al. Giant Optical Anisotropy of Perovskite Nanowire Array Films. *Adv. Funct. Mater.* **2020**, *30*, 1909275.
(168) Zhou, N.; Bekenstein, Y.; Eisler, C. N.; Zhang, D.; Schwartzberg, A. M.; Yang, P.; Alivisatos, A. P.; Lewis, J. A. Perovskite nanowire−block copolymer composites with digitally programmable polarization anisotropy. *Sci. Adv.* **2019**, *5*, No. eaav8141.
(169) Green, M. A.; Ho-Baillie, A.; Snaith, H. J. The emergence of perovskite solar cells. *Nat. Photonics* **2014**, *8*, 506−514.
(170) Stranks, S. D.; Eperon, G. E.; Grancini, G.; Menelaou, C.; Alcocer, M. J. P.; Leijtens, T.; Herz, L. M.; Petrozza, A.; Snaith, H. J. Electron-Hole Diffusion Lengths Exceeding 1 Micrometer in an Organometal Trihalide Perovskite Absorber. *Science* **2013**, *342*, 341.
(171) Wolff, C. M.; Canil, L.; Rehermann, C.; Ngoc Linh, N.; Zu, F.; Ralaiarisoa, M.; Caprioglio, P.; Fiedler, L.; Stolterfoht, M.; Kogikoski, S.; et al. Perfluorinated Self-Assembled Monolayers Enhance the Stability and Efficiency of Inverted Perovskite Solar Cells. *ACS Nano* **2020**, *14*, 1445−1456.
(172) Rahmany, S.; Etgar, L. Semitransparent Perovskite Solar Cells. *ACS Energy Lett.* **2020**, *5*, 1519−1531.
(173) Xiao, K.; Cui, C.; Wang, P.; Lin, P.; Qiang, Y.; Xu, L.; Xie, J.; Yang, Z.; Zhu, X.; Yu, X.; et al. Amine treatment induced perovskite nanowire network in perovskite solar cells: efficient surface passivation and carrier transport. *Nanotechnology* **2018**, *29*, 065401.
(174) Zhao, F.; Deng, L.; Wang, K.; Han, C.; Liu, Z.; Yu, H.; Li, J.; Hu, B. Surface Modification of SnO_2 via $MAPbI_3$ Nanowires for a Highly Efficient Non-Fullerene Acceptor-Based Organic Solar Cell. *ACS Appl. Mater. Interfaces* **2020**, *12*, 5120−5127.
(175) Raja, W.; Schmid, M.; Toma, A.; Wang, H.; Alabastri, A.; ProiettiZaccaria, R. Perovskite Nanopillar Array Based Tandem Solar Cell. *ACS Photonics* **2017**, *4*, 2025−2035.
(176) Chen, Y.; Wu, X.; Chu, Y.; Zhou, J.; Zhou, B.; Huang, J. Hybrid Field-Effect Transistors and Photodetectors Based on Organic

Semiconductor and $CsPbI_3$ Perovskite Nanorods Bilayer Structure. *Nano-Micro Lett.* **2018**, *10*, 57.
(177) Chen, P.-A.; Guo, J.; Nouri, M.; Tao, Q.; Li, Z.; Li, Q.; Du, L.; Chen, H.; Dong, Z.; Chang, L.; et al. Microfluidic solution-processed organic and perovskite nanowires fabricated for field-effect transistors and photodetectors. *J. Mater. Chem. C* **2020**, *8*, 2353−2362.
(178) Wang, Z.; Liu, J.; Xu, Z.-Q.; Xue, Y.; Jiang, L.; Song, J.; Huang, F.; Wang, Y.; Zhong, Y. L.; Zhang, Y.; et al. Wavelength-tunable waveguides based on polycrystalline organic−inorganic perovskite microwires. *Nanoscale* **2016**, *8*, 6258−6264.
(179) Lee, W.; Li, H.; Wong, A. B.; Zhang, D.; Lai, M.; Yu, Y.; Kong, Q.; Lin, E.; Urban, J. J.; Grossman, J. C.; et al. Ultralow thermal conductivity in all-inorganic halide perovskites. *Proc. Natl. Acad. Sci. U. S. A.* **2017**, *114*, 8693.

https://doi.org/10.1021/acsaem.1c03284
ACS Appl. Energy Mater. 2022, 5, 1342−1377